UNIVERSIDAD DE MÁLAGA

Facultad de Ciencias - Departamento de Física Aplicada I

TESIS DOCTORAL

ELECTROKINETICS OF SALT-FREE CONCENTRATED SUSPENSIONS INCLUDING ION SIZE EFFECTS

Rafael Roa Chamorro

2013

Programa de Doctorado en Química Avanzada
Preparación y Caracterización de Materiales

Félix Carrique Fernández, Catedrático del Departamento de Física Aplicada I de la Universidad de Málaga, y Emilio Ruiz Reina, Profesor Titular del Departamento de Física Aplicada II de la Universidad de Málaga,

CERTIFICAN:

Que el trabajo de investigación que se presenta en esta memoria, titulado

ELECTROKINETICS OF SALT-FREE CONCENTRATED SUSPENSIONS INCLUDING ION SIZE EFFECTS

ha sido realizado en el Departamento de Física Aplicada I de la Universidad de Málaga bajo nuestra dirección, así como durante su estancia en la UCD School of Physics (University College Dublin, Irlanda), por el Licenciado D. Rafael Roa Chamorro, y constituye su Tesis Doctoral.

Con esta fecha, autorizamos su presentación ante la Universidad de Málaga.

Málaga, 13 de Diciembre de 2012

Dr. Félix Carrique Fernández
Catedrático
Dpto. Física Aplicada I
Universidad de Málaga

Dr. Emilio Ruiz Reina
Profesor Titular
Dpto. Física Aplicada II
Universidad de Málaga

El doctorando
Rafael Roa Chamorro

Electrokinetics of salt-free concentrated suspensions including ion size effects

Rafael Roa Chamorro

Física Aplicada I, Universidad de Málaga

Málaga, Enero 2013

This thesis is mainly based in the following papers:

- R. Roa, F. Carrique and E. Ruiz-Reina. Electric double layer for spherical particles in salt-free concentrated suspensions including ion size effects. *Phys. Chem. Chem. Phys.* **13** (2011) 3960-3968.

- R. Roa, F. Carrique and E. Ruiz-Reina. Ion size effects on the electric double layer of a spherical particle in a realistic salt-free concentrated suspension. *Phys. Chem. Chem. Phys.* **13** (2011) 9644-9654.

- R. Roa, F. Carrique and E. Ruiz-Reina. DC electrokinetics for spherical particles in salt-free concentrated suspensions including ion size effects. *Phys. Chem. Chem. Phys.*, **13** (2011) 19437-19448.

- R. Roa, F. Carrique and E. Ruiz-Reina. Ion size effects on the electrokinetics of salt-free concentrated suspensions in ac fields. *J. Colloid Interface Sci.*, **387** (2012) 153-161.

Abstract

We analyze the influence of finite ion size effects in the response of a salt-free concentrated suspension of spherical particles to static and oscillating electric fields. Ideal salt-free suspensions are just composed of charged colloidal particles and the added counterions released by the particles to the solution that counterbalance their surface charge. To get closer to experimental conditions we also consider realistic salt-free suspensions. These realistic suspensions include water dissociation ions and those generated by atmospheric carbon dioxide contamination, in addition to the added counterions. We study the static and dynamic electrophoretic mobility of the particles and the conductivity and dielectric response of the suspension, as well as the equilibrium electric double layer. Some of the theoretical predictions are compared with preliminary experimental results. We find that the finite ion size significantly modifies the ionic condensation region near the particle surface for moderate to high particle charges. This produces an increment of the electrophoretic mobility and an enhancement of the Maxwell-Wagner-O'Konski process associated with the counterions condensation layer, that also yields an increment of the dynamic mobility for such frequencies. All these effects increase with ion size and particle charge. This work shows the importance of including ion size effects in any extension attempting to improve standard electrokinetic models.

Contents

Introduction

In the last years, there has been a renewed interest in electrophoresis. This is in part due to recent advances in nanoscience, which make possible the separation of macromolecules by size or charge. Suspended DNA or proteins are driven and separated by applying dc or ac electric fields [1–3]. Another main application in the field of nanoscience is the use of gold nanoparticles for drug delivery or cancer cell detection [4, 5]. Measurements of the electrophoretic mobility have been found to be useful to characterize the surface functionalization of these gold nanoparticles [6]. Usually particles are charged and suspended together with microions and a structure of electric double layer (EDL) appears around the particle [7–9]. The electrophoretic mobility of a suspended particle is not only dependent on the particle charge or the viscosity of the medium, but also on the configuration of the EDL.

Most of the theoretical EDL models are based on the classical Poisson-Boltzmann equation, a mean field approach that takes into account point-like ions in solution. This theory breaks down when the crowding of ions becomes significant, and steric repulsion and correlations potentially become important. Some authors have shown that the consideration of finite ion size effects allows for the crowding of ions near the particle surface [10]. This redistribution of ions modifies the EDL around the particle and consequently its electrophoretic mobility when an external electric field is applied [11–14].

We can find in the literature different studies dealing with ion size effects. Some of them concern microscopic descriptions of ion-ion correlations [15–30]. These approaches are mainly restricted to equilibrium conditions, but are able to predict important phenomena like overcharging [31,32]. Other studies are based on macroscopic descriptions considering average interactions by mean field approximations [10–14, 33–55]. In many of these works, the finite ion size is commonly included by modifying the activity coefficient of the ions in the electrochemical potential or by incorporating entropic contributions related to the excluded volume of the ions. The

macroscopic approaches have been found to work appreciably well with monovalent electrolytes for high particle charges and/or large ionic sizes when they have been compared with some simulation results [15].

Most works in electrokinetics concern suspensions with low particle concentration, but nowadays it is the concentrated regime that deserves more attention because of its practical applications [56]. These systems are difficult to understand due to the inherent complexity associated with the increasing particle-particle electrohydrodynamic interactions as particle concentration grows [57,58]. On the other hand, systems with low salt concentration show a lower screening of the repulsive electrostatic particle-particle interactions, which favors the generation of colloidal crystals or glasses [59]. Suspensions just composed of charged particles and their ionic counter-charges (the so-called added counterions) in the liquid medium are termed ideal salt-free suspensions, or just salt-free suspensions. The interest in these systems has increased in recent years from both experimental and theoretical points of view [14, 53–55, 60–76].

The aim of this thesis is to analyze the influence of finite ion size effects in the response of a salt-free concentrated suspension to static and oscillating electric fields. We will study specially the static and the dynamic electrophoretic mobility of the particles, and the conductivity and the dielectric response of the suspension, as well as the equilibrium EDL [14,53,54]. To get closer to experimental conditions we will also discuss the equilibrium EDL in realistic salt-free concentrated suspensions. [55]. These realistic suspensions include water dissociation ions and those generated by atmospheric carbon dioxide contamination, in addition to the added counterions released by the particles to the solution. To test the validity of these models, some calculations are compared with preliminary experimental results of the static and dynamic electrophoretic mobility of charged colloidal particles.

This thesis is structured as follows. In Chapter 1 we present an introduction about soft condensed matter, focusing on colloidal suspensions. We discuss the use of a spherical cell approach to deal with particle-particle interactions and review some previous works dealing with ion size effects. We describe the electrokinetic model to account for ion size effects in ideal salt-free concentrated suspensions in Chapter 2. We also give details of the resolution method of the electrokinetic equations and define the quantities we calculate. The results of the numerical calculations are analyzed upon changing particle surface charge density, particle volume fraction, and size of the counterions. In order to show the realm of the finite ion size effect in ideal salt-free suspensions, the results are compared with standard

predictions for point-like ions. In Chapter 3 we present a model for the equilibrium EDL in realistic salt-free suspensions including ion size effects. We solve the model numerically and compare the results with those for ideal salt-free suspensions and with point-like calculations. We also show some preliminary experimental results to compare theoretical predictions of the models described before. Conclusions are presented in Chapter 4.

Chapter 1

Colloidal systems

This chapter presents an introduction to colloidal suspensions. In particular, we pay our attention to salt-free concentrated suspensions of charged colloids. We discuss the use of a spherical cell approach to deal with particle-particle interactions. Classical works based on mean-field theories have usually neglected the excluded volume of the ions. We conclude this chapter reviewing existing works that account for ion size effects, which are the cornerstone of this thesis.

1.1   Colloidal suspensions

"Take a little fine dust, pour it into a glass of water, mix with care, and you get a colloid. That's all. A colloid, in its simplest form, is just a suspension of solid particles in a liquid. Actually, you don't even need a liquid. Candle smoke coiling and spreading in air is a colloid too, but one where the particles are suspended in a gas" [77].

Soft matter is a quite recent branch of condensed matter physics [78]. One of the particularities of soft matter systems is that many of their properties cannot be predicted directly from their atomic or molecular constituents. Usually, the microscopic components join into larger structures, each of them with a precise identity and function. The properties of these mesoscopic structures may determine the macroscopic behavior of the material. In his Nobel Lecture, de Gennes points out that the two major features of soft matter systems are complexity and flexibility. Examples of this kind of systems are colloids, aerosols, polymers, emulsions, gels, liquid crystals, granular matter, membranes, biopolymers, biological machines, etc.

This thesis is focused on colloids which, in spite of being one of the

most simple examples of soft matter systems, have an enormous practical importance. Colloidal suspensions consist in a dispersion of particles in a fluid, that can be either a liquid or a gas (in this case we call them aerosols). The colloidal particles can be made of any kind of material: solid, liquid immiscible with the solvent (emulsions), or gas (foams); have any shape, and be flexible or rigid (like a polymer coil or a vesicle). The characteristic that distinguishes colloids from other particles is their size. Their volume must be quite large in comparison with the solvent molecules. In the lower limit, particles with size of a couple of nanometers, like a micelle, can be considered as colloids. For the upper limit, we just ask that they are not so large that their settling under their own weight does not overwhelm their Brownian motion (which differentiate them from a granular material) [77].

The properties of colloidal suspensions are mostly dominated by surface and interfacial effects. To understand them we may consider the following example. The surface of a cubic block with a side of 0.1 cm is $S = 0.0006$ m^2. Let's divide it to get tiny blocks with 0.1 μm side. We will obtain 10^{15} blocks with a huge total surface area $S = 60$ m^2. The larger the contact surface, the faster that materials and energy can be exchanged with the surroundings. This feature makes possible, for example, the use of gold nanoparticles for drug delivery or cancer cell detection [4, 5]

Electric double layer

It is an experimental fact that colloidal particles get an electric surface charge when dispersed in a polar solvent, in particular, in an aqueous electrolyte solution. Different mechanisms explain the origin of this charge [8, 9, 79, 80]. The electroneutrality condition impose that the liquid adjacent to the particle must have a net electric charge, opposite to that on the particle surface. Clearly, the charged surface will influence the distribution of the nearby ions in the electrolyte solution. Ions of opposite charge to that of the surface, called counterions, will be attracted toward the surface, while ions of like charge, called coions, will be repelled from the surface. As a consequence of the attraction and repulsion between the ions in the electrolyte solution and the charged surface, there will be a non-uniform ionic distribution normal to the surface. Such a redistribution of the free ions in solution gives rise to the so-called electric double layer (EDL). In simple terms, its name came about because of the separation of charge between the surface and the electrolyte solution. One layer is the charge on the surface, and the other, a "layer" of ions in the vicinity of the surface.

The concept of EDL was introduced by Helmholtz in 1879. His dou-

ble layer model was very primitive and consisted of a charged flat surface and a spatial countercharge with opposite sign as compared to that of the surface, forming a "molecular condenser". However, thermal motion causes the counterions to be spread out in space, forming a diffuse double layer. In the early 1900s, Gouy and Chapman developed independently a theory that accounted for such diffuse double layer [81, 82]. In their model, the charged surface is composed of a layer of charges and has a surface potential Ψ_s^0. The ions in solution are considered as point charges immersed in a continuous dielectric medium. The repulsion/attraction coupled with the random thermal Brownian motion of the ions within the dielectric medium gives rise to a diffuse electrical layer [9].

We have mentioned that the presence of a charged surface gives rise to a spatial distribution of the ions normal to the surface. In the equilibrium, the ionic distribution is related to the equilibrium electric potential, Ψ^0, through the Boltzmann distribution. In the present context, a dilute electrolyte solution described within a mean-field theory, the ionic number concentration of the ith ionic species is

$$n_i^0 = n_{i\infty} \exp\left(\frac{-z_i e \Psi^0}{k_B T}\right) \tag{1.1}$$

where $n_{i\infty}$ is the ionic number concentration at the neutral state in which $\Psi^0 = 0$, called bulk, z_i the ionic valency, e the elementary electric charge, k_B the Boltzmann constant and T the absolute temperature.

In an electrolyte solution, the continuous phase is water, which is considered a dielectric medium, and the free charges are the ions contained in the electrolyte solution. Therefore, Poisson's equation is the appropriate equation to analyze the electric diffuse double layers where the dielectric permittivity of water, ϵ_{rs}, is assumed constant. The Poisson equation is given by

$$\epsilon_{rs}\epsilon_0 \nabla^2 \Psi^0 = -\rho_f^0 = -\sum_{i=1}^{N} z_i e n_i^0 \tag{1.2}$$

where ϵ_0 is the permittivity of the vacuum and ρ_f^0 is the space charge density of the mobile ("free") ions, that can be written in terms of the number concentrations of the N ionic species in the electrolyte solution. Combining Eq. 1.1 and 1.2 we obtain the well-known Poisson-Boltzmann equation.

$$\epsilon_{rs}\epsilon_0 \nabla^2 \Psi^0 = -\sum_{i=1}^{N} z_i e n_{i\infty} \exp\left(\frac{-z_i e \Psi^0}{k_B T}\right) \tag{1.3}$$

The Poisson-Boltzmann equation defines the electric potential distribution in the diffuse ionic layer adjacent to a charged surface subject to appropriate boundary conditions. In the case of planar EDL's with a symmetric electrolyte, it is possible to obtain an analytical solution for Ψ^0 without any further approximations. Considering the boundary conditions $\Psi^0 = \Psi_s^0$ at the particle surface, $x = 0$, and $\Psi^0 = 0$ at the bulk, $x \to \infty$, we obtain

$$\Psi^0 = 2 \ln \left[\frac{1 + \exp(-\kappa x)\tanh(\Psi_s^0/4)}{1 - \exp(-\kappa x)\tanh(\Psi_s^0/4)} \right] \qquad (1.4)$$

This solution is known as Gouy-Chapman theory. In this Equation κ^{-1} is the Debye length, which is defined as

$$\kappa^{-1} = \left(\frac{\epsilon_{rs}\epsilon_0 k_B T}{\sum_{i=1}^{N} e^2 z_i^2 n_{i\infty}} \right)^{1/2} \qquad (1.5)$$

The Debye length is a measure of the EDL thickness, and is a property of the electrolyte solution. It should be noted that this parameter contains no information about properties of the charged surface. Although it is normally referred to as the thickness of the EDL, the actual thickness of a double layer extends well beyond κ^{-1}. Typically, the Debye length would represent a characteristic distance from the charged surface to a point where the electric potential decays to approximately 33% of the surface potential, when the latter is rather low.

The Gouy-Chapman treatment of the diffuse EDL assumes that the ions are point charges and that the inner boundary of the EDL is on the particle surface. The location of the outer boundary is characterized by the inverse Debye length. The present theory has some difficulties at small κx values when Ψ_s^0 is large.

In 1924 Stern proposed a modification of the Gouy-Chapman model [83]. The structure of Stern's EDL can be very complex, not fully resolved in many instances, and it may contain three or more layers extending over varying distances from the solid surface, Fig. 1.1 [8, 9, 79].

Ions capable of undergoing specific adsorption might be located close to the particle surface. Their distance to the surface will be of the order of an ionic radius because it is assumed that they have lost their hydration shell, at least in the direction of the particle surface. This plane of ions is called inner Helmholtz plane (IHP) and is located at a distance β_i from the particle surface. The consideration of finite size ions makes the region between the particle surface and the IHP to be free of charge. Ions placed in

this region will have not only electrostatic interactions with the surface. In fact they often overcome electric repulsions, and are capable, for instance, of increasing the positive charge of an already positive surface. It is usual to say that the missing interactions are of a chemical or specific nature [79].

At a larger distance from the surface β_d and beyond, we find ions subjected only to electrostatic interactions with the surface. They are also exposed to collisions with solvent molecules, and therefore they are distributed over a certain distance to the particle surface. The plane located at β_d is called outer Helmholtz plane (OHP) and identifies the beginning of the diffuse layer. The region between the particle surface and the OHP is termed Stern layer. The electric potential changes from the surface potential, Ψ_s^0, to Ψ_d^0 within the Stern layer and it decays to zero far away from the Stern plane, Fig. 1.1.

The ions and liquid closer to the particle surface, the so-called stagnant layer, can be considered immobile. On the contrary, both ions and liquid outside it can be moved by an external field, and therefore a relative motion between the phases in contact will occur. The exact location of the boundary between the mobile and immobile phases, the so-called slipping or shear plane, is a matter of investigation [8,79]. We have shown it in Fig. 1.1 at a
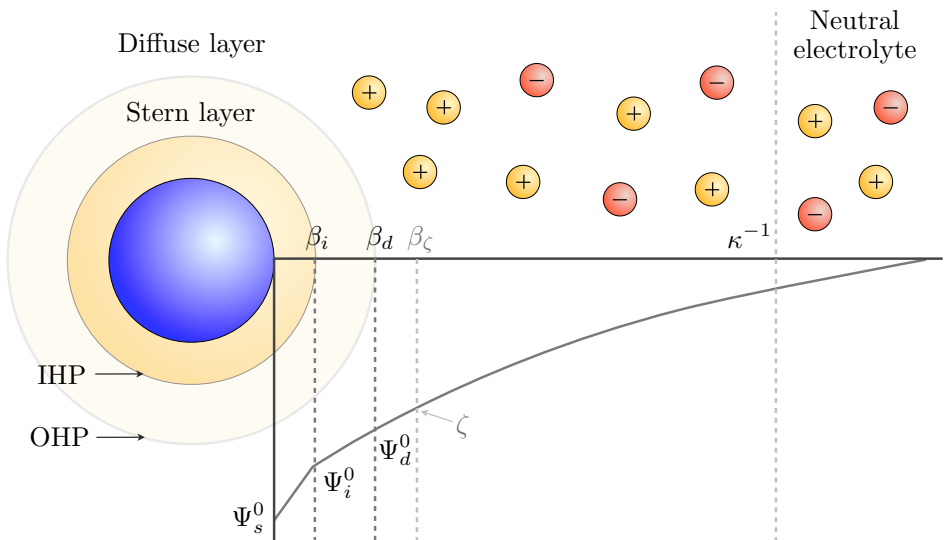

Figure 1.1: Schematic representation of potential distribution at a negatively charged interface showing the Debye length, κ^{-1}, and the overall extent of the EDL within the Stern model.

distance β_ζ from the surface. The potential at the shear plane is referred to as the electrokinetic potential, more commonly known as the zeta potential, ζ.

Electrokinetic phenomena

The term electrokinetics is associated with the relative motion between two charged phases. Electrokinetic phenomena take place when one tries to shear off the mobile part of the EDL. Then, as the charged particle tends to move in the appropriate direction, the ions in the mobile part of the EDL suffer a net migration in the opposite direction, dragging solvent with them, thereby causing the movement of the solvent. In the same way, an electric field is created if the charged surface and the diffuse part of the double layer are made to move relative to each other [9].

The different electrokinetic phenomena can be distinguished by the mobile/immobile phases, the nature of the applied field, and the quantity that must be experimentally determined. In this thesis we are specially interested in three of them [79]:

- Electrophoresis. It is the translation of a colloidal particle under the action of an externally applied field constant in time and position independent. For not very large applied fields, there is a linear relationship between the steady electrophoretic velocity, $\mathbf{v}_e$, and the applied field, $\langle \mathbf{E} \rangle$: $\mathbf{v}_e = \mu \langle \mathbf{E} \rangle$; where μ is the quantity of interest, known as electrophoretic mobility. Electrophoresis is usually employed in measuring the surface potential of a charged particle.

- Dielectric dispersion. It is the change with the frequency of an applied ac field of the dielectric permittivity of a suspension of colloidal particles. The phenomenon is also dependent on the concentration of particles, their zeta potential, and the ionic composition of the medium and appears to be very sensitive to most of these quantities. The analysis of the permittivity by dielectric spectroscopy provides rich information on the dynamics of the EDL because such technique is very sensitive to the particle-solution interface. The dielectric spectroscopy can also be used to study and characterize cell cultures [84,85] and DNA molecules in saline solutions [86].

- Electroacoustic phenomena. These electrokinetic phenomena have recently gained interest, both experimentally and theoretically. In the

ESA (electrokinetic sonic amplitude) technique, an alternating electric field is applied to the suspension and the sound wave produced in the system is detected and analyzed. The colloid vibration potential (CVP) or colloid vibration current (CVI) is the reciprocal of the former: a mechanic (ultrasonic) wave is forced to propagate in the system, and the resulting alternating potential difference (or current) is measured.

Salt-free and concentrated suspensions

In the previous discussion we have considered dilute colloidal suspensions, and therefore we have not taken into account the effect of particle-particle interactions. We define the particle volume fraction, ϕ, as the ratio between the volume occupied by the particles and the volume of the whole suspension. Regarding this definition, dilute suspensions are characterized for taking low ϕ values. On the contrary, in concentrated suspensions, where ϕ takes high values, the volume occupied by the particles in the suspension is a considerable part of it, and the interactions between particles cannot be neglected [57, 58]. Due to this reason, the study of concentrated suspensions is a less explored field in spite of their technological and fundamental importance. For example, a large number of suspensions of industrial interest (like paints, ceramics, drugs or soils) are concentrated [56]. Besides, electrokinetic effects are also present in situations where non homogeneous electric fields allow the separation, mixing, or concentration of dispersed particles [87, 88].

These applications require techniques for the characterization of the properties of the suspension, like stability, particle size distribution or surface charge. The use of light scattering techniques has limited applicability in concentrated or turbid suspensions. For this reason, methods based on the determination of some electrokinetic properties to perform such characterization, like electroacoustic techniques [89] or the determination of the low frequency permittivity of the suspension [90], are in demand.

The discussion presented before has been also referred to electrolyte solutions. Systems with low salt concentration show a lower screening of the repulsive electrostatic particle-particle interactions, which, for example, favors the generation of colloidal crystals or glasses [59]. Suspensions just composed of charged particles and their ionic countercharges (the so-called added counterions) in the liquid medium are termed ideal salt-free suspensions, or just salt-free suspensions [64, 66, 67]. Therefore, in salt-free suspensions the ionic species in the dispersion medium come solely from the

dissociation of the functional groups of the dispersed phase. An aqueous dispersion can be treated as a salt-free dispersion when the concentrations of hydrogen ions and hydroxide ions are much lower than the concentration of the added counterions. To get closer to experimental conditions, Carrique *et al.* have proposed a theoretical model to deal with realistic salt-free concentrated suspensions [70–74]. These realistic suspensions include water dissociation ions and those generated by atmospheric carbon dioxide contamination, in addition to the added counterions released by the particles to the solution.

It should be noted that only added counterions are present in the EDL. As a result, the Debye length is no longer a parameter that can be adjusted experimentally by changing the concentration of added electrolyte. Instead, the thickness of the EDL in salt-free suspensions can be modified only by changing the particle volume fraction. Also, an interesting phenomenon in this kind of suspensions was reported by Manning, Imai and Oosawa, among others [91–93]. They concluded that above a critical particle surface charge value, a condensate of counterions is formed around the particle. The interest in these systems has increased in recent years from both experimental and theoretical points of view [14, 53–55, 60–76].

1.2   Spherical cell approach

There are many obstacles in formulating and solving mathematical problems intended for obtaining spatial distributions of physical quantities inside a multi-particle system, such as concentrated suspensions. Fortunately, it is not necessary to know all the details of these distributions. Typical experiments with multi-particle systems deal with measuring the responses of the entire system under given external influences. Such responses can be addressed by averaging the actual distributions of physical quantities over the multi-particle system volume.

We use the concept of macroscopically homogeneous medium to simplify the procedure of obtaining the response of the system to external influences. A macroscopically homogeneous medium is characterized by a set of equivalent parameters called kinetic coefficients. Such coefficients are calculated by averaging the local distributions of physical quantities over a representative part, the cell, of the disperse system, not over the entire volume.

Two conditions are required to consider a multi-particle system as macroscopically homogeneous medium: (i) the dimensions of the representative cell should be negligible in comparison with the dimensions of the whole sys-
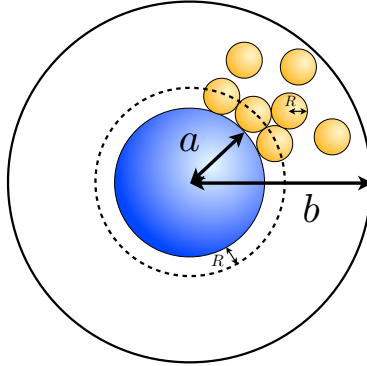
Figure 1.2: Spherical cell model including the distance of closest approach of the counterions to the particle surface.

tem; and (ii) the average over the representative cell gives rise to the same set of kinetic coefficients irrespective of the position of the representative cell. When the second condition is satisfied, an average over the disperse system volume is always equal to the average over the representative cell volume.

The spherical cell approach is an approximate method for addressing macroscopically homogeneous and isotropic media consisting of particles dispersed in a continuous phase. In this approach, represented in Fig. 1.2, each spherical particle of radius a is surrounded by a concentric shell of the liquid medium, having an outer radius b such that the particle/cell volume ratio in the cell is equal to the particle volume fraction throughout the entire suspension, that is

$$\phi = \left(\frac{a}{b}\right)^3 \tag{1.6}$$

The above assumption enables one to predict the kinetic coefficients by averaging electrical, hydrodynamic and ion concentration fields over the spherical cell volume. Consequently, the boundary value problem, which should be solved for describing these fields, is formulated inside the spherical cell.

After the pioneering papers of Levine and Neale [94] and Shilov, Zharkikh and Borkovskaya [95], a large number of theoretical studies were concerned with applying the spherical cell approach for describing electrokinetic phenomena. Among others, it is worthwhile to mention the works in salt-free systems of Ohshima (static and dynamic electrophoretic mobility) [64,65], Lee *et al.* (electrophoresis) [66,76] and Carrique *et al.* (dc and ac electroki-

netics in salt-free and realistic salt-free concentrated suspensions) [67–74]. The spherical cell approach has been successfully tested against experimental electrokinetic results in concentrated suspensions [96–99]. It has been also recently shown that, up to moderately strong electrostatic couplings, the spherical cell approach proves accurate for the prediction of osmotic pressures of deionised suspensions in agreement with Monte Carlo simulations and renormalized-effective interaction approaches [100].

An interested reader can find more details about the spherical cell approach and its history in the review of Zholkovskij *et al.* [101].

1.3   Ion size effects

All the previous theories, that describe point-like ions in a mean-field approximation, break down when the crowding of ions becomes significant, and steric repulsion and correlations potentially become important. We have seen that long ago Stern postulated a static compact monolayer of solvated ions located at the particle surface to account for the obvious ionic excess in the Poisson-Boltzmann theory [83]. A lack of this theory is that the size of the ions should be considered not only at the monolayer. Besides, a dynamical model is required for a "condensed layer" that is built and destroyed as the applied field alternates. Such condensed layer should be described by the same ion transport equations used for the diffuse part of the EDL.

We can find in the literature different attempts to overcome these limitations. Some of them concern microscopic descriptions of ion-ion correlations and the finite size of the ions [15–22]. There are also some works dealing with the response of colloidal suspensions under external electric fields using microscopic descriptions [23–30]. In spite of their advantages in comparison with mean-field approaches, time-dependent problems within this level of description require much more computational time and are restricted to simple configurations regarding particle charge and volume fraction.

In this work we focus in macroscopic descriptions considering average interactions by mean-field approximations. Many "modified Poisson-Boltzmann" theories have been proposed to describe equilibrium ion profiles near a charged wall [33–37]. An extensive review of these theories can be found in Ref. [10]. The first complete modified Poisson-Boltzmann model with steric effects in the electrolyte phase was proposed by Bikerman in 1942 [33]. Bikerman applied continuum volume constraints to the Poisson-

Boltzmann theory, which corresponds to an excess chemical potential

$$\mu_i^{0,ex} = -k_B T \ln(1 - \Phi) \tag{1.7}$$

associated with the entropy of the solvent, where $\Phi = a^3 \sum_i c_i$ is the local volume fraction of solvated ions on the lattice [102]. For a symmetric binary electrolyte, the ionic concentration within the Bikerman model is

$$n_i^0 = \frac{n_{i\infty} \exp\left(\frac{-z_i e \Psi^0}{k_B T}\right)}{1 + 2\nu \sinh^2(z_i e \Psi^0/2k_B T)} \tag{1.8}$$

where $\nu = 2a^3 n_{i\infty}$ is the bulk volume fraction of solvated ions. Due to the underlying lattice-gas model for excluded volume, the ion profiles effectively obey Fermi-Dirac statistics. Classical Boltzmann statistics and the Gouy-Chapman model for Poisson-Boltzmann are recovered in the limit of point-like ions, $\nu = 0$.

Bikerman's modified Poisson-Boltzmann equation has been independently reformulated by many authors [38–44]. Most of these authors derived the same model starting from the bulk statistical mechanics of ions and solvent molecules on a cubic lattice of spacing in the continuum limit where the concentration profiles vary slowly over the lattice.

Several authors have studied non-equilibrium properties departing from Bikerman's model. This is the case of Kilic, Bazant and Adjari with dilute electrolytes in large applied voltages [10, 45, 46] or Khair and Squires in electrophoresis of colloids [12]. In a series of papers, López-García and coworkers [11, 47–49] have studied the electrokinetics of dilute colloidal suspensions in electrolyte solutions including ion size effects. In a similar way as Stern, they considered that ions cannot approach to the particle surface as much as their hydrated ionic radius, although no chemical adsorption is taken into account in this model. They have found that ion size effects should be considered in all magnitudes studied, specially for moderate to high particles charges and electrolyte concentrations. In the response of the suspension under oscillating electric fields, this effect is also significant for weekly charged partices.

Their mean-field model has been compared with some Monte Carlo simulations for general ionic conditions [15]. While the latter has predicted charge inversion [31, 32] for the case of multivalent ions, the mean-field model has been unable to show such behaviours whatever the valency of the ions may be. Another theoretical approximation, the HNC-MSA [21, 27], has also found charge inversion for such conditions. It was concluded that

the neglecting of ion-ion correlations in the mean-field model was its main drawback. Very recently, Lopez-García *et al.* [13, 50] presented a modified standard electrokinetic model for diluted suspensions which takes into account the finite ion size and considers a minimum approach distance of ions to the particle surface not necessarily equal to their effective radius in the bulk solution. They show that this model is able to predict overcharging for high electrolyte concentration and counterions valency. We think that this is a very important result because to our knowledge this is the first time that a phenomenological theory based on macroscopic descriptions is able to predict this phenomenon. In two recent contributions, the same authors have considered the finite ion size by modelling the aqueous electrolyte solution as a suspension of polarizable insulating spheres in water [51, 52].

In this thesis we study the electrokinetics of salt-free concentrated suspensions of colloidal particles including ion size effects. We use a spherical cell approach to deal with particle-particle interactions within a mean-field model. Following the work of Borukhov *et al.* [38], we consider the finite size of the counterions using a phenomenological free energy derivation. The result for the equilibrium is a modified Poisson-Boltzmann equation similar to Bikerman's one. Finite size counterions in our model are depicted in Fig. 1.2, *i.e.* they are treated like spheres of radius R with a point charge at their center that cannot approach to the particle surface as much as their hydrated ionic radius [11]. This definition makes the region between the particle surface and one ionic radius to be free of charge. Ion size effects are also considered in the fundamental electrokinetic equations [7, 103] to predict non-equilibrium properties of this system.

Chapter 2

Ideal salt-free suspensions

Having presented the system we are concerned, we develop a theoretical model to consider finite size counterions in ideal salt-free concentrated suspensions. We analyze the equilibrium response of the system as well as the response to static and alternating external electric fields. We show the importance of our corrections by calculating the electrophoretic mobility of the particles and conductivity and the dielectric response of the suspension, and by comparing these results with the classical predictions for point-like counterions.

2.1   Model

2.1.1   Electrokinetic equations

Let us consider a spherical charged particle of radius a, surface charge density σ, mass density ρ_p and relative permittivity ϵ_{rp} immersed in an ideal salt-free medium of relative permittivity ϵ_{rs}, mass density ρ_s and viscosity η, with only the presence of the added counterions of valency z_c and drag coefficient λ_c. We consider finite size counterions as spheres of radius R with a point charge at their center. By applying to the system an oscillating electric field $\mathbf{E}\,e^{-i\omega t}$ of angular frequency ω, the particle moves with a velocity $\mathbf{v}_e e^{-i\omega t}$, the dynamic electrophoretic velocity. The axes of the spherical coordinate system $(r,\ \theta,\ \varphi)$ are fixed at the center of the particle, with the polar axis $(\theta = 0)$ parallel to the electric field. The solution of the problem at time t requires the knowledge, at every point $\mathbf{r}$ in the system, of the electric potential, $\Psi(\mathbf{r}, t)$, the number density of counterions, $n_c(\mathbf{r}, t)$, their drift velocity, $\mathbf{v}_c(\mathbf{r}, t)$, the fluid velocity, $\mathbf{v}(\mathbf{r}, t)$, and the pressure, $P(\mathbf{r}, t)$.

The fundamental electrokinetic equations connecting them are [7, 103]: the Poisson equation for the relationship between the electric potential and the charge density,

$$\nabla^2 \Psi(\mathbf{r}, t) = -\frac{z_c e}{\epsilon_0 \epsilon_{rs}} n_c(\mathbf{r}, t) \tag{2.1}$$

the Navier-Stokes equation for the fluid velocity for low Reynolds number in the presence of an electrical body force,

$$\eta \nabla^2 \mathbf{v}(\mathbf{r}, t) - \nabla P(\mathbf{r}, t) - z_c e n_c(\mathbf{r}, t) \nabla \Psi(\mathbf{r}, t) = \rho_s \frac{\partial}{\partial t}[\mathbf{v}(\mathbf{r}, t) + \mathbf{v}_e \, \mathrm{e}^{-i\omega t}] \tag{2.2}$$

the continuity equation for the counterions that implies the conservation of the number of counterions in the system,

$$\nabla \cdot [n_c(\mathbf{r}, t)\mathbf{v}_c(\mathbf{r}, t)] = -\frac{\partial}{\partial t}[n_c(\mathbf{r}, t)] \tag{2.3}$$

and the Nernst-Planck equation for the flow of the counterions,

$$n_c(\mathbf{r}, t)\mathbf{v}_c(\mathbf{r}, t) = n_c(\mathbf{r}, t)\mathbf{v}(\mathbf{r}, t) - \frac{1}{\lambda_c} n_c(\mathbf{r}, t)\nabla \mu_c(\mathbf{r}, t) \tag{2.4}$$

where $\mu_c(\mathbf{r}, t)$ is the electrochemical potential of the counterions. We also take into account the continuity equation for an incompressible fluid flow,

$$\nabla \cdot \mathbf{v}(\mathbf{r}, t) = 0 \tag{2.5}$$

In these equations, ϵ_0 is the vacuum permittivity and e is the elementary electric charge. The drag coefficient λ_c is related to the limiting ionic conductance Λ_c^0 or the diffusion coefficient D_c by

$$\lambda_c = \frac{N_A e^2 |z_c|}{\Lambda_c^0} = \frac{k_B T}{D_c} \tag{2.6}$$

where N_A is Avogadro's number, k_B is Boltzmann's constant, and T is the absolute temperature.

As we are interested in studying the linear response of the system to an electric field, we apply a perturbation scheme. Thus, each quantity X is written as the sum of its equilibrium value, X^0, plus a perturbation term, δX, linearly dependent with the field multiplied by the term $\mathrm{e}^{-i\omega t}$, that

represents the time dependent sinusoidal response of the stationary state:

$$\Psi(\mathbf{r}, t) = \Psi^0(r) + \delta\Psi(\mathbf{r})\mathrm{e}^{-i\omega t}$$
$$n_c(\mathbf{r}, t) = n_c^0(r) + \delta n_c(\mathbf{r})\mathrm{e}^{-i\omega t}$$
$$\mu_c(\mathbf{r}, t) = \mu_c^0 + \delta\mu_c(\mathbf{r})\mathrm{e}^{-i\omega t}$$
$$P(\mathbf{r}, t) = P^0(r) + P(\mathbf{r})\mathrm{e}^{-i\omega t}$$
$$\mathbf{v}(\mathbf{r}, t) = \mathbf{v}(\mathbf{r})\mathrm{e}^{-i\omega t}$$
$$\mathbf{v}_c(\mathbf{r}, t) = \mathbf{v}_c(\mathbf{r})\mathrm{e}^{-i\omega t} \tag{2.7}$$

We introduce the finite size of the counterions by adding a new term, the entropy of the solvent molecules, in the free energy of the suspension [38,53]. Within a mean-field approximation, the total free energy of the system, $F = U - TS$, can be written in terms of the equilibrium electric potential $\Psi^0(\mathbf{r})$ and the counterions concentration $n_c^0(\mathbf{r})$. The configurational internal energy contribution U is

$$U = \int \mathrm{d}\mathbf{r} \left[-\frac{\epsilon_0\epsilon_{rs}}{2}|\nabla\Psi^0(\mathbf{r})|^2 + z_c e n_c^0(\mathbf{r})\Psi^0(\mathbf{r}) - \mu_c^0 n_c^0(\mathbf{r}) \right] \tag{2.8}$$

The first term is the self-energy of the electric field, the second term is the electrostatic energy of the counterions in the electrostatic mean field, and the last term couples the system to a bulk reservoir.

The entropic contribution $-TS$ is

$$-TS = k_B T n_c^{max} \int \mathrm{d}\mathbf{r} \left[\frac{n_c^0(\mathbf{r})}{n_c^{max}} \ln\left(\frac{n_c^0(\mathbf{r})}{n_c^{max}}\right) \right.$$
$$\left. + \left(1 - \frac{n_c^0(\mathbf{r})}{n_c^{max}}\right) \ln\left(1 - \frac{n_c^0(\mathbf{r})}{n_c^{max}}\right) \right] \tag{2.9}$$

being n_c^{max} the maximum possible concentration of counterions due to the excluded volume effect, defined as $n_c^{max} = V^{-1}$, where V is the average volume occupied by an ion in the solution. The first term inside the integral is the entropy of the counterions, and the second one is the entropy of the solvent molecules. This last term accounts for the ion size effect that modifies the classical Poisson-Boltzmann equation and was proposed earlier by Borukhov $et\ al.$ [38].

The variation of the free energy $F = U - TS$ with respect to $\Psi^0(\mathbf{r})$ provides the Poisson equation for the equilibrium

$$\nabla^2\Psi^0(\mathbf{r}) = -\frac{z_c e}{\epsilon_0\epsilon_{rs}}n_c^0(\mathbf{r}) \tag{2.10}$$

and the equilibrium counterions concentration is obtained performing the variation of the free energy with respect to $n_c^0(\mathbf{r})$

$$n_c^0(\mathbf{r}) = \frac{b_c \exp\left(-\frac{z_c e \Psi^0(\mathbf{r})}{k_B T}\right)}{1 + \frac{b_c}{n_c^{max}}\left[\exp\left(-\frac{z_c e \Psi^0(\mathbf{r})}{k_B T}\right) - 1\right]} \tag{2.11}$$

where b_c is an unknown coefficient that represents the ionic concentration where the electric potential is chosen to be zero.

We also get the equilibrium electrochemical potential doing the variation of the free energy with respect to $n_c^0(\mathbf{r})$ [46],

$$\mu_c^0(\mathbf{r}) = z_c e \Psi^0(\mathbf{r}) + k_B T \ln\left(\frac{\frac{n_c^0(\mathbf{r})}{n_c^{max}}}{1 - \frac{n_c^0(\mathbf{r})}{n_c^{max}}}\right) \tag{2.12}$$

In the case of equilibrium there is no external field and the particle is surrounded by a spherically symmetrical charge distribution. Applying this symmetry and combining Eqs. 2.10 and 2.11, we obtain a modified Poisson-Boltzmann equation for the equilibrium electric potential

$$\frac{\mathrm{d}^2 \Psi^0(r)}{\mathrm{d}r^2} + \frac{2}{r}\frac{\mathrm{d}\Psi^0(r)}{\mathrm{d}r} = -\frac{z_c e}{\epsilon_0 \epsilon_{rs}} \frac{b_c \exp\left(-\frac{z_c e \Psi^0(r)}{k_B T}\right)}{1 + \frac{b_c}{n_c^{max}}\left[\exp\left(-\frac{z_c e \Psi^0(r)}{k_B T}\right) - 1\right]} \tag{2.13}$$

In addition, the electroneutrality of the cell implies that

$$Q = 4\pi a^2 \sigma = -4\pi z_c e \int_a^b n_c^0(r) r^2 \mathrm{d}r \tag{2.14}$$

which is a necessary expression for the iterative calculation of the unknown b_c coefficient. Ruiz-Reina and Carrique recently shown that this problem can be solve avoiding the iterative procedure [70]. For this purpose, we use dimensionless variables, which are defined as

$$x = \frac{r}{a} \qquad \tilde{\Psi}^0(x) = \frac{e\Psi^0(r)}{k_B T} \qquad \tilde{\sigma} = \frac{ea}{\epsilon_0 \epsilon_{rs} k_B T}\sigma$$

$$\tilde{b}_c = \frac{e^2 a^2}{\epsilon_0 \epsilon_{rs} k_B T}b_c \qquad \tilde{n}_c^{max} = \frac{e^2 a^2}{\epsilon_0 \epsilon_{rs} k_B T}n_c^{max} \tag{2.15}$$

and rewrite Eq. 2.13 as

$$g(x) \equiv \frac{\mathrm{d}^2 \tilde{\Psi}^0(x)}{\mathrm{d}x^2} + \frac{2}{x}\frac{\mathrm{d}\tilde{\Psi}^0(x)}{\mathrm{d}x} = \frac{-z_c \tilde{b}_c e^{-z_c \tilde{\Psi}^0(x)}}{1 + \frac{\tilde{b}_c}{\tilde{n}_c^{max}}\left(e^{-z_c \tilde{\Psi}^0(x)} - 1\right)} \tag{2.16}$$

where we have defined the function $g(x)$. If we differentiate it, after a little algebra, it is possible to eliminate the unknown coefficient $\tilde{b}_c$ and find that

$$g'(x) + z_c g(x)\tilde{\Psi}'(x) + \frac{1}{\tilde{n}_c^{max}}g^2(x)\tilde{\Psi}'(x) = 0 \qquad (2.17)$$

where the prime stands for differentiation with respect to x. In terms of the electric potential Eq. 2.17 is rewritten as

$$\tilde{\Psi}^{0'''}(x) + \frac{2}{x}\tilde{\Psi}^{0''}(x) - \frac{2}{x^2}\tilde{\Psi}^{0'}(x)$$
$$+ \tilde{\Psi}^{0'}(x)\left(\tilde{\Psi}^{0''}(x) + \frac{2}{x}\tilde{\Psi}^{0'}(x)\right)$$
$$\times \left[z_c + \frac{1}{\tilde{n}_c^{max}}\left(\tilde{\Psi}^{0''}(x) + \frac{2}{x}\tilde{\Psi}^{0'}(x)\right)\right] = 0 \quad (2.18)$$

We solve this third order differential equation instead of Eq. 2.13 to avoid the iterative process. An interested reader can find more details about the modified Poisson-Boltzmann equation for the equilibrium in Ref. [53].

As indicated before, it is convenient to write the non-equilibrium quantities in terms of their equilibrium values plus a field-dependent perturbation. The symmetry of the problem allows us to define the functions $h(r)$, $\phi_c(r)$, and $Y(r)$ [104]

$$\mathbf{v}(\mathbf{r}) = (v_r, v_\theta, v_\varphi) = \left(-\frac{2}{r}h(r)E\cos\theta, \frac{1}{r}\frac{\mathrm{d}}{\mathrm{d}r}(rh(r))E\sin\theta, 0\right) \qquad (2.19)$$

$$\delta\mu_c(\mathbf{r}) = -z_c e\phi_c(r)E\cos\theta \qquad (2.20)$$

$$\delta\Psi(\mathbf{r}) = -Y(r)E\cos\theta \qquad (2.21)$$

with $E = |\mathbf{E}|$.

Substituting into the differential electrokinetic equations, Eqs. 2.1 − 2.5, the above mentioned perturbation scheme, neglecting nonlinear perturbations terms, and making use of the symmetry conditions of the problem we obtain

$$\mathcal{L}(\mathcal{L}h(r)) + \frac{i\omega\rho_s}{\eta}\mathcal{L}h(r) = -\frac{z_c e^2}{k_B T \eta r}$$
$$\times \left(\frac{\mathrm{d}\Psi^0(r)}{\mathrm{d}r}\right)n_c^0(r)\left(\phi_c(r) - \frac{n_c^0(r)}{n_c^{max}}Y(r)\right) \quad (2.22)$$

$$\mathcal{L}\phi_c(r) + \frac{i\omega\lambda_c}{k_B T}\left(\phi_c(r) - Y(r)\right) = \frac{e}{k_B T}\left(\frac{\mathrm{d}\Psi^0(r)}{\mathrm{d}r}\right)$$

$$\times \left(1 - \frac{n_c^0(r)}{n_c^{max}}\right)\left(z_c\frac{\mathrm{d}\phi_c(r)}{\mathrm{d}r} - \frac{2\lambda_c}{e}\frac{h(r)}{r}\right) \quad (2.23)$$

$$\mathcal{L}Y(r) = -\frac{z_c^2 e^2 n_c^0(r)}{\epsilon_0\epsilon_{rs}k_B T}\left(\phi_c(r) - Y(r)\right) \quad (2.24)$$

where the $\mathcal{L}$ operator is defined by

$$\mathcal{L} \equiv \frac{\mathrm{d}^2}{\mathrm{d}r^2} + \frac{2}{r}\frac{\mathrm{d}}{\mathrm{d}r} - \frac{2}{r^2} \quad (2.25)$$

According to Ref. [11], we incorporate a distance of closest approach of the counterions to the particle surface, resulting from their finite size. We assume that the counterions cannot come closer to the surface of the particle than their effective hydration radius, R, and therefore the ionic concentration will be zero in the region between the particle surface, $r = a$, and the spherical surface, $r = a + R$, defined by the counterion effective radius. This reasoning implies that counterions are considered as spheres of radius R with a point charge at their center.

With this consideration, we solve the electrokinetic equations, Eqs. 2.13, $2.22 - 2.24$, only between $r = a + R$ and $r = b$. When we address the problem in the region between $r = a$ and $r = a + R$, the equations to solve turn into the Laplace equation for the equilibrium electric potential, and equations $\mathcal{L}(\mathcal{L}h(r)) = 0$, $\phi_c(r) = 0$, and $\mathcal{L}Y(r) = 0$ for the rest of the spherical functions, because this region is free of charge. We call FIS+L model this complete model that includes ion size effects and also considers the distance of closest approach of the counterions to the charged particle surface.

We have presented a system of equations that accounts for the response of a salt-free suspension under alternating electric fields including ion size effects. If we are interested in the response under a static electric field, we only need to set $\omega = 0$ in the previous equations. Also, if we consider point-like counterions, $n_c^{max} = \infty$, we recover the expressions obtained by Carrique *et al.* [68].

2.1.2   Boundary conditions

We next specify the boundary conditions used for the resolution of the electrokinetic equations. In the case of the equilibrium electric potential,

we fix its origin at $r = b$, which results in

$$\Psi^0(b) = 0 \qquad (2.26)$$

Using the electroneutrality condition of the cell, Eq. 2.14, and the Gauss' theorem to the outer surface of the cell, we obtain

$$\left.\frac{\mathrm{d}\Psi^0(r)}{\mathrm{d}r}\right|_{r=b} = 0 \qquad (2.27)$$

On the other hand, specifying the electrical state of the particle, and applying Gauss' theorem to the outer side of the particle surface $r = a$ we get

$$\left.\frac{\mathrm{d}\Psi^0(r)}{\mathrm{d}r}\right|_{r=a} = -\frac{\sigma}{\epsilon_0 \epsilon_{rs}} \qquad (2.28)$$

We also force the equilibrium potential and its first derivative to be continuous at the surface $r = a + R$ defined by the counterion effective radius.

Regarding dilute suspensions, it is very common in the literature to use the surface charge (also regulated surface charge) or the surface potential as a boundary condition at the particle surface when solving the equilibrium Poisson-Boltzmann equation, and all of them are equally valid. When it comes to concentrated suspensions, we prefer the use of the particle surface charge as boundary condition by the following reasoning. The particle charge is a property that can be often measured experimentally. Instead, the surface potential depends on the choice of the potential origin, which is the solution "bulk" for the dilute case (see the discussion in Appendix A). As in the concentrated case there is not a clear "bulk", the origin is typically chosen at the outer surface of the cell, $r = b$, which depends on the particle volume fraction, Eq. 1.6. In any case, we always can use the surface potential as a boundary condition, representing the potential difference between the particle surface and the outer surface of the cell.

In the case of the electric potential out of equilibrium, the discontinuity of the normal component of the displacement vector at the particle surface states

$$\epsilon_{rs}\nabla\delta\Psi(\mathbf{r})\cdot\hat{\mathbf{r}}\big|_{r=a} - \epsilon_{rp}\nabla\delta\Psi_P(\mathbf{r})\cdot\hat{\mathbf{r}}\big|_{r=a} = 0 \qquad (2.29)$$

where $\delta\Psi_P(\mathbf{r})$ is the perturbed part of the electric potential in the interior region of the solid particle, and $\hat{\mathbf{r}}$ is the normal unit vector outward to the surface. Also, the continuity of the electric potential at the surface of the particle has to be considered

$$\delta\Psi(\mathbf{r})\big|_{r=a} = \delta\Psi_P(\mathbf{r})\big|_{r=a} \qquad (2.30)$$

According to Shilov-Zharkikh-Borkovskaya boundary conditions [95], the connection between the macroscopic experimentally measured electric field $\langle \mathbf{E} \rangle$ and local electric properties is

$$\delta \Psi(\mathbf{r})\big|_{r=b} = -\langle \mathbf{E} \rangle \cdot \mathbf{r}\big|_{r=b} \tag{2.31}$$

We also must impose the continuity of the electric potential out of equilibrium and of its first derivative at the boundary surface $r = a + R$.

Following again Shilov-Zharkikh-Borkovskaya boundary conditions, the ionic perturbation at the outer surface of the cell must be zero

$$\delta n_c(\mathbf{r})\big|_{r=b} = 0 \tag{2.32}$$

As the solid particles are impenetrable objects for the ions, the velocity of the ions in the normal direction to the particle surface is zero

$$\mathbf{v}_c(\mathbf{r}) \cdot \hat{\mathbf{r}}\big|_{r=a+R} = 0 \tag{2.33}$$

Due to the inclusion of a distance of closest approach of the counterions to the particle surface, the density of counterions $n_c(\mathbf{r}, t)$ and their drift velocity $\mathbf{v}_c(\mathbf{r}, t)$ will be discontinuous at the surface $r = a + R$, being zero in the region $[a, a + R]$ and non-zero in the region $[a + R, b]$.

The liquid located at the particle surface, $r = a$, is considered immobile, strongly attached to the particle. The latter fact that the liquid cannot slip on the particle is expressed as

$$\mathbf{v}(\mathbf{r})\big|_{r=a} = 0 \tag{2.34}$$

At the outer surface of the cell, $r = b$, we follow Kuwabara's boundary conditions [105]. In the radial direction, the velocity of the liquid far from the particle will be the negative of the radial component of the electrophoretic velocity

$$\mathbf{v}(\mathbf{r}) \cdot \hat{\mathbf{r}}\big|_{r=b} = -\mathbf{v}_e(\mathbf{r}) \cdot \hat{\mathbf{r}}\big|_{r=b} \tag{2.35}$$

According also to Kuwabara, the fluid flow is free of vorticity at the outer surface of the cell

$$\nabla \times \mathbf{v}(\mathbf{r})\big|_{r=b} = 0 \tag{2.36}$$

At the boundary surface $r = a + R$ we must consider the continuity of the normal and tangential components of the fluid velocity as well as the continuity of vorticity and pressure [106].

Finally, we need to know the net force acting on the particle or the unit cell. Details of the net force calculation can be found in Ref. [104] or Appendix 1 in Ref. [68].

In terms of the radial functions $\Psi^0(r)$, $Y(r)$, $\phi_c(r)$ and $h(r)$, the boundary conditions change into:

(i) at the particle surface $r = a$

$$\left. \frac{\mathrm{d}\Psi^0(r)}{\mathrm{d}r} \right|_{r=a} = -\frac{\sigma}{\epsilon_0 \epsilon_{rs}} \tag{2.37}$$

$$\left. \frac{\mathrm{d}Y(r)}{\mathrm{d}r} \right|_{r=a} - \frac{\epsilon_{rp}}{\epsilon_{rs}} \frac{Y(a)}{a} = 0 \tag{2.38}$$

$$h(a) = 0 \tag{2.39}$$

$$\left. \frac{\mathrm{d}h(r)}{\mathrm{d}r} \right|_{r=a} = 0 \tag{2.40}$$

(ii) at the surface $r = a + R$ defined by the counterion effective radius

$$\Psi^0(a + R^-) = \Psi^0(a + R^+) \tag{2.41}$$

$$\left. \frac{\mathrm{d}\Psi^0(r)}{\mathrm{d}r} \right|_{r=a+R^-} = \left. \frac{\mathrm{d}\Psi^0(r)}{\mathrm{d}r} \right|_{r=a+R^+} \tag{2.42}$$

$$Y(a + R^-) = Y(a + R^+) \tag{2.43}$$

$$\left. \frac{\mathrm{d}Y(r)}{\mathrm{d}r} \right|_{r=a+R^-} = \left. \frac{\mathrm{d}Y(r)}{\mathrm{d}r} \right|_{r=a+R^+} \tag{2.44}$$

$$\left. \frac{\mathrm{d}\phi_c(r)}{\mathrm{d}r} \right|_{r=a+R^+} = 0 \tag{2.45}$$

$$h(a + R^-) = h(a + R^+) \tag{2.46}$$

$$\left. \frac{\mathrm{d}h(r)}{\mathrm{d}r} \right|_{r=a+R^-} = \left. \frac{\mathrm{d}h(r)}{\mathrm{d}r} \right|_{r=a+R^+} \tag{2.47}$$

$$\mathcal{L}h(a + R^-) = \mathcal{L}h(a + R^+) \tag{2.48}$$

$$\left. \frac{\mathrm{d}^3 h(r)}{\mathrm{d}r^3} \right|_{r=a+R^-} = \left. \frac{\mathrm{d}^3 h(r)}{\mathrm{d}r^3} \right|_{r=a+R^+} - \frac{z_c e}{(a + R)\eta} n_c^0(a + R^+) Y(a + R^+) \tag{2.49}$$

(iii) and finally, at the outer surface of the cell $r = b$

$$\Psi^0(b) = 0 \tag{2.50}$$

$$\frac{\mathrm{d}\Psi^0(r)}{\mathrm{d}r}\bigg|_{r=b} = 0 \tag{2.51}$$

$$Y(b) = b \tag{2.52}$$

$$\phi_c(b) = b \tag{2.53}$$

$$\mathcal{L}h(b) = 0 \tag{2.54}$$

$$\eta\frac{\mathrm{d}}{\mathrm{d}r}\big[r\mathcal{L}h(r)\big]_{r=b} - z_c eb_c Y(b)$$
$$= i\omega\rho_s\left(h(b) - 2\phi\frac{\rho_p - \rho_s}{\rho_s}h(b) - b\frac{\mathrm{d}h(r)}{\mathrm{d}r}\bigg|_{r=b}\right) \tag{2.55}$$

This last boundary condition, Eq. 2.55, stands for the equation of motion of the unit cell. The boundary conditions for the case of static electric fields are a particularization of the previous ones with $\omega = 0$.

2.2 Method

We will discuss the results of the FIS+L electrokinetic model. In order to show the realm of the finite ion size effect in salt-free suspensions, the results are compared with the standard predictions for point-like ions, PL model [67–69]. The electrokinetic equations with their boundary conditions form a boundary value problem that can be solved numerically using the MATLAB routine bvp4c [107].

For the sake of simplicity, we assume that the average volume occupied by a counterion is $V = (2R)^3$, being $2R$ the counterion effective diameter. With this consideration, the maximum possible concentration of counterions due to the excluded volume effect is $n_c^{max} = (2R)^{-3}$. This corresponds to a simple cubic package (52% packing). In molar concentrations, the values used in the calculations, $n_c^{max} = 22$, 4 and 1.7 M, correspond approximately to counterion effective diameters of $2R = 0.425$, 0.75 and 1 nm,

Table 2.1: Parameter values used in the calculations.

$T = 298.15$ K	$a = 100$ nm
$\eta = 0.89{\cdot}10^{-3}$ P	$z_c = +1$
$\epsilon_{rs} = 78.55$	$D_c = 9.34{\cdot}10^{-9}$ m^2/s
$\epsilon_{rp} = 2$	

respectively. These are typical hydrated ionic diameters [108]. We present in Table 2.1 the parameter values used in all the calculations. The chosen parameters correspond to hydrated H^+ counterions, which are commonly found in many experimental conditions with salt-free suspensions of, for example, negatively charged sulfonated particles, due to the cleaning process of the suspension with proton exchange resins.

2.3 Calculated quantities

2.3.1 Electrophoretic mobility

The dynamic electrophoretic mobility μ of a spherical particle in a concentrated colloidal suspension can be defined from the relation between the electrophoretic velocity of the particle $\mathbf{v}_e e^{-i\omega t}$ and the macroscopic electric field $\langle \mathbf{E} \rangle e^{-i\omega t}$, which is given by

$$\langle \mathbf{E} \rangle = -\frac{1}{V_{cell}} \int_{V_{cell}} \nabla \delta \Psi(\mathbf{r}) \mathrm{d}V \tag{2.56}$$

From the boundary condition Eq. 2.35, the definition $\mathbf{v}_e = \mu \langle \mathbf{E} \rangle$, and making use of the symmetry conditions of the problem, Eq. 2.19, we obtain

$$\mu = \frac{2h(b)}{b} \tag{2.57}$$

As usual, the mobility data will be scaled as

$$\mu^* = \frac{3\eta e}{2\epsilon_0 \epsilon_{rs} k_B T} \mu \tag{2.58}$$

where μ^* is the nondimensional dynamic electrophoretic mobility. For the case of a static electric field, if we impose $\omega = 0$ in the electrokinetic equations, Eq. 2.57 will give us the low frequency limit of the dynamic electrophoretic mobility, simply known as electrophoretic mobility.

2.3.2 Conductivity and dielectric response

The complex conductivity, K, of the suspension is usually defined in terms of the volume averages of the local electric current density and electric field in a cell representing the whole suspension.

$$\langle \mathbf{J} \rangle = \frac{1}{V_{cell}} \int_{V_{cell}} \mathbf{J}(\mathbf{r}) \mathrm{d}V = K \langle \mathbf{E} \rangle \tag{2.59}$$

where $\langle \mathbf{E} \rangle \mathrm{e}^{-i\omega t}$ is the macroscopic electric field, and $\mathbf{J}(\mathbf{r}, t) = \mathbf{J}(\mathbf{r})\mathrm{e}^{-i\omega t}$ is the electric current density of a salt-free suspension, equal to the sum of the conduction and displacement terms

$$\mathbf{J}(\mathbf{r}, t) = z_c e n_c(\mathbf{r}, t)\mathbf{v}_c(\mathbf{r}, t) + \frac{\partial \mathbf{D}(\mathbf{r}, t)}{\partial t} \qquad (2.60)$$

or in terms of the perturbation quantities

$$\mathbf{J}(\mathbf{r}) = z_c e n_c^0(\mathbf{r})\mathbf{v}_c(\mathbf{r}) - i\omega \mathbf{D}(\mathbf{r}) \qquad (2.61)$$

Following a similar procedure to that described for the complex conductivity of suspensions in salt solutions in Ref. [96] and using Shilov-Zharkikh-Borkovskaya boundary conditions [95], we obtain (see also Ref. [69])

$$K = \left(\frac{z_c^2 e^2}{\lambda_c} \frac{\mathrm{d}\phi_c(r)}{\mathrm{d}r} \bigg|_{r=b} - \frac{2h(b)}{b} z_c e \right) n_c^0(b) - i\omega \epsilon_{rs} \epsilon_0 \frac{\mathrm{d}Y(r)}{\mathrm{d}r} \bigg|_{r=b} \qquad (2.62)$$

For the case of a static electric field, $\omega = 0$, Eq. 2.62 turns into

$$K = \left(\frac{z_c^2 e^2}{\lambda_c} \frac{\mathrm{d}\phi_c(r)}{\mathrm{d}r} \bigg|_{r=b} - \frac{2h(b)}{b} z_c e \right) n_c^0(b) \qquad (2.63)$$

that gives us the conductivity of the suspension. This expression is also the low frequency limit of real part of the complex conductivity.

From the complex conductivity, the real $\epsilon_r'(\omega)$ and imaginary $\epsilon_r''(\omega)$ components of the complex relative permittivity of the suspension $\epsilon_r(\omega)$ are calculated by writing

$$K(\omega) = K(\omega = 0) - i\omega\epsilon_0\epsilon_r(\omega) = K(\omega = 0) + \omega\epsilon_0\epsilon_r''(\omega) - i\omega\epsilon_0\epsilon_r'(\omega) \quad (2.64)$$

$$\epsilon_r'(\omega) = -\frac{\mathrm{Im}[K(\omega)]}{\omega\epsilon_0} \qquad (2.65)$$

$$\epsilon_r''(\omega) = \frac{\mathrm{Re}[K(\omega)] - K(\omega = 0)}{\omega\epsilon_0} \qquad (2.66)$$

2.4   Results: equilibrium electric double layer

In this section we show the results for the equilibrium electric double layer in salt-free concentrated suspensions including ion size effects by calculating the equilibrium electric potential, $\Psi^0(r)$, and the equilibrium counterions concentration, $n_c^0(r)$.

Fig. 2.1 shows the dimensionless equilibrium electric potential distribution, Fig. 2.1a, and the counterions concentration profiles, Fig. 2.1b, along the cell. We compare the results of the FIS+L model for different counterions sizes (different dashed colored lines) with those of the PL model (solid black line). The particle surface charge density have been chosen equal to $-40 \ \mu C/cm^2$ and the particle volume fraction is $\phi = 0.5$ (very concentrated suspension), which implies a normalized cell size of $b/a = 1.26$.

We observe in Fig. 2.1a that the inclusion of ion size effects always rises the surface electric potential in comparison with the point-like predictions, which are recovered in the limit of point-like counterions ($n_c^{max} = \infty$). The reason is that the limitation of the counterions concentration in the vicinity of the particle significantly diminishes the screening of the particle
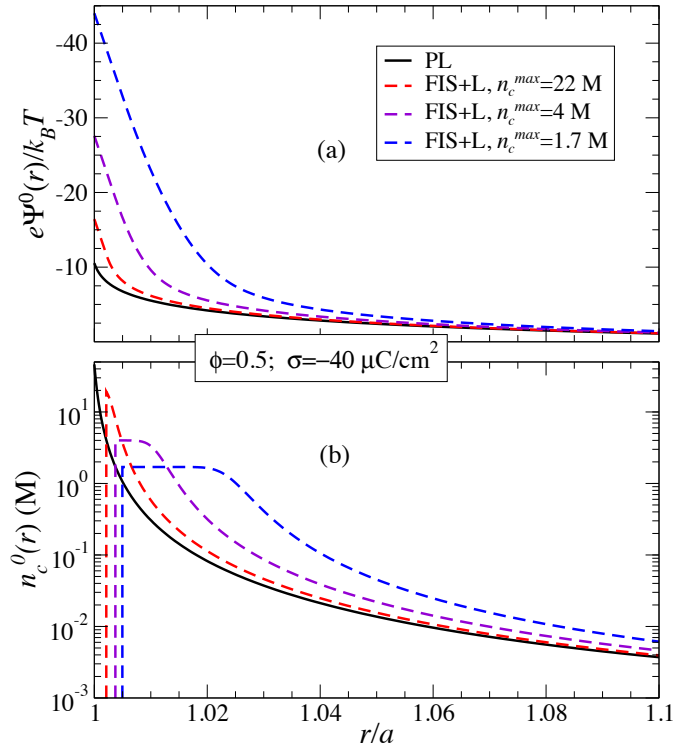

Figure 2.1: Dimensionless electric potential distribution (a) and counterions concentration (b) along the cell. Dashed lines present the results of the FIS+L model. Different colors stand for different counterion sizes. Solid black lines show the results for point-like counterions.
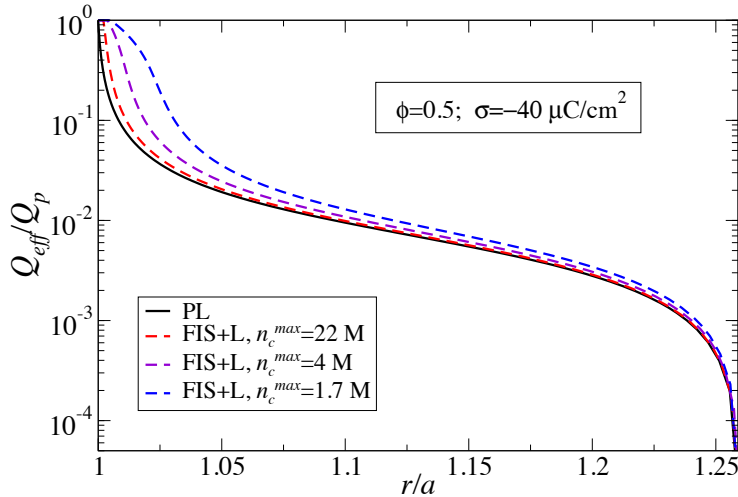
Figure 2.2: Effective charge divided by the particle charge along the cell. Dashed lines present the results of the FIS+L model. Different colors stand for different counterion sizes. Solid black lines show the results for point-like counterions.

charge, which consequently increases the surface potential. We can also see in Fig. 2.1b how ion size effects create saturated regions which corresponds to plateaus in the counterions concentration profiles. These saturated regions, and therefore also the increment in the surface potential, are higher the higher the ion size, or analogously the lower n_c^{max}.

Fig. 2.2 shows the effective charge divided by the particle charge along the cell for a particle volume fraction $\phi = 0.5$. We compare the results of the FIS+L model for different counterions sizes (different dashed colored lines) with those of the PL model (solid black line). The effective charge is the charge seen at a given radial distance from the center of the particle which includes the own particle charge and the ionic volume charge density in the double layer integrated from the particle surface to the r distance [71]. From this definition, the ratio Q_{eff}/Q_p is equal to one at the surface of the particle and zero at the outer surface of the cell due to its electroneutrality. The results of this figure reinforced those discussed previously in Fig. 2.1. As expected, the larger the ion size, the lower the screening of the particle charge.

Fig. 2.3 displays the dimensionless equilibrium surface electric potential for a wide range of particle surface charge densities, Fig. 2.3a, and
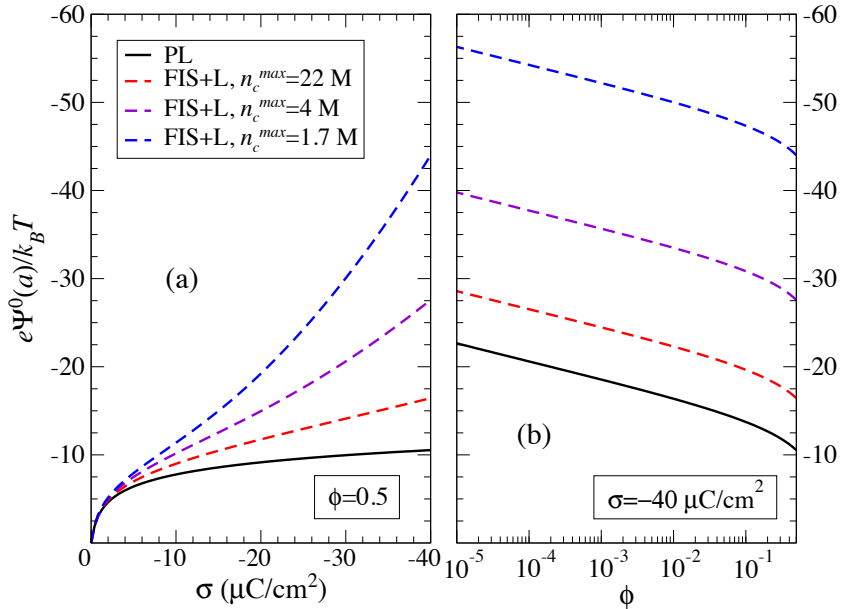
Figure 2.3: Dimensionless surface electric potential for different values of particle surface charge density (a) and particle volume fraction (b). Dashed lines present the results of the FIS+L model. Different colors stand for different counterion sizes. Solid black lines show the results for point-like counterions.

particle volume fractions, Fig. 2.3b. We repeat this study for different counterion sizes (different colored dashed lines) and for point-like counterions (black solid line). We find that the surface electric potential increases with the particle charge density, Fig. 2.3a. However, in some cases there is a different behavior in comparison with the point-like case. Initially, a fast and rough increase of the surface potential with the surface charge density is observed, which is followed by a much slower growth at higher surface charge densities for the PL case or when the size of the counterions is very small. This phenomenon is related to the classical counterion condensation effect: for high surface charges a layer of counterions develops very close to the particle surface [64, 109]. When the ion size is taken into account we limit the appearance of the classical condensation effect. The reason is that the additional counterions join the condensate enlarging it when the surface charge is increased. This explains the further increase of the surface potential observed for large ion sizes and high surface charges densities.
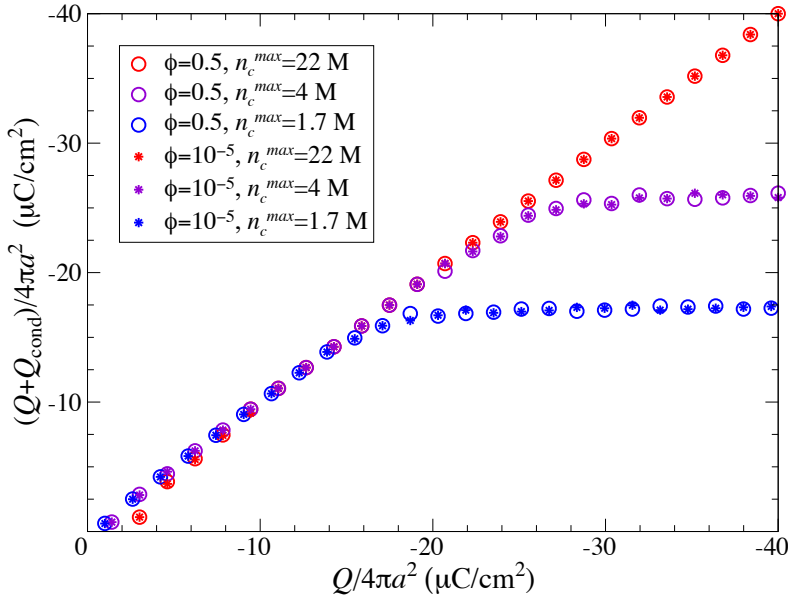
Figure 2.4: Particle charge density plus charge accumulated in the counterions condensate versus particle charge. Different colors stand for different counterion sizes within the FIS+L model. Open circles and stars symbols show the results for $\phi = 0.5$ and $\phi = 10^{-5}$, respectively. All results are divided by $4\pi a^2$.

On the other hand, the surface electric potential decreases when the particle volume fraction increases, irrespectively of the case studied: PL or FIS+L models, Fig. 2.3b. When the particle concentration raises, the available space for the counterions inside the cell decreases and, consequently, the screening of the particle charge largely augments, thus reducing the value of the surface potential.

We show in Fig. 2.4 the sum of the particle charge, Q, and the charge accumulated in the counterions condensate, Q_{cond}, as a function of particle charge. All the results are divided by $4\pi a^2$ (with $a = 100$ nm). We repeat this study for different ion sizes within the FIS+L model and for two different volume fractions in the concentrated and dilute limits. We observe a linear relation between Q and $Q + Q_{\mathrm{cond}}$ that is only kept for low particle charges as the ion size increases. This is because when both the ion size and charge are high enough, the counterions tend to locate mostly in the vicinity of the particle surface, creating a condensate (see Fig. 2.1). From this

point, as the particle charge is increased, the additional counterions join and enlarge the condensate. This is shown in the plateau that appears for moderate to high particle charges. The value of σ from which the counterions start to condensate is lower the larger the ion size, as expected. Besides, we note that the counterions condensation is independent of the particle volume fraction (open circles and stars symbols are almost coincident for every particle charge). All these results confirm those from Fig. 2.3.

The results from Fig. 2.4 should be considered qualitatively. The exact charge value from which the condensate is formed as well as the magnitude of the plateaus are strongly dependent on the definition of the condensate. For these calculations we have considered that the condensate ends at the point in which the counterions concentration differs 1% from its concentration in the plateau (see Fig. 2.1). The deviations found at low particle charge are due to this definition.

From the results, we think that it is clear that the influence of the finite ion size effects on the EDL description cannot be neglected for many typical particle charges and volume fractions.

2.5 Results: dc electrokinetics

Now we analyze the response of a salt-free concentrated suspension including ion size effects to an external static electric field. Once the FIS+L model presented in Section 2.1 is solved for $\omega = 0$, we calculate the electrophoretic mobility of the particles and the conductivity of the suspension. The discussion of the results is presented in the two following subsections.

2.5.1 Electrophoretic mobility

The classical behavior of the electrophoretic mobility of spherical particles in salt-free concentrated suspensions when we consider point-like counterions, PL model, is as follows: for low particle surface charges, there is a large increment of the electrophoretic mobility with the surface charge. When the particle volume fraction decreases, this increment is even larger. This behavior satisfies a Hückel law linearly connecting both magnitudes. When the particle charge is further increased, the electrophoretic mobility reaches a plateau and becomes practically independent of particle charge. This fact has been associated with the generation of a condensation layer of counterions close to the particle surface [64, 109]. Between these regimes there is a maximum followed by a small diminution of the electrophoretic
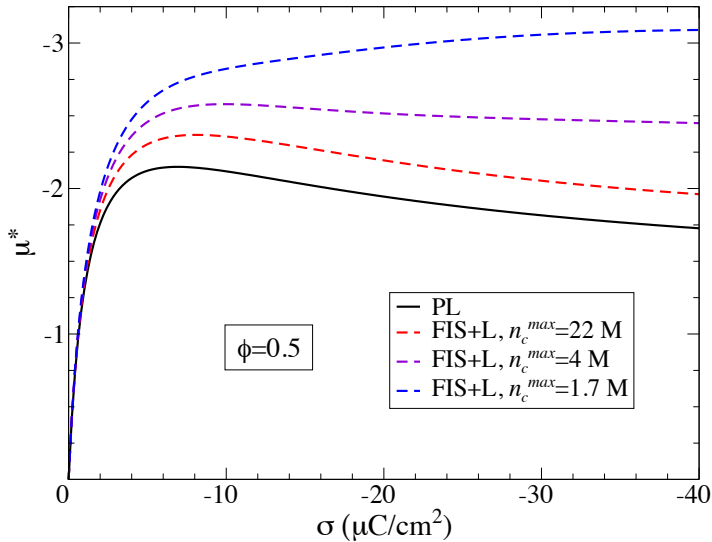
Figure 2.5: Scaled electrophoretic mobility against particle surface charge density. Dashed colored stand for the results of the FIS+L model for different counterion sizes. Solid black line show the result for point-like counterions.

mobility that depends on particle volume fraction. Also, the lower the particle volume fraction, the higher the electrophoretic mobility for every particle charge value. These classical behaviors are shown in solid black lines in Figs. 2.5 and 2.6. The results displayed in solid colored lines in Figs. 2.7 and 2.8 are also useful to understand this discussion.

If we take into account finite size counterions, FIS+L model, we find deviations from the point-like case. As we can see from the results of the dashed colored lines in Fig. 2.5, the small diminution passed the maximum in the electrophoretic mobility tends to disappear when the ion size becomes important. Moreover, if the size of the counterions is sufficiently large, also the maximum disappears. In this case we find two different regimes for the electrophoretic mobility upon changing the surface charge of the particles: the initial large increment of the mobility with the surface charge, similar to the one for point-like ions, now followed, for higher particle charges, by another region with a small rate of increment of the electrophoretic mobility.

When we study the behavior of the electrophoretic mobility when changing the particle volume fraction, we observe that the results of the FIS+L model differ from those for point-like ions, obtaining higher values of the
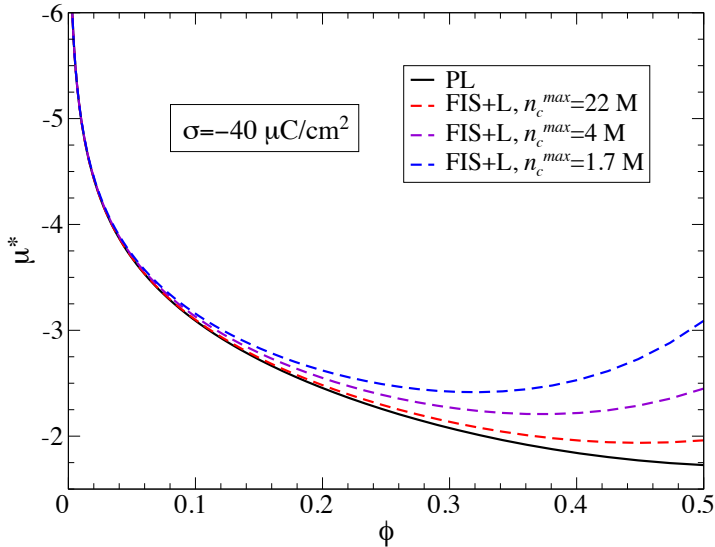
Figure 2.6: Scaled electrophoretic mobility against particle volume fraction. Dashed colored stand for the results of the FIS+L model for different counterion sizes. Solid black line show the result for point-like counterions.

mobility as we approach the concentrated regime, see dashed colored lines in Fig. 2.6. Also, if the ion size is sufficiently large, we can find a broad minimum at high particle volume fraction, in contrast with the PL case.

If the counterion size approaches to zero, or equivalently $n_c^{max} \to \infty$, the results of the FIS+L model approximate to those of the PL model in any case. Also, for low particle charges and low particle volume fractions the results of both models are nearly the same. For the remaining situations we always observe that the FIS+L model predicts higher values of the electrophoretic mobility than those calculated with the classical model for point-like ions, whatever the ion size.

As a main conclusion from Figs. 2.5 to 2.8, the consideration of finite ion size effects leads to an increase of the electrophoretic mobility over the PL case, using H^+ ions as counterions. As the ionic concentration in the cell has been altered, we will analyze the changes in the convective fluid flow, the counterions fluxes and the perturbed counterions concentration, as well as the overall forces and polarizations induced by the electric field for the FIS+L model in comparison with the PL case.
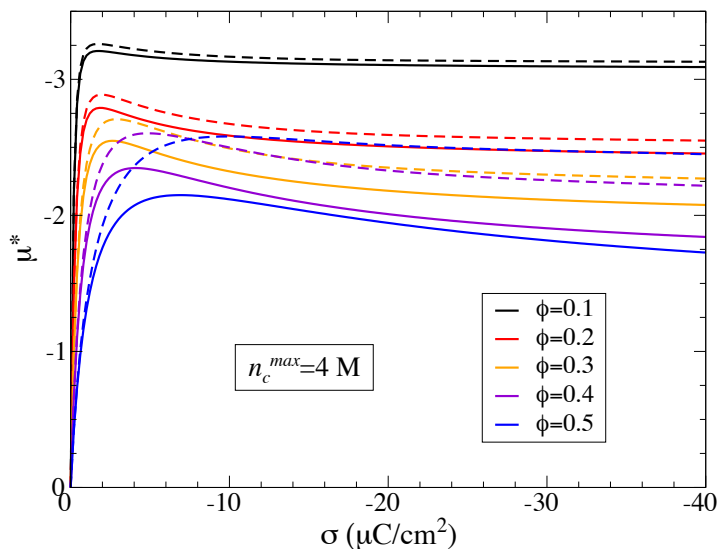
Figure 2.7: Scaled electrophoretic mobility against the surface charge density for different particle volume fraction values. Solid lines show the results for point-like ions. Dashed lines show the results of the FIS+L model with $n_c^{max} = 4$ M.
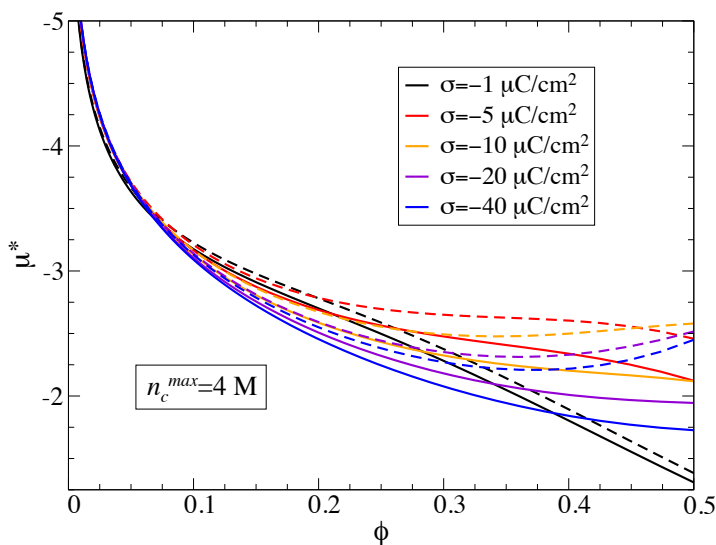

Figure 2.8: Scaled electrophoretic mobility against the particle volume fraction for different surface charge densities. Solid lines show the results for point-like ions. Dashed lines show the results of the FIS+L model with $n_c^{max} = 4$ M.
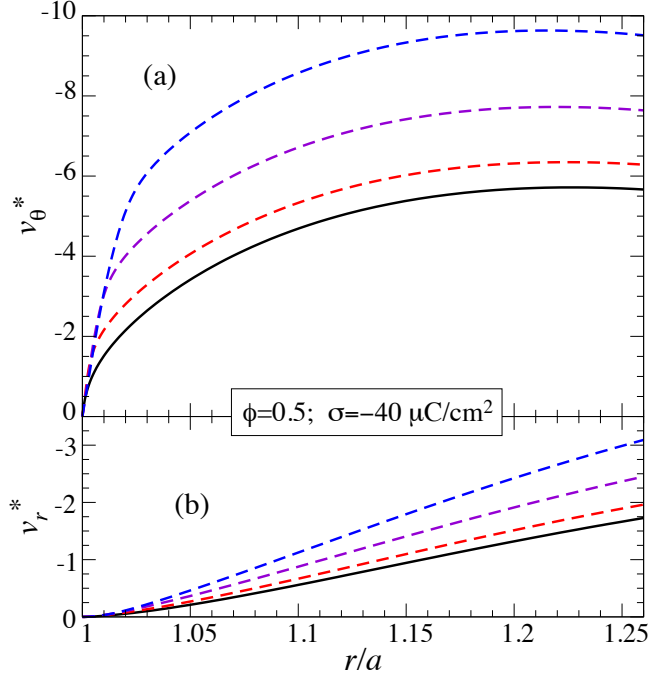
Figure 2.9: Scaled polar component of the fluid velocity over the particle equator $\theta = \pi/2$ (a), and scaled radial component of the fluid velocity at the front of the particle $\theta = \pi$ (b), along the cell for different ion sizes. Different lines have the same meaning than those shown in Fig. 2.5.

Fig. 2.9a shows the scaled polar component of the fluid velocity over the particle equator, $\theta = \pi/2$, and Fig. 2.9b presents the scaled radial component of the fluid velocity at the front of the particle, $\theta = \pi$, along the cell. Solid black lines represent the results of the PL model. Dashed colored lines stand for the results of the FIS+L model for different counterion sizes. The particle surface charge density has been chosen equal to $-40\ \mu C/cm^2$, and the particle volume fraction is $\phi = 0.5$, which implies a normalized cell size of $b/a = 1.26$. We define the scaled fluid velocity as

$$\mathbf{v}^*(\mathbf{r}) = \frac{3\eta e}{2\epsilon_0 \epsilon_{rs} k_B T E} \mathbf{v}(\mathbf{r}) \tag{2.67}$$

where the different components of $\mathbf{v}(\mathbf{r})$ can be obtained from Eq. 2.19. Both quantities, v_θ at $\pi/2$ and v_r at π, are of interest because they give us an idea of the magnitude of the electrophoretic velocity because they are antiparallel to it.
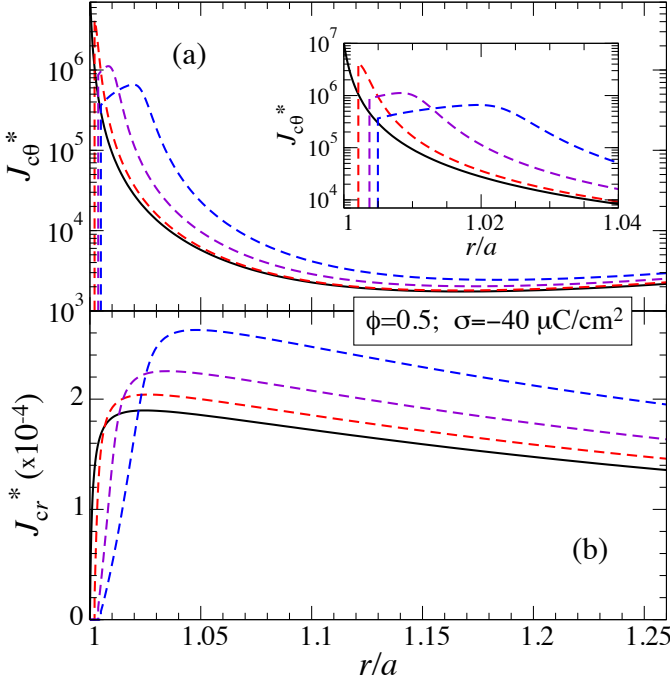
Figure 2.10: Scaled polar component of the flux of counterions over the particle equator $\theta = \pi/2$ (a), and scaled radial component of the flux of counterions at the front of the particle $\theta = \pi$ (b), along the cell for different ion sizes. Different lines have the same meaning than those shown in Fig. 2.5. In the inset of Fig. 2.10a we enlarge the region close to the particle surface.

We can see how the polar fluid velocity increases with the distance to the particle surface, with a high rate close to the particle surface, and diminishing it as we approximate to the outer surface of the cell. In the case of the radial component, there is a linear increase after an initial slower growth rate very close to the particle surface. This behavior is the same for the PL and FIS+L models. We also observe that the numerical values obtained with the FIS+L model are larger than those obtained with the PL model, in concordance with our predictions for the mobility.

Fig. 2.10a shows the scaled polar component of the counterions flux over the particle equator, $\theta = \pi/2$, and Fig. 2.10b presents the scaled radial component of the flux of the counterions at the front of the particle, $\theta = \pi$, along the cell. Different lines have the same meaning than in Fig. 2.9. We

define the scaled counterions flux as

$$\mathbf{J}_c^*(\mathbf{r}) = \frac{3\eta e^3 a^2}{2(\epsilon_0 \epsilon_{rs} k_B T)^2 E} \mathbf{J}_c(\mathbf{r}) \tag{2.68}$$

being $\mathbf{J}_c(\mathbf{r}) = n_c(\mathbf{r})\mathbf{v}_c(\mathbf{r})$, where $\mathbf{v}_c(\mathbf{r})$ is obtained from Eq. 2.4. We can see in Fig. 2.10 how the inclusion of finite ion size effects largely decreases the magnitude of the counterions fluxes close to the particle surface in both the polar and the radial directions in comparison with the PL case. In addition, the counterions fluxes are highly increased in the FIS+L case as we move away from the particle surface because now both the counterions concentration and the counterions velocity (not shown for brevity) reach higher values.

The enhancement of the fluid velocity observed in the FIS+L case in comparison with the PL model could be associated with the increment of the counterions fluxes in the region not in the immediate vicinity of the particle, because the ions have been expelled out due to the excluded volume effect, and consequently the electrical body force in that region is greater. However, as we can see in Table 2.2, the total electrical body force, $-F_e^*$, is lower in the FIS+L case, in comparison with the PL case. This is due to a very large diminution of the electrical body force very close to the particle when the finite ion size is taken into account, not only because ions have moved away from the vicinity of the particle surface but also for the remarkable diminution of the local electric field due to the increased induced electric polarization (see Table 2.2).

The total hydrodynamic and electric forces acting on the particle shown

Table 2.2: Scaled hydrodynamic, F_h^*, and electric, F_e^*, forces acting on the particle in the direction of the field. The total body force in the fluid is equal to $-F_e^*$ due to the electroneutrality of the cell. $\langle P_C \rangle^*$ and $\langle P_D \rangle^*$ are the scaled induced charge and dielectric polarizations in the direction of the field, respectively. All the calculations were performed at $\sigma = -40\mu C/cm^2$ and $\phi = 0.5$.

Model / n_c^{max}	F_h^*	F_e^*	$\langle P_C \rangle^*$	$\langle P_D \rangle^*$
PL	685	-696	346	-71.7
FIS+L / 22 M	524	-524	365	-73.1
FIS+L / 4 M	447	-447	386	-73.8
FIS+L / 1.7 M	394	-394	418	-74.2

in Table 2.2 can be calculated by

$$\mathbf{F}_h = \int_{S_p} \tilde{\sigma}^H \cdot \hat{\mathbf{r}} \; dS_p \tag{2.69}$$

$$\mathbf{F}_e = \int_{S_p} \tilde{\sigma}^M \cdot \hat{\mathbf{r}} \; dS_p \tag{2.70}$$

where S_p is the surface of the solid particle, and $\tilde{\sigma}^H$ and $\tilde{\sigma}^M$ are the hydrodynamic and the Maxwell stress tensors, respectively [9]. Evaluating these expressions, we obtain

$$\mathbf{F}_h = \frac{4}{3}\pi a^2 E \left[\eta a \frac{d^3 h}{dr^3}\bigg|_{r=a} + \eta \frac{d^2 h}{dr^2}\bigg|_{r=a} - z_c e n_c^0(a) Y(a) \right] \hat{\mathbf{k}} \tag{2.71}$$

$$\mathbf{F}_e = \frac{4}{3}\pi a^2 E \sigma \frac{Y(a)}{a} \left(\frac{\epsilon_{rp}}{\epsilon_{rs}} + 2 \right) \hat{\mathbf{k}} \tag{2.72}$$

where $\hat{\mathbf{k}}$ points to the direction of the macroscopic electric field. Both forces are scaled as follows

$$\mathbf{F}_{e,h}^* = \frac{3e}{4\pi a \epsilon_0 \epsilon_{rs} k_B T E} \mathbf{F}_{e,h} \tag{2.73}$$

The numerical values of the F_e^* are negative because this force has the opposite direction of the electric field for a negative particle. The hydrodynamic force opposes the movement of the particle and therefore has the direction of the field. In the stationary state the total force acting on the particle must be zero, as we can see by summing the values of both forces in Table 2.2. The small numerical discrepancies observed for the PL case can be removed by improving the mesh for the resolution of the electrokinetic equations very close to the particle surface although a large computational time is required.

It is worthwhile to mention that both the hydrodynamic and the electric forces calculated in Table 2.2 for the FIS+L model are lower than those of the PL case. The electric force acting on the particle has a driving and a relaxation contribution. As the driving force is constant in the study displayed in Table 2.2, the diminution of the total electric force is related with a change of the relaxation force as finite ion size is taken into account.

This relaxation force will depend on the electric dipole moment induced on the particle and its double layer by the electric field. A related quantity is the average induced dipole moment density whose components are: the

charge polarization, $\langle \mathbf{P}_C \rangle$, and the induced dipole moment density arising from the polarization of the dielectric continuum of the medium and the particles, $\langle \mathbf{P}_D \rangle$

$$\langle \mathbf{P}_C \rangle = \left\langle \frac{1}{V_{cell}} \int_{V_{cell}} \mathbf{r} z_c e \delta n_c(\mathbf{r}) \mathrm{d}V \right\rangle \tag{2.74}$$

$$\langle \mathbf{P}_D \rangle = \left\langle \frac{-1}{V_{cell}} \int_{V_{cell}} \mathbf{r}(\epsilon(\mathbf{r}) - \epsilon_0) \nabla \delta \Psi(\mathbf{r}) \mathrm{d}V \right\rangle \tag{2.75}$$

where

$$\epsilon(\mathbf{r}) = \begin{cases} \epsilon_{rp}\epsilon_0 & \mathbf{r} \in V_p \\ \\ \epsilon_{rs}\epsilon_0 & \mathbf{r} \in V_s \end{cases} \tag{2.76}$$

and V_p and V_s are the particle and solution volumes in the cell, respectively. According to the procedure developed for AC electric fields and point-like ions by Bradshaw-Hajek *et al.* [110], particularized to its DC limit and also accounting for the distance of closest approach of the counterions to the particle surface, the latter equations become

$$\langle \mathbf{P}_C \rangle = -\epsilon_0 \epsilon_{rs} \left[1 - \frac{\mathrm{d}Y}{\mathrm{d}r}\Big|_{r=b} + \left(\frac{a+R}{b} \right)^3 \right.$$
$$\left. \times \left(\frac{\mathrm{d}Y}{\mathrm{d}r}\Big|_{r=a+R^+} - \frac{Y(a+R^-)}{a+R} \right) \right] \langle \mathbf{E} \rangle \quad (2.77)$$

$$\langle \mathbf{P}_D \rangle = \epsilon_0 \left[(\epsilon_{rp} - \epsilon_{rs})\phi \frac{Y(a)}{a} + (\epsilon_{rs} - 1) \right] \langle \mathbf{E} \rangle \tag{2.78}$$

We show in Table 2.2 the scaled average polarization contributions, $\langle \mathbf{P}_C \rangle^*$ and $\langle \mathbf{P}_D \rangle^*$, calculated by

$$\langle \mathbf{P}_{C,D} \rangle^* = \frac{\langle \mathbf{P}_{C,D} \rangle}{\epsilon_0 E} \tag{2.79}$$

The charge polarization takes positive values and therefore the induced dipole moment generates an electric field which opposes the external one, thus penalizing the particle movement. On the contrary, the induced dipole moment due to the dielectric polarization has the opposite direction, reinforcing the effect of the external electric field on the particle movement. As the charge polarization contribution is considerably larger than the dielectric polarization one, see Table 2.2, the effect on the particle movement will be a net relaxation force that opposes the electric driving force, yielding a
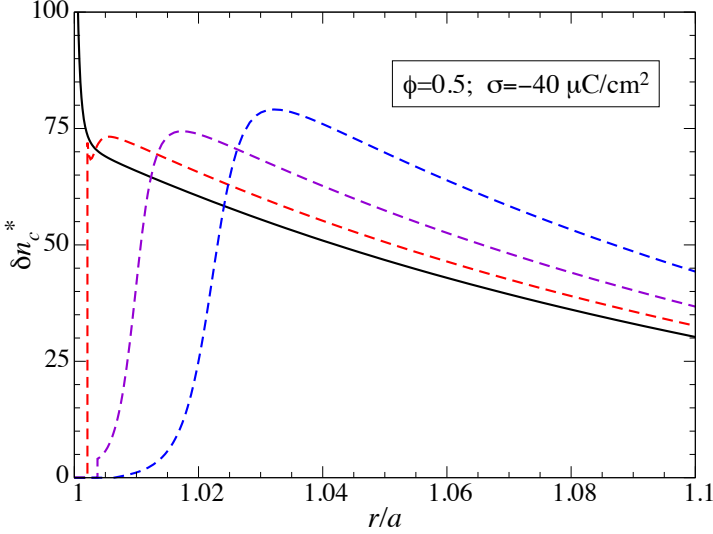
Figure 2.11: Scaled perturbed counterion concentration in the direction of the field ($\theta = 0$) along the cell for different ion sizes. Different lines have the same meaning than those in Fig. 2.5.

smaller total electric force in the FIS+L model, in comparison with the PL case (see Table 2.2).

In Fig. 2.11 we observe the scaled perturbed counterion concentration in the direction of the field ($\theta = 0$) along the cell. This quantity is responsible of the charge polarization contribution as we can see in Eq. 2.74. Solid black lines represent the results of the PL model. Dashed colored lines stand for the results of the FIS+L model for different counterion sizes. The perturbed counterion concentration is scaled as

$$\delta n_c^*(r) = \frac{ea}{\epsilon_0 \epsilon_{rs} E} \delta n_c(r) \tag{2.80}$$

where, using Eqs. 2.12, 2.20 and 2.21, we have

$$\delta n_c(r) = \frac{z_c e}{k_B T} n_c^0(r) \left(Y(r) - \phi_c(r) \right) E \cos\theta \tag{2.81}$$

We observe that the perturbed counterion concentration decreases asymptotically to zero at the outer surface of the cell ($b/a = 1.26$) in all cases according to Shilov-Zharkikh-Borkovskaya boundary condition, Eq. 2.32. In the PL case, we obtain an excess of counterions at the rear of the particle, $\theta = 0$, and a defect of counterions at the front of the particle, $\theta = \pi$, due

to a counterions migration from the front to the rear of the particle when the external electric field is applied. This excess of counterions is mainly located very close to the particle surface and generates an electric dipole moment that points to the direction of the electric field.

When we take into account finite size counterions, FIS+L model, the excess of counterions is lower near the particle surface in comparison with the PL case, see Fig. 2.11. As we noted in Fig. 2.1, the equilibrium concentration profile shows a counterions condensate that increases its width upon increasing the size of the counterions because of steric reasons. Therefore, when the external electric field is applied, the excess of counterions cannot be located in the condensate, full of counterions mainly for high particle charges. This is the reason why the main region of excess of counterions is now found at farther distances from the particle surface. Also, the consideration of an excluded region in contact with the particle makes the perturbed concentration profile to be shifted to larger distances from the particle surface as we see in Fig. 2.11. In all the cases studied, the charge contribution to the induced electric dipole moment points to the direction of the electric field which penalizes the movement of the particle by the relaxation effect [9].

According to Table 2.2, the charge polarization contribution is larger the larger the ion size. This fact is in concordance with an increase in the charge contribution to the induced electric dipole moment that we can associate to the charge redistribution depicted in Fig. 2.11 due to the excluded volume effect.

Summarizing, we have seen that when we introduce the ion size effects there is a remarkable diminution of the total electric force acting on the particle (see Table 2.2). This decrease grows with the ion size and with the inclusion of the excluded region. The diminution of the total electric force must be accompanied, in the stationary state, by a corresponding diminution of the total hydrodynamic force. According to the theory of classical electrokinetics [9], the total hydrodynamic force could be decomposed in a viscous drag and a electrophoretic retardation contribution. In this frame, the above mentioned decrease of the electric body force as ions size effects are considered produces a diminution of the electrophoretic retardation force, which opposes to the movement of the particle, as it happens in the FIS+L case. However, a complete explanation of the observed increase in the electrophoretic mobility will force us to study the transient regime after the application of the external field and the evolution of the different forces involved until the stationary state is reached. In the case we are concerned in
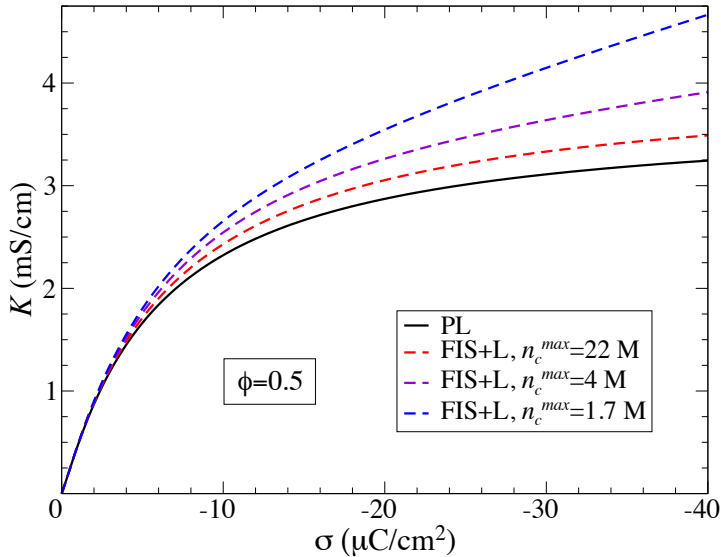
Figure 2.12: Electrical conductivity against particle surface charge density. Dashed lines stand for the results of the FIS+L model for different counterion sizes. Solid black line present the results for point-like counterions.

this work, the final result is that the electrophoretic mobility of the particle is higher in the FIS+L case in comparison with the PL model using H^+ ions as counterions, being these ions commonly found in many experimental salt-free suspensions. For other ionic species the behaviors observed can be different, depending on the diffusion coefficient of the ion, because the various contributions to the total force will be altered.

2.5.2   Electrical conductivity

The electrical conductivity of salt-free concentrated suspensions with point-like ions behaves classically as follows: the conductivity increases as surface charge density increases for any volume fraction [67]. For large particle charges, the conductivity tends to reach a plateau because of the classic counterion condensation effect [64, 109]: it appears that a critical particle charge density exists beyond which there is no appreciable influence on the conductivity. Once this critical charge value is attained, increasing the amount of counterions by raising the surface charge even more simply feeds the condensation region, where a high accumulation of counterions takes place close to the particle surface, leaving the charge and potential outside
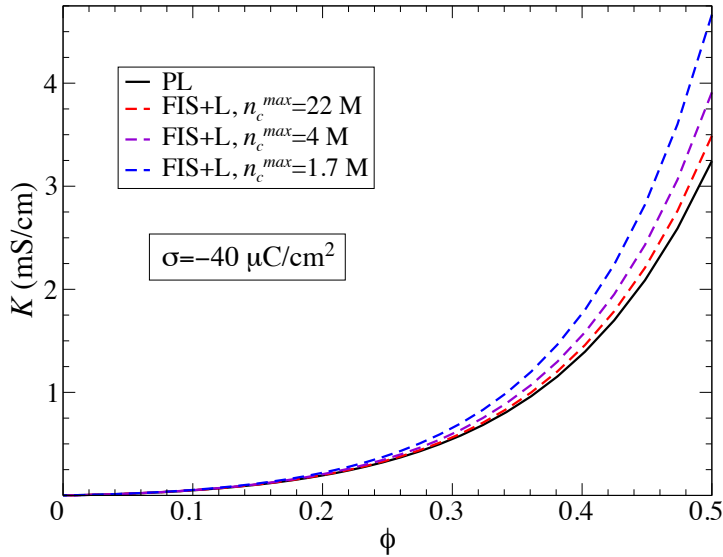
Figure 2.13: Electrical conductivity against particle volume fraction. Dashed lines stand for the results of the FIS+L model for different counterion sizes. Solid black line present the results for point-like counterions.

that region virtually unchanged. There is also a conductivity enhancement with particle volume fraction because the increasing number of the double-layer mobile ions is not offset by the presence of the nonconducting volume occupied by the particles in the unit volume. These behaviors are shown in solid black lines in Figs. 2.12 and 2.13, and in solid colored lines in Fig. 2.14.

When we take into account finite size counterions (FIS+L model, dashed lines in Figs. 2.12, 2.13 and 2.14) we observe similar behaviors but the numerical values of the electrical conductivity are always higher for any counterion size for moderate to high particle charges in concentrated suspensions. If the counterion size approaches to zero, or equivalently $n_c^{max} \to \infty$, the results of the FIS+L model approximate to those of the PL model. Also, for low particle charges and low particle volume fractions the results of both models are almost coincident.

According to Fig. 2.10 the counterions fluxes not in the immediate vicinity of the particle have been enhanced in the FIS+L model in comparison with the PL case. This enhancement gives rise to a larger conductivity of the suspension, because it predominates over the larger PL counterions fluxes
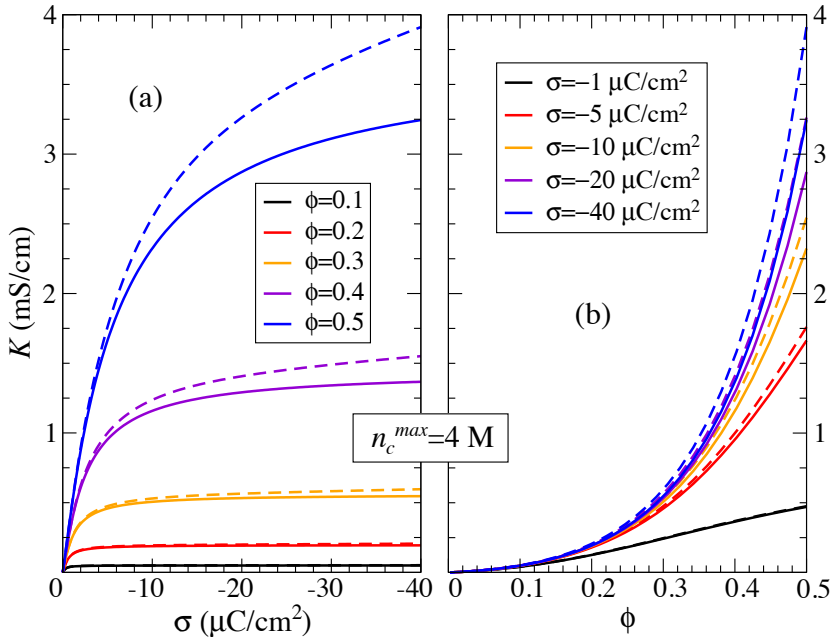
Figure 2.14: (a) Electrical conductivity against the surface charge density for different particle volume fraction values. (b) Electrical conductivity against the particle volume fraction for different surface charge densities. Solid lines show the results for point-like ions. Dashed lines show the results of the FIS+L model.

very close to the particle surface. As these augmented counterions fluxes in the FIS+L model grow with the counterion size, the electric conductivity increases as well (see Figs. 2.12, 2.13 and 2.14).

Although all the conductivity calculations have been performed with H^+ counterions, we have checked that the conductivity behavior shown before maintains for other counterions species with different diffusion coefficients.

2.6   Results: ac electrokinetics

In this section we analyze the changes that appear when we consider finite size counterions in the response of a salt-free concentrated suspension to an oscillating electric field. Once we solve the complete FIS+L model presented in Section 2.1, we calculate the dynamic electrophoretic mobility of the

particles and the relative permittivity of the suspension. The discussion of the results is presented in the following subsections.

2.6.1 Point-like model

The classical frequency response of a salt-free concentrated suspension with point-like counterions, PL model, is as follows: (i) at low frequency, the electromigration and diffusion processes have enough time to be fully developed around the particle and, commonly, this fact leads to the generation of an induced electric dipole moment that tends to brake the particle motion. In this frequency region, there is a plateau value of the dynamic electrophoretic mobility that coincides with the electrophoretic mobility in static electric fields. (ii) As the frequency increases, we find a frequency region where the counterions cannot follow the comparatively fast field oscillations. Thus, the above mentioned dipolar moment decreases and, consequently, the dynamic mobility increases. This process is known as Maxwell-Wagner-O'Konski (MWO) relaxation and takes place whenever the medium and the charged particle, surrounded by its EDL, present different conductivities and permittivities. (iii) Finally, the frequency can be so high that the inertia of the particle and fluid restricts the motion progressively. As a result, the mobility shows a continuous decline when the frequency rises, which is known as the inertial relaxation.

There is another classical relaxation mechanism, the alpha relaxation [7], which is related to the concentration polarization effect (*i.e.*, the presence of a gradient of neutral electrolyte around the particle). We do not find any alpha relaxation in a salt-free suspension, as was explained in Ref. [73], because we only have one ionic species, the added counterions.

In order to clarify the discussion, we will try to separate the different mechanisms by performing three different variations of the PL model:

(i) the complete PL model that includes all the mentioned effects;

(ii) the *pure inertial response* where we do not allow any perturbation of the ionic atmosphere from the equilibrium values. So, breaking mechanisms associated with the charge polarization are excluded in this variation;

(iii) the *inertia-free response*, where we have eliminated all the inertial terms in the electrokinetic equations.

In Fig. 2.15 we show the modulus of the scaled dynamic mobility for the three last-mentioned PL variations. We use two different particle volume fractions at a given particle charge density. We display in solid lines the complete PL model, in dashed lines the *pure inertial response*, and in dotted lines the *inertia-free response*.
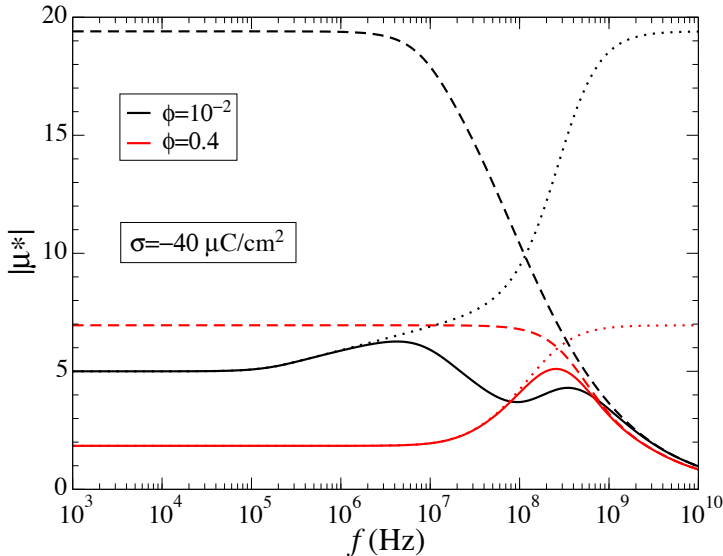
Figure 2.15: Modulus of the scaled dynamic electrophoretic mobility as a function of frequency for different particle volume fractions. We use three variations of the PL model. Solid lines stand for results of the complete PL model. Dashed lines show the *pure inertial response*. Dotted lines display the *inertia-free response*.

The *pure inertial response* behaves as follows: after an initial low frequency mobility plateau, the mobility monotonously decreases with frequency. This plateau has larger values than that of the complete PL model. The difference between the *pure inertial response* and the PL model is due to the absence of breaking effects on particle motion associated with the induced dipole moment (double layer relaxation effect).

In the numerical results corresponding to the *inertia-free response*, we observe one or two successive increments in the dynamic mobility for high or low particle volume fraction, respectively. These increments are related to one or two successive MWO relaxation processes in each case. When we introduce the inertia (dashed lines) to get the complete PL model (solid lines), these above mentioned increments become into one or two successive peaks, as can be observed. The diminution of the dynamic mobility after the first maximum is therefore due to the inertial relaxation.

As was expected, once all the MWO processes have relaxed in the high frequency limit, the mobility in the *inertia-free response* curve reaches the same plateau value than the one of the *pure inertial response* for low frequen-

cies. This is because, when the induced polarization completely disappears, the counterions distribution coincides with that of the equilibrium as in the *pure inertial response.*

2.6.2 Maxwell-Wagner-O'Konski relaxations

We have observed that two differenced MWO relaxations can exist. They will be related to two differenced regions in the EDL. Through the Wagner formula for a constant dielectric mixture, it is possible to obtain the frequency and the dielectric increment of a MWO relaxation [7]

$$\omega_{\text{MWO}} = \frac{(1-\phi)K_p + (2+\phi)K_s}{(1-\phi)\epsilon_0\epsilon_{rp} + (2+\phi)\epsilon_0\epsilon_{rs}} \tag{2.82}$$

$$\Delta\epsilon_{\text{MWO}} = \frac{9\phi(1-\phi)}{(1-\phi)\epsilon_{rp} + (2+\phi)\epsilon_{rs}} \left[\frac{\epsilon_{rs}K_p - \epsilon_{rp}K_s}{(1-\phi)K_p + (2+\phi)K_s} \right]^2 \tag{2.83}$$

where K_p and K_s are the conductivities of the particles and the medium, respectively. The particles are assumed to be made of a nonconducting material. Their conductivity is exclusively associated with the surface conductivity, K^σ, that appears due to an excess of counterions in the ionic atmosphere, $K_p = 2K^\sigma/a$ [8]. Eqs. (2.82) and (2.83) were derived without allowance of mutual polarization of particles and they are valid for suspensions with added electrolyte, thin EDL, and reasonably low ϕ.

The latter equations predict only one MWO relaxation process. However, for suspensions of highly charged particles, two different MWO relaxations have been considered in the literature to explain their dielectric response. This consideration is based on the existence of two differenced regions in the EDL, specially when σ is sufficiently high and ion size effects are considered, see Fig. 2 on Ref. [53]. The first one is a condensate of counterions very close to the particle surface. The second one is a diffuse layer that extends from the end of the condensate to the outer surface of the cell. When we have finite size counterions, the condensate consists in a homogeneous region where counterions are well packaged. In the PL case, such picture of the condensate is not valid, but there are theoretical evidences of the existence of a thin region with different behavior in the electric potential and ionic distribution than in the diffuse layer [64,73]. As was suggested on Ref. [73], we will consider each region with a different associated MWO relaxation process and roughly estimate their MWO relaxation frequencies and dielectric increments to qualitatively explain the behavior of both MWO relaxation processes.

To obtain the relaxation frequency of the condensate, we need to calculate the surface conductivity of the counterion condensation layer. Considering this layer with a mean concentration n_c^{max} and a thickness δ, we obtain

$$K^\sigma = \frac{z_c^2 e^2 n_c^{max} \delta}{\lambda_c} \tag{2.84}$$

For the study of the condensate relaxation, the conductivity of the counterions in the diffuse layer, K_s, will be taken equal to zero, because it has no influence in the condensate relaxation process. Using $K_p = 2K^\sigma/a$ and $\epsilon_{rp} \ll \epsilon_{rs}$, according to Eq. (2.82) we obtain a relaxation frequency

$$\omega_{\text{MWO}}^{cond} = \frac{2z_c^2 e^2 n_c^{max} \delta(1-\phi)}{\epsilon_0 \epsilon_{rs} a \lambda_c (2+\phi)} \tag{2.85}$$

and with Eq. (2.83) a dielectric increment

$$\Delta\epsilon_{\text{MWO}}^{cond} = \frac{9\phi\epsilon_{rs}}{(1-\phi)(2+\phi)} \tag{2.86}$$

To obtain only the relaxation process of the diffuse layer, we need to calculate the conductivity of the counterions in this region, K_s,

$$K_s = \frac{z_c^2 e^2 \overline{n}_c}{\lambda_c} = \frac{-3z_c e \sigma^{dif} \phi}{a\lambda_c(1-\phi)} \tag{2.87}$$

where $\overline{n}_c$ is the average counterions concentration in the diffuse layer, and σ^{dif} is the charge density at the spherical surface, $r = a + \delta$, defined by the thickness of the condensation layer. We now take $K_p = 0$ because we consider the particle with its condensate as an equivalent particle with less surface charge density, σ^{dif}. Introducing the expression of the conductivity K_s in Eq. (2.82) and considering $\epsilon_{rp} \ll \epsilon_{rs}$, we obtain the relaxation frequency of the diffuse layer

$$\omega_{\text{MWO}}^{dif} = \frac{-3z_c e \sigma^{dif} \phi}{\epsilon_0 \epsilon_{rs} a \lambda_c (1-\phi)} \tag{2.88}$$

and with Eq. (2.83) the dielectric increment

$$\Delta\epsilon_{\text{MWO}}^{dif} = \frac{9\phi(1-\phi)\epsilon_{rp}^2}{(2+\phi)^3 \epsilon_{rs}} \tag{2.89}$$

As commented before, the previous expressions will be more precise for reasonably low ϕ. Also, the expression for the MWO relaxation frequency of the condensate will be more accurate than the one for the diffuse layer: the use of an average concentration works better in the condensate because it is a thin layer with homogeneous ionic density.
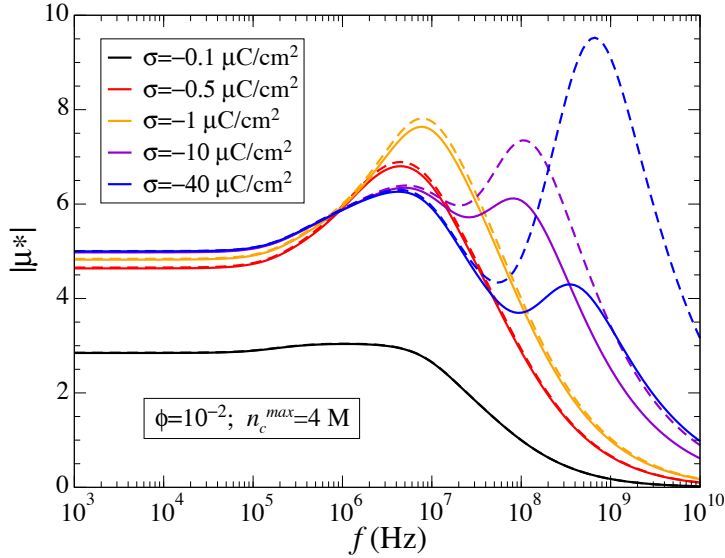
Figure 2.16: Modulus of the scaled dynamic electrophoretic mobility of the particles as a function of frequency for different particle surface charge densities. All calculations performed at low particle volume fraction. Solid lines show the results for point-like ions. Dashed lines show the results of the FIS+L model with $n_c^{max} = 4$ M.

2.6.3 Finite ion size

We will jointly study both the dynamic electrophoretic mobility of the particles and the dielectric response of the suspension as a function of frequency, because they are strongly interrelated.

Condensate MWO relaxation

Fig. 2.16 represents the modulus of the scaled dynamic electrophoretic mobility and Fig. 2.17 the real (a) and the imaginary (b) parts of the relative permittivity of a salt-free concentrated suspension as a function of frequency. We compare the results of the FIS+L model (dashed lines) at a fixed counterion size, $n_c^{max} = 4$ M, with those of the PL model (solid lines). Different colors stand for different particle surface charges. The calculations were made at low particle volume fraction, $\phi = 10^{-2}$.

For the low frequency mobility and permittivity plateaus, Figs. 2.16 and 2.17a, we observe that there is almost no difference between the finite size
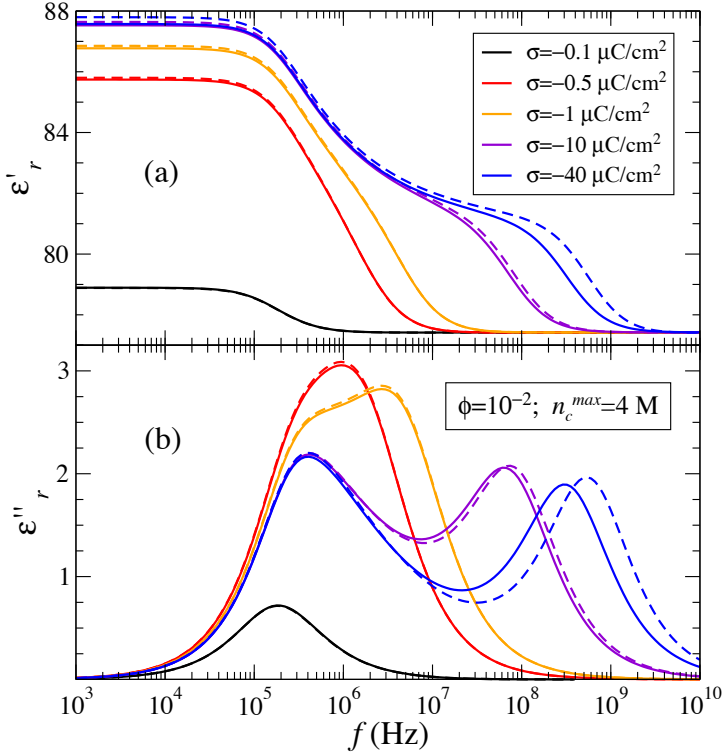
Figure 2.17: Real (a) and imaginary (b) parts of the relative permittivity of the suspension as a function of frequency for different particle surface charge densities. All calculations performed at low particle volume fraction. Solid lines show the results for point-like ions. Dashed lines show the results of the FIS+L model with $n_c^{max} = 4$ M.

and point-like results for any particle charge at low particle volume fraction. As was discussed in Ref. [14] and Section 2.5 for the static mobility and conductivity, this is because in the case of a dilute suspension the inclusion of ion size effects only significantly modifies the counterions fluxes in the immediate vicinity of the particle.

The MWO relaxation frequency is defined as that of the maximum in the imaginary part of the permittivity, as it is well-known. We note that for a suspension with low volume fraction, depending on particle surface charge, one or two differenced MWO relaxations, Fig. 2.17, or analogously one or two mobility maximums, Fig. 2.16, may take place. As we indicated before, we associate the first one upon increasing frequency with the MWO

relaxation of the diffuse part of the EDL, and the second one with the relaxation of the condensate.

At low σ there is no condensate of counterions near the particle surface and therefore no condensate MWO relaxation process is observed. When we rise the particle charge, almost all the extra counterions accumulate in the condensate [64, 109], which significantly grows when also ion size effects are considered [53]. This explains why ion size effects do not produce any remarkable effect in the MWO relaxation of the diffuse part of the EDL and why they considerably enhance the condensate MWO relaxation.

According to Eq. (2.88), the frequency of the MWO of the diffuse layer changes with σ^{dif}. As the counterions concentration in the diffuse layer has been scarcely altered, ω_{MWO}^{dif} remains basically the same in Figs. 2.16 and 2.17. On the contrary, Fig. 2.17b shows an increment of the frequency of the condensate MWO relaxation when ion size effects are considered. This is in agreement with Eq. (2.85), because ω_{MWO}^{cond} increases when the width of the condensate, δ, raises. For the well resolved MWO peaks of the two highest surface charge curves in Fig. 2.17b, we observe that the height of the peaks is nearly independent on both, the surface charge density and the ion size, in accordance with Eqs. (2.86) and (2.89).

In Section 2.5, we studied the effects of the electric polarization on the magnitude of the static electrophoretic mobility in a salt-free concentrated suspension with finite ion size effects. This study was based on a procedure developed by Bradshaw-Hajek *et al.* [110]. We showed that the induced charge polarization density was larger when ion size effects were considered. The generalization of the latter study to ac electric fields leads to similar conclusions. As the relaxation effect and, correspondingly, the induced dipole moment, have been increased with ion size, the second mobility maximum in Fig. 2.16 attains higher values as well. This is due to the disappearance of breaking mechanisms on the particle motion of increasing importance as the ion size grows, causing the dynamic mobility to reach superior values when the size of the counterions is taken into account.

Overlapping of MWO relaxations

We show the frequency response of the modulus of the scaled dynamic electrophoretic mobility and the imaginary part of the relative permittivity of the suspension in Figs. 2.18 and 2.19, respectively. In both Figures we compare the results of the FIS+L model with $n_c^{max} = 4$ M, dashed lines, with those of the PL model, solid lines, for different particle volume fractions. All the calculations were performed at a high particle charge, $\sigma = -40 \ \mu\text{C/cm}^2$.
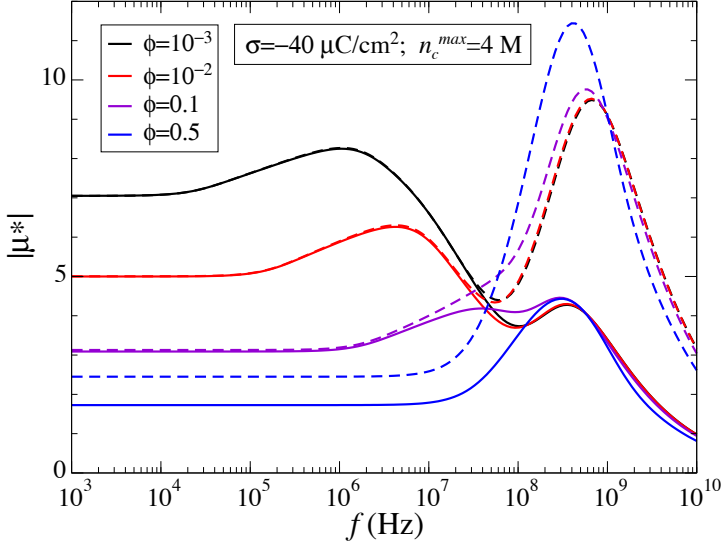
Figure 2.18: Modulus of the scaled dynamic electrophoretic mobility of the particles as a function of frequency for different particle volume fractions. Solid lines show the results for point-like ions. Dashed lines show the results of the FIS+L model with $n_c^{max} = 4$ M.

We see in Figs. 2.16 and 2.17 how two differenced MWO relaxations take place when surface charge increases in conditions of low volume fraction. Now we observe that the MWO relaxations of the condensate and the diffuse layer in Fig. 2.19, or analogously the two mobility maximums in Fig. 2.18, tend to overlap in frequency for concentrated suspensions at high surface charge. According to Eq. (2.88), $\omega_{\mathrm{MWO}}^{dif}$ grows with volume fraction at a rate $\phi/(1 - \phi)$. This is in agreement with the frequency shift observed in the MWO relaxation of the diffuse layer, indicated with black arrows in Fig. 2.19. Eq. (2.85) predicts a frequency change with volume fraction at a rate $(1 - \phi)/(2 + \phi)$ for the condensate MWO relaxation. Then we find no significant changes in $\omega_{\mathrm{MWO}}^{cond}$ for low ϕ values, and a small decrease for high volume fractions as shown in Fig. 2.19. These behaviors result in the observed overlapping of the MWO relaxations for concentrated suspensions.

When we include ion size effects we find only changes in the condensate MWO relaxation (enhancement of the corresponding mobility maximum and small increase in $\omega_{\mathrm{MWO}}^{cond}$). These changes can be explained with the same reasoning used for Figs. 2.16 and 2.17: the consideration of finite size counterions significantly enlarges the condensate near the particle but does
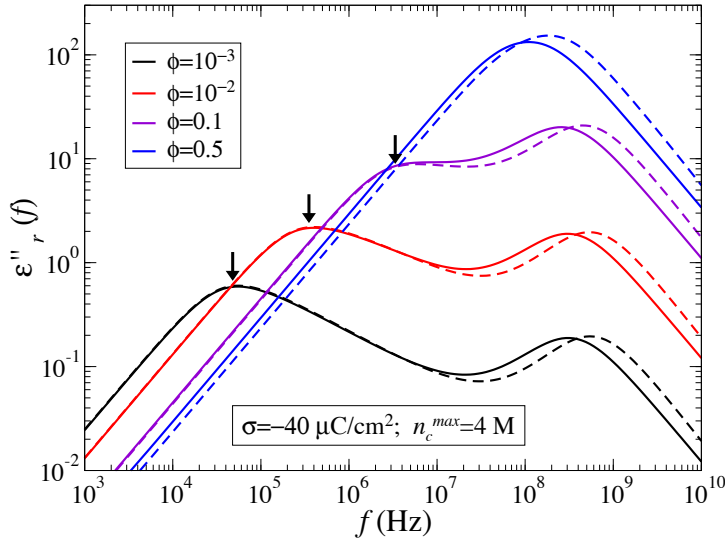
Figure 2.19: Imaginary part of the relative permittivity of the suspension as a function of frequency for different particle volume fractions. Solid lines show the results for point-like ions. Dashed lines show the results of the FIS+L model with $n_c^{max} = 4$ M.

not produce remarkable effects in the diffuse layer. We also observe the well-known diminution of mobility with the increase of volume fraction in Fig. 2.18 due basically to the larger screening of the particle charge [53]: when the particle concentration grows, the available space for the counterions inside the cell decreases and, consequently, the screening of the particle charge is greatly raised, thus reducing the value of the surface potential and, therefore, the mobility.

Highly charged concentrated suspensions

Figs. 2.20 and 2.21 show the modulus of the scaled dynamic electrophoretic mobility and the real (a) and imaginary (b) parts of the relative permittivity of the suspension as a function of frequency for different particle surface charges. We compare the results of the FIS+L model with $n_c^{max} = 4$ M, dashed lines, with those of the PL model, solid lines at a high particle volume fraction, $\phi = 0.5$.

Besides, Figs. 2.22 and 2.23 represent the same quantities at fixed particle surface charge, $\sigma = -40$ μC/cm^2, and volume fraction, $\phi = 0.5$. In these
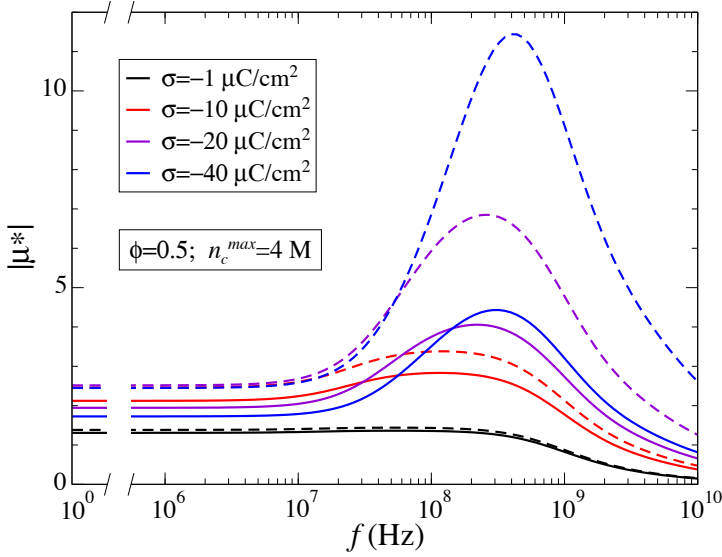
Figure 2.20: Modulus of the scaled dynamic electrophoretic mobility of the particles as a function of frequency for different particle surface charge densities. All calculations performed at high particle volume fraction. Solid lines show the results for point-like ions. Dashed lines show the results of the FIS+L model with $n_c^{max} = 4$ M.

Figures, we compare the results of the FIS+L model at different ion sizes (different colored dashed lines) with those of the PL model (black lines).

As we mentioned before, for this high volume fraction value, the two MWO relaxations are overlapped in a unique broad peak. We observe how both the dynamic mobility and relative permittivity increase when we consider finite size counterions in comparison with the PL case and when we increase the particle surface charge. The reason is that the increase of the surface charge or the consideration of ion size effects leads to an enhancement of the overall charge polarization in the EDL, resulting in both, higher permittivity values as can be seen in Figs. 2.21a and 2.23a, and larger heights of the corresponding peaks of the imaginary part, Figs. 2.21b and 2.23b. A similar explanation applies to the remarkable increment observed in the mobility maxima, associated with the MWO relaxations, Figs. 2.20 and 2.22: the disappearance of the augmented induced dipole moment gives rise to greater mobility values.

Figs. 2.21b and 2.23b display a shift to larger frequencies in the MWO relaxation when ion size effects are considered. This shift is also larger the
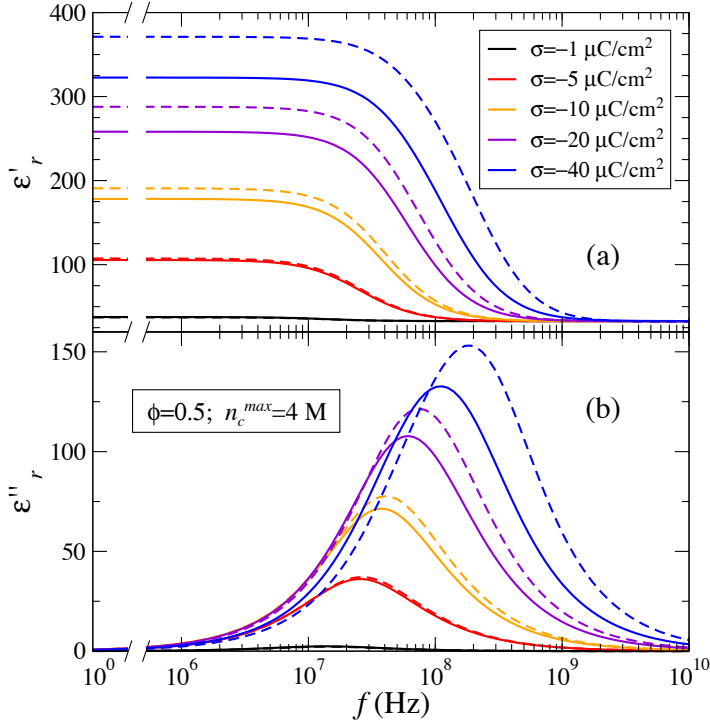
Figure 2.21: Real (a) and imaginary (b) parts of the relative permittivity of the suspension as a function of frequency for different particle surface charge densities. All calculations performed at high particle volume fraction. Solid lines show the results for point-like ions. Dashed lines show the results of the FIS+L model with $n_c^{max} = 4$ M.

larger the size of the counterions (lower n_c^{max} value). The MWO relaxation of the diffuse layer is nearly independent of the ion size, Eq. (2.88), and, therefore, the shift observed is entirely due to the displacement of the condensate MWO relaxation. We have checked numerically that the expression of the MWO relaxation frequency of the condensate, Eq. (2.85), predicts a shift to higher frequencies with the increase of the ion size through the product $n_c^{max}\delta$. This is because the width of the condensate δ augments in a higher rate than the parameter n_c^{max} diminishes upon increasing ion size [53]. When we increase the particle surface charge, we are also increasing the surface conductivity K^σ of the condensate, for both PL and FIS+L models, and consequently the frequency of the MWO relaxation rises.

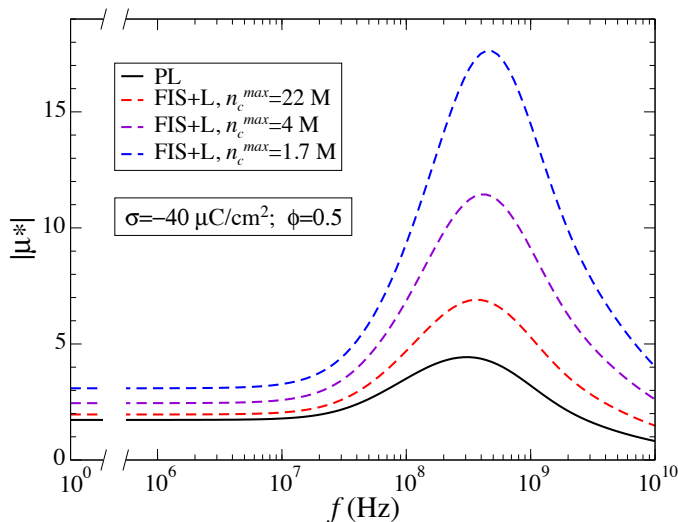Figure 2.22: Modulus of the scaled dynamic electrophoretic mobility of the particles as a function of frequency for different ion sizes (dashed lines). Black lines show the results for point like ions.
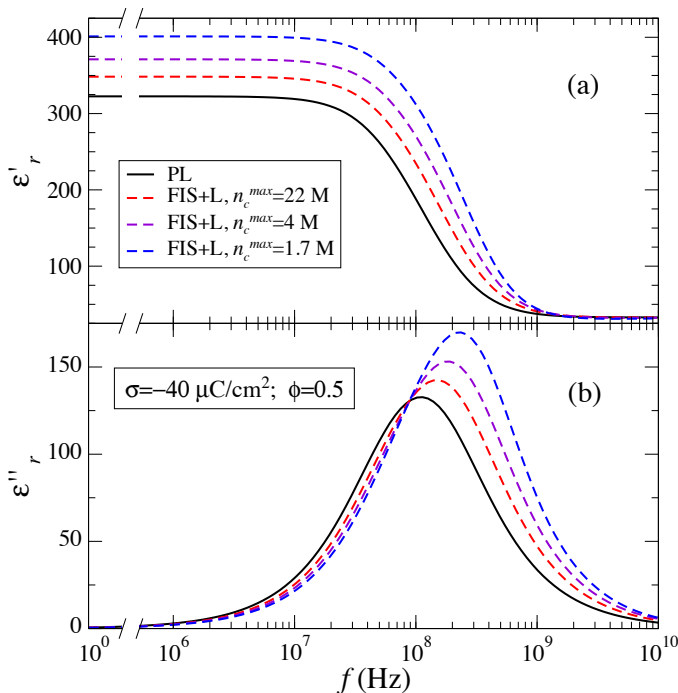

Figure 2.23: Real (a) and imaginary (b) parts of the relative permittivity of the suspension as a function of frequency for different ion sizes (dashed lines). Black lines show the results for point like ions.

Chapter 3

Realistic salt-free suspensions

In this chapter, we deal with realistic salt-free concentrated suspensions including ion size effects to get closer to experimental conditions. Our systems consist of aqueous suspensions deionized maximally without any electrolyte added during the preparation. Hence, in addition to the added counterions released by the particles to the solution, we must also consider the H^+ and OH^- ions from water dissociation. Moreover, if the suspension is open to the atmosphere, there will be other ions produced by the atmospheric CO_2 contamination. All these new ionic species could be coincident, or not, with that of the added counterions. We analyze the influence of the finite ion size in the equilibrium EDL of realistic salt-free suspensions by comparing our results with those from Chapter 2 and with point-like calculations. We also show some preliminary experimental results to test the validity of the models discussed before.

3.1   Model

We generalize the model presented in Section 2.1 for the equilibrium EDL in ideal salt-free concentrated suspensions to the general case of N ionic species in the suspension. Of course the ionic species dissolved in the liquid medium that appeared by water dissociation and atmospheric CO_2 contamination will be coupled by appropriate chemical equilibrium mass-action equations. The details for each particular situation can be found in Subsection 3.1.1.

Let us consider a spherical charged particle of radius a and surface charge density σ immersed in a realistic salt-free medium with N ionic species in-

cluding that of the added counterions that counterbalance its surface charge. In our description, the axes of the spherical coordinate system (r, θ, φ) are fixed at the center of the particle. In the absence of any external field, the particle is surrounded by a spherically symmetrical charge distribution. Within a mean-field approximation, the total free energy of the system, $F = U - TS$, can be written in terms of the equilibrium electric potential $\Psi^0(\mathbf{r})$ and the equilibrium ionic concentration $n_i^0(\mathbf{r})$ of the different ionic species, $i = 1, \ldots, N$, of the suspension. The configurational internal energy contribution U is

$$U = \int d\mathbf{r} \left[-\frac{\epsilon_0 \epsilon_{rs}}{2} |\nabla \Psi^0(\mathbf{r})|^2 + \sum_{i=1}^{N} z_i e n_i^0(\mathbf{r}) \Psi^0(\mathbf{r}) - \sum_{i=1}^{N} \mu_i^0 n_i^0(\mathbf{r}) \right] \quad (3.1)$$

The first term is the self-energy of the electric field, where again ϵ_0 is the vacuum permittivity, and ϵ_{rs} is the relative permittivity of the suspending medium. The next term is the sum of the electrostatic energies of the different ionic species in the electrostatic mean field, and the last term couples the system to a bulk reservoir, where μ_i^0 is the equilibrium chemical potential of the ionic species i.

The entropic contribution $-TS$ is

$$-TS = k_B T n^{max} \int d\mathbf{r} \left[\sum_{i=1}^{N} \frac{n_i^0(\mathbf{r})}{n^{max}} \ln \left(\frac{n_i^0(\mathbf{r})}{n^{max}} \right) \right.$$
$$\left. + \left(1 - \sum_{i=1}^{N} \frac{n_i^0(\mathbf{r})}{n^{max}} \right) \ln \left(1 - \sum_{i=1}^{N} \frac{n_i^0(\mathbf{r})}{n^{max}} \right) \right] \quad (3.2)$$

where k_B is Boltzmann's constant, T is the absolute temperature, and n^{max} is the maximum possible ionic concentration due to the excluded volume effect, defined as $n^{max} = V^{-1}$, where V is the average volume occupied by an ion in the solution. For simplicity, we assume that all types of ions have the same size, and therefore n^{max} will take the same value for all of them. The first term inside the integral is the sum of the entropy of the different ionic species, and the second one is the entropy of the solvent molecules. This last term accounts for the ion size effect that modifies the classical Poisson-Boltzmann equation and was proposed earlier by Borukhov *et al.* [38]

The variation of the free energy $F = U - TS$ with respect to $\Psi^0(\mathbf{r})$

provides the Poisson equation

$$\nabla^2 \Psi^0(\mathbf{r}) = -\frac{e}{\epsilon_0 \epsilon_{rs}} \sum_{i=1}^{N} z_i n_i^0(\mathbf{r}) \tag{3.3}$$

and the ionic concentration of the ionic species i is obtained by performing the variation of the free energy with respect to $n_i^0(\mathbf{r})$, yielding

$$n_i^0(\mathbf{r}) = \frac{b_i \exp\left(-\frac{z_i e \Psi^0(\mathbf{r})}{k_B T}\right)}{1 + \sum_{j=1}^{N} \frac{b_j}{n^{max}} \left[\exp\left(-\frac{z_j e \Psi^0(\mathbf{r})}{k_B T}\right) - 1\right]} \tag{3.4}$$

where b_i is an unknown coefficient that represents the ionic concentration of the species i where the electric potential is zero.

Applying the spherical symmetry of the problem and combining Eqs. 3.3 and 3.4, we obtain a modified Poisson-Boltzmann equation for the equilibrium electric potential considering N ionic species

$$\frac{\mathrm{d}^2 \Psi^0(r)}{\mathrm{d}r^2} + \frac{2}{r} \frac{\mathrm{d}\Psi^0(r)}{\mathrm{d}r} = -\frac{e}{\epsilon_0 \epsilon_{rs}} \frac{\sum_{i=1}^{N} z_i b_i \exp\left(-\frac{z_i e \Psi^0(r)}{k_B T}\right)}{1 + \sum_{i=1}^{N} \frac{b_i}{n^{max}} \left[\exp\left(-\frac{z_i e \Psi^0(r)}{k_B T}\right) - 1\right]} \tag{3.5}$$

We need two boundary conditions to solve the modified Poisson-Boltzmann equation. The first one is

$$\left.\frac{\mathrm{d}\Psi^0(r)}{\mathrm{d}r}\right|_{r=b} = 0 \tag{3.6}$$

which derives from the electroneutrality condition of the cell and the application of Gauss' theorem to the outer surface of the cell. The second one is

$$\Psi^0(b) = 0 \tag{3.7}$$

that fixes the origin of the electric potential at $r = b$.

The equilibrium problem, Eqs. 3.5, 3.6, and 3.7, can be solved iteratively using the electroneutrality condition of the cell and appropriate chemical reactions to find the unknown b_i coefficients (see Subsection 3.1.1 for details

on b_i calculation). This kind of problem can be solved in a better way by using dimensionless variables [70], which are defined as

$$x = \frac{r}{a} \qquad \tilde{\Psi}^0(x) = \frac{e\Psi^0(r)}{k_B T} \qquad \tilde{\sigma} = \frac{ea}{\epsilon_0\epsilon_{rs}k_B T}\sigma$$

$$\tilde{b}_i = \frac{e^2 a^2}{\epsilon_0\epsilon_{rs}k_B T}b_i \qquad \tilde{n}^{max} = \frac{e^2 a^2}{\epsilon_0\epsilon_{rs}k_B T}n^{max} \qquad (3.8)$$

and rewriting Eq. 3.5 as

$$g(x) \equiv \frac{d^2\tilde{\Psi}^0(x)}{dx^2} + \frac{2}{x}\frac{d\tilde{\Psi}^0(x)}{dx} = \frac{-\displaystyle\sum_{i=1}^{N} z_i\tilde{b}_i e^{-z_i\tilde{\Psi}^0(x)}}{1 + \displaystyle\sum_{i=1}^{N} \frac{\tilde{b}_i}{\tilde{n}^{max}}\left(e^{-z_i\tilde{\Psi}^0(x)} - 1\right)} \qquad (3.9)$$

where we have defined the function $g(x)$. If we differentiate it, after a little algebra, we find that

$$g'(x) + \frac{\displaystyle\sum_{i=1}^{N} z_i^2\tilde{b}_i e^{-z_i\tilde{\Psi}^0(x)}}{\displaystyle\sum_{i=1}^{N} z_i\tilde{b}_i e^{-z_i\tilde{\Psi}^0(x)}} g(x)\tilde{\Psi}^{0\prime}(x) + \frac{1}{\tilde{n}^{max}}g^2(x)\tilde{\Psi}^{0\prime}(x) = 0 \qquad (3.10)$$

where the prime stands for differentiation with respect to x. In terms of the electric potential, Eq. 3.10 is rewritten as

$$\tilde{\Psi}^{0\prime\prime\prime}(x) + \frac{2}{x}\tilde{\Psi}^{0\prime\prime}(x) - \frac{2}{x^2}\tilde{\Psi}^{0\prime}(x) + \tilde{\Psi}^{\prime 0}(x)\left(\tilde{\Psi}^{0\prime\prime}(x) + \frac{2}{x}\tilde{\Psi}^{0\prime}(x)\right)$$

$$\times \left[\frac{\displaystyle\sum_{i=1}^{N} z_i^2\tilde{b}_i e^{-z_i\tilde{\Psi}^0(x)}}{\displaystyle\sum_{i=1}^{N} z_i\tilde{b}_i e^{-z_i\tilde{\Psi}^0(x)}} + \frac{1}{\tilde{n}^{max}}\left(\tilde{\Psi}^{0\prime\prime}(x) + \frac{2}{x}\tilde{\Psi}^{0\prime}(x)\right)\right] = 0 \quad (3.11)$$

Eq. 3.11 is a nonlinear third-order differential equation that needs three boundary conditions to completely specify the solution. Two of them are provided by Eqs. 3.6 and 3.7, which now read

$$\tilde{\Psi}^{0\prime}(h) = 0; \quad \tilde{\Psi}^0(h) = 0 \qquad (3.12)$$

where $h = (b/a) = \phi^{-1/3}$ is the dimensionless outer radius of the cell. The third one specifies the electrical state of the particle, and can be obtained by applying Gauss theorem to the outer side of the particle surface $r = a$

$$\left.\frac{\mathrm{d}\Psi^0(r)}{\mathrm{d}r}\right|_{r=a} = -\frac{\sigma}{\epsilon_0 \epsilon_{rs}} \tag{3.13}$$

Its dimensionless form is

$$\tilde{\Psi}^{0'}(1) = -\tilde{\sigma} \tag{3.14}$$

Many theoretical and experimental studies have recently explored the use of either constant surface potential or constant surface charge boundary conditions. These conditions, although making the mathematical treatment simpler, represent only limiting or idealized cases. Many biological and artificial particles have their surface charge associated with some degree of dissociation of functional groups which depend on the nearby environment. Constant surface potential and constant surface charge models would correspond, respectively, to the cases when the dissociation reactions of the functional groups are infinitely fast and infinitely slow [111]. Also, some authors have derived an hybrid surface charge model to account for the electrical state of the particles [112], which is a generalization of the conventional constant surface potential and constant surface-charged density models. Our model can be modified to include charge regulation mechanisms at the particle surface.

It is very common in the literature to use the surface charge or the surface potential as a boundary condition at the particle surface when solving the equilibrium Poisson-Boltzmann equation, and both of them are valid. When it comes to concentrated suspensions, we prefer to use the particle surface charge as a boundary condition because in many cases of interest the particle charge is a property that can be determined experimentally. Moreover, the use of commercially available latex suspensions with fully dissociated surface electrical groups, have led us to choose the constant surface charge boundary condition. Besides, the surface potential depends on the choice of the potential origin, and in the case of concentrated suspensions there is not a standard criterium for this choice. As stated in Eq. 3.7 we have chosen it at the outer surface of the cell, $r = b$.

If we consider point-like ions, $n^{max} = \infty$, Eq. 3.11 generates the expressions obtained by Ruiz-Reina and Carrique [70] for realistic salt-free suspensions. Also, if we evaluate Eq. 3.11 considering that we have just one

ionic species, the added counterions that counterbalance the particle sur-
face charge, the equation reduces to Eq. 2.18 for ideal salt-free suspensions
including ion size effects.

Following the work of Aranda-Rascón *et al.* [11], we incorporate a dis-
tance of closest approach of the ions to the particle surface, resulting from
their finite size. As we said before, for the sake of simplicity we have con-
sidered that all ions have the same size. We assume that ions cannot come
closer to the surface of the particle than the chosen effective hydration ionic
radius, R, and, therefore, the ionic concentration will be zero in the region
between the particle surface, $r = a$, and the spherical surface, $r = a + R$,
defined by the ionic effective radius.

The whole electric potential $\Psi^0(r)$ is now determined by combining
Laplace's and the modified Poisson-Boltzmann equations into the follow-
ing stepwise equation

$$\begin{cases} \dfrac{d^2\Psi^0(r)}{dr^2} + \dfrac{2}{r}\dfrac{d\Psi^0(r)}{dr} = 0 & a \leq r \leq a + R \\[2em] \text{Eq. 3.5} & a + R \leq r \leq b \end{cases} \qquad (3.15)$$

We must impose the continuity of the potential and of its first derivative
at the surface $r = a + R$, in addition to boundary conditions, Eqs. 3.6 and
3.7. The continuity of the first derivative comes from the continuity of the
normal component of the electric displacement at that surface.

As we have seen before, changing the system of second order differential
equations, Eq. 3.15, into one of third order, hugely simplify the resolution
process

$$\begin{cases} \tilde{\Psi}^{0\prime\prime\prime}(x) + \dfrac{2}{x}\tilde{\Psi}^{0\prime\prime}(x) - \dfrac{2}{x^2}\tilde{\Psi}^{0\prime}(x) = 0 & 1 \leq x \leq 1 + \xi \\[2em] \text{Eq. 3.11} & 1 + \xi \leq x \leq h \end{cases} \qquad (3.16)$$

where $\xi = R/a$ and having used dimensionless variables. The boundary
conditions needed to completely close the problem are

$$\tilde{\Psi}^{0\prime}{}_L(1) = -\tilde{\sigma} \qquad \tilde{\Psi}^{0\prime}{}_L(1+\xi) = \frac{-\tilde{\sigma}}{(1+\xi)^2}$$

$$\tilde{\Psi}^0{}_P(h) = 0 \qquad \tilde{\Psi}^{0\prime}{}_P(h) = 0$$

$$\tilde{\Psi}^0{}_L(1+\xi) = \tilde{\Psi}^0{}_P(1+\xi) \qquad \tilde{\Psi}^{0\prime}{}_L(1+\xi) = \tilde{\Psi}^{0\prime}{}_P(1+\xi) \qquad (3.17)$$

where subscript L refers to the region in which the potential is calculated using Laplace's equation, and subscript P refers to the region in which we evaluate the modified Poisson-Boltzmann equation.

The complete equilibrium electric potential $\tilde{\Psi}^0(x)$ is obtained numerically using Eqs. 3.16 and 3.17, including an iterative process for the calculation of the b_i coefficients. Once the electric potential is found, the equilibrium ionic concentrations $n_i^0(r)$ for the different ionic species can be derived (see subsection 3.1.1 for details).

3.1.1 Particularization for different realistic salt-free suspensions

In this Subsection we give details of the calculation of the different b_i coefficients for realistic salt-free suspensions when we have, besides the added counterions, water dissociation and atmospheric contamination ions. We separate the cases in which the added counterions are coincident or not with any of the other ionic species.

Added counterions and water dissociation

Let us consider that, in addition to the added counterions stemming from the particle charging process, there are also H^+ and OH^- ions coming from water dissociation in the liquid medium. This will always occur in aqueous suspensions. The equilibrium mass-action equation for water dissociation, which we assume to hold at the outer surface of the cell, is

$$[H^+][OH^-] = K_w \quad \Rightarrow \quad \tilde{b}_{H^+}\tilde{b}_{OH^-} = \tilde{K}_w \tag{3.18}$$

where the square brackets stand for the molar concentration, $K_w = 10^{-14}$ mol^2/L^2 is the water dissociation constant at room temperature, 298.15 K, and $\tilde{K}_w$ is a dimensionless quantity defined by

$$\tilde{K}_w = \left(\frac{10^3 N_A e^2 a^2}{\epsilon_0 \epsilon_{rs} k_B T} \right)^2 K_w \tag{3.19}$$

with N_A the Avogadro constant.

We can distinguish between two cases, (a) when the added counterions are H^+ or OH^- ions, and (b) when they are of a different ionic species. The distinction is important because in the (a) case, the added counterions will enter in the equilibrium reaction equation for water dissociation, whereas in the (b) case, they do not.

Case a. In this case we have two different ionic species. Evaluating Eq. 3.9, particularized just for H^+ and OH^- ions, at $x = h$ we obtain

$$\tilde{\Psi}^{0\prime\prime}(h) = -z_{H^+}\tilde{b}_{H^+} - z_{OH^-}\tilde{b}_{OH^-} \tag{3.20}$$

Using the relation between both $\tilde{b}_{H^+}$ and $\tilde{b}_{OH^-}$ coefficients given by Eq. 3.18, we can write Eqs. 3.16 and 3.20 in terms of just one unknown coefficient, $\tilde{b}_{H^+}$. The iterative process needed for the numerical resolution of the third order version of the modified Poisson-Boltzmann problem remains as follows. We choose an initial guess for the $\tilde{b}_{H^+}$ coefficient, say $\tilde{b}_{H^+}^{(0)} = 0$ or, in a more accurate way, the value obtained for point-like ions, and solve Eq. 3.16 with the boundary conditions given by Eq. 3.17. We obtain the solution $\tilde{\Psi}^{0(0)}(x)$, and then, we use Eq. 3.18 and 3.20 to find a new value $\tilde{b}_{H^+}^{(1)}$, which will give us $\tilde{\Psi}^{0(1)}(x)$ using Eqs. 3.16 and 3.17 again. The numerical iterative process is repeated until the relative variation of the electric potential at the particle surface is lower than a prescribed quantity. Although an iterative process has been used to obtain the solution to Eq. 3.16 with boundary conditions, Eq. 3.17, and Eqs. 3.18 and 3.20, this procedure is much better than the original and equivalent iterative problem defined by Eq. 3.15. The improved convergency and superior numerical efficiency that are obtained when computing the third order problem lie in the facts that all of the intermediate solutions $\tilde{\Psi}^{0(n)}(x)$ of the iterative method have the correct slope $\tilde{\Psi}^{0\prime}(1) = -\tilde{\sigma}$ at the particle surface. This is not true if we use the original scheme because in that case the slope at the particle surface is not determined by any condition.

Case b. In this case we have three different ionic species. Evaluating Eq. 3.9, particularized for the added counterions, of valency z_c, and the ions H^+ and OH^-, at $x = h$ we obtain

$$\tilde{\Psi}^{0\prime\prime}(h) = -z_c\tilde{b}_c - z_{H^+}\tilde{b}_{H^+} - z_{OH^-}\tilde{b}_{OH^-} \tag{3.21}$$

The added counterions counterbalance the overall charge on the particle surface

$$\tilde{\sigma} = -\int_1^h \frac{z_c\tilde{b}_c e^{-z_c\tilde{\Psi}^0(x)}}{1 + \sum\limits_{i=1}^{N} \dfrac{\tilde{b}_i}{\tilde{n}^{max}}\left(e^{-z_i\tilde{\Psi}^0(x)} - 1\right)} x^2 dx \tag{3.22}$$

whereas the number of H^+ and OH^- must be equal due to the electroneutrality of the cell.

Using the relation between both $\tilde{b}_{\mathrm{H+}}$ and $\tilde{b}_{\mathrm{OH-}}$ coefficients given by Eq. 3.18, we can write Eqs. 3.16, 3.21, and 3.22 in terms of two unknown coefficients, $\tilde{b}_c$ and $\tilde{b}_{\mathrm{H+}}$. The iterative process to obtain the solution to Eq. 3.16 with boundary conditions, Eq. 3.17, and Eqs. 3.18, 3.21, and 3.22, is similar to the one described before, but in this case we have the two unknown coefficients, $\tilde{b}_c$ and $\tilde{b}_{\mathrm{H+}}$, to be determined iteratively.

Added counterions, water dissociation, and atmospheric contamination

Let us consider now that, in addition to the added counterions and the $\mathrm{H^+}$ and $\mathrm{OH^-}$ ions coming from water dissociation, there are also present ions stemming from the atmospheric CO_2 contamination in the liquid medium. This will always occur in aqueous suspensions in contact with the atmosphere; the CO_2 gas diffused into the suspension combines with water molecules to form carbonic acid H_2CO_3, and then, the following dissociation reactions take place

$$\mathrm{H_2CO_3} \rightleftarrows \mathrm{H^+} + \mathrm{HCO_3^-} \tag{3.23}$$
$$\mathrm{HCO_3^-} \rightleftarrows \mathrm{H^+} + \mathrm{CO_3^=} \tag{3.24}$$

with equilibrium dissociation constants $K_1 = 4.47 \cdot 10^{-7}$ mol/L and $K_2 = 4.67 \cdot 10^{-11}$ mol/L at room temperature, 298.15 K, respectively. The concentration of H_2CO_3 molecules in water can be calculated from the solubility and the partial pressure of CO_2 in standard air. For a temperature of 298.15 K and an atmospheric pressure of 101300 Pa, the concentration of carbonic acid is approximately $[\mathrm{H_2CO_3}] = 1.08 \cdot 10^{-5}$ mol/L, depending its particular value on the local environmental conditions. The dimensionless dissociation constants and H_2CO_3 concentration are

$$\tilde{K}_1 = \frac{10^3 N_A e^2 a^2}{\epsilon_0 \epsilon_{rs} k_B T} K_1; \quad \tilde{K}_2 = \frac{10^3 N_A e^2 a^2}{\epsilon_0 \epsilon_{rs} k_B T} K_2$$
$$\tilde{N}_{\mathrm{H_2CO_3}} = \frac{10^3 N_A e^2 a^2}{\epsilon_0 \epsilon_{rs} k_B T} N_{\mathrm{H_2CO_3}} \tag{3.25}$$

where all the values are taken in S.I. units. The equilibrium mass-action equations, which we assume to hold at the outer surface of the cell, are

$$\frac{[\mathrm{H^+}][\mathrm{HCO_3^-}]}{[\mathrm{H_2CO_3}]} = K_1 \quad \Rightarrow \quad \frac{\tilde{b}_{\mathrm{H^+}}\tilde{b}_{\mathrm{HCO_3^-}}}{\tilde{N}_{\mathrm{H_2CO_3}}} = \tilde{K}_1 \qquad (3.26)$$

$$\frac{[\mathrm{H^+}][\mathrm{CO_3^=}]}{[\mathrm{HCO_3^-}]} = K_2 \quad \Rightarrow \quad \frac{\tilde{b}_{\mathrm{H^+}}\tilde{b}_{\mathrm{CO_3^=}}}{\tilde{b}_{\mathrm{HCO_3^-}}} = \tilde{K}_2 \qquad (3.27)$$

Hereafter, the second dissociation reaction, Eq. 3.24, will be neglected because the terms associated to the ion $\mathrm{CO_3^=}$ that appears in Eq. 3.16 are several orders of magnitude lower than those due to the ion $\mathrm{HCO_3^-}$, in accordance with what Ruiz-Reina and Carrique showed in a previous work [70].

Once more, we can distinguish between two cases, (a) when the added counterions are coincident with one of the ionic species in the system ($\mathrm{H^+}$, $\mathrm{OH^-}$ or $\mathrm{HCO_3^-}$) and (b) when they are of a different ionic species. In the (a) case, the added counterions will enter in one of the equilibrium dissociation equations, whereas in the (b) case, they do not.

Case a.   In this case we have three different ionic species. Evaluating Eq. 3.9, particularized for $\mathrm{H^+}$, $\mathrm{OH^-}$ and $\mathrm{HCO_3^-}$ ions, at $x = h$ we obtain

$$\tilde{\Psi}^{0''}(h) = -z_{\mathrm{H^+}}\tilde{b}_{\mathrm{H^+}} - z_{\mathrm{OH^-}}\tilde{b}_{\mathrm{OH^-}} - z_{\mathrm{HCO_3^-}}\tilde{b}_{\mathrm{HCO_3^-}} \qquad (3.28)$$

Using the relations between coefficients $\tilde{b}_{\mathrm{H^+}}$, $\tilde{b}_{\mathrm{OH^-}}$ and $\tilde{b}_{\mathrm{HCO_3^-}}$ given by Eqs. 3.18 and 3.26, we can write Eqs. 3.16 and 3.28 in terms of just one unknown coefficient, $\tilde{b}_{\mathrm{H^+}}$. The iterative process to obtain the solution to Eq. 3.16 with boundary conditions, Eq. 3.17, and Eqs. 3.18, 3.26, and 3.28, is similar to the case (a) for added counterions and water dissociation described before.

Case b.   In this case we have four different ionic species. Evaluating Eq. 3.9, particularized for the added counterions, of valency z_c, and the ions $\mathrm{H^+}$, $\mathrm{OH^-}$ and $\mathrm{HCO_3^-}$, at $x = h$ we obtain

$$\tilde{\Psi}^{0''}(h) = -z_c\tilde{b}_c - z_{\mathrm{H^+}}\tilde{b}_{\mathrm{H^+}} - z_{\mathrm{OH^-}}\tilde{b}_{\mathrm{OH^-}} - z_{\mathrm{HCO_3^-}}\tilde{b}_{\mathrm{HCO_3^-}} \qquad (3.29)$$

The added counterions counterbalance the overall charge on the particle surface, as in Eq. 3.22, whereas the number of ions $\mathrm{H^+}$, $\mathrm{OH^-}$ and $\mathrm{HCO_3^-}$ must balance due to the electroneutrality of the cell.

Using the relations between coefficients $\tilde{b}_{\mathrm{H}+}$, $\tilde{b}_{\mathrm{OH}^-}$ and $\tilde{b}_{\mathrm{HCO}_3^-}$ given by Eqs. 3.18 and 3.26, we can write Eqs. 3.16, 3.29, and 3.22 in terms of two unknown coefficients, $\tilde{b}_c$ and $\tilde{b}_{\mathrm{H}+}$. The iterative process to obtain the solution to Eq. 3.16 with boundary conditions, Eq. 3.17, and Eqs. 3.18, 3.26, 3.29, and 3.22, is similar to the case (b) for added counterions and water dissociation described before.

3.2 Method

We will discuss the results of the FIS+L model for the equilibrium. We will consider different realistic salt-free concentrated suspensions: suspensions with added counterions coincident, WDC (read it as Water Dissociation Coincident), or not, WDNC (Water Dissociation Non-Coincident), with the ions that stem from water dissociation, *i.e.*, H^+ or OH^-; and suspensions with added counterions coincident, WDACC (read it as Water Dissociation Atmospheric Contamination Coincident), or not, WDACNC (Water Dissociation Atmospheric Contamination Non-Coincident), with the ions that stem from water dissociation or atmospheric contamination, *i.e.*, H^+, OH^-, HCO_3^-. We will compare them with the results of the FIS+L model for ideal salt-free suspensions with only added counterions (SF), presented in Section 2.4. In order to show the realm of the finite ion size effect in realistic salt-free suspensions, the results are compared with the standard predictions for point-like ions, PL model [70].

Eqs. 3.11, 3.12 and 3.14 form a boundary value problem that can be solved numerically using the MATLAB routine bvp4c [107]. It can be easily demonstrated that solving the third-order problem is mathematically equivalent to finding the solution of the modified Poisson-Boltzmann problem, that is, any function satisfying Eqs. 3.11, 3.12 and 3.14 also satisfies Eqs. 3.5, 3.6, and 3.7, and vice versa. In both cases, we use an appropriate iterative process for the calculation of the b_i coefficients in the resolution of the differential equation. We set initial values for the different b_i coefficients, but the use of the third order problem with the addition of the boundary condition Eq. 3.14, improves the convergency giving rise to a better numerical resolution.

For all the calculations, the temperature has been taken equal to $T = 298.15$ K and the relative electric permittivity of the suspending liquid $\epsilon_{rs} = 78.55$, which coincides with that of the deionised water. Also, the valency of the added counterions has been chosen equal to $z_c = +1$, when they are of a different ionic species as that of the ions stemming from water dissociation

or atmospheric CO_2 contamination, and the particle radius $a = 100$ nm. We use the same ionic diameters, or correspondingly n^{max} values, than those shown in Section 2.2.

3.3   Results: equilibrium electric double layer

In this section we show the results for the equilibrium electric double layer in realistic salt-free concentrated suspensions including ion size effects. Once we have solved Eq. 3.11 with boundary conditions Eqs. 3.12 and 3.14, we calculate the equilibrium surface potential, $\Psi^0(a)$, for different particle charges and volume fractions to show the influence of ion size effects in these systems.

Fig. 3.1 shows the dimensionless equilibrium electric potential at the surface of the particle for a wide range of particle volume fractions. Dashed lines show the results of the FIS+L model. Solid lines present the results
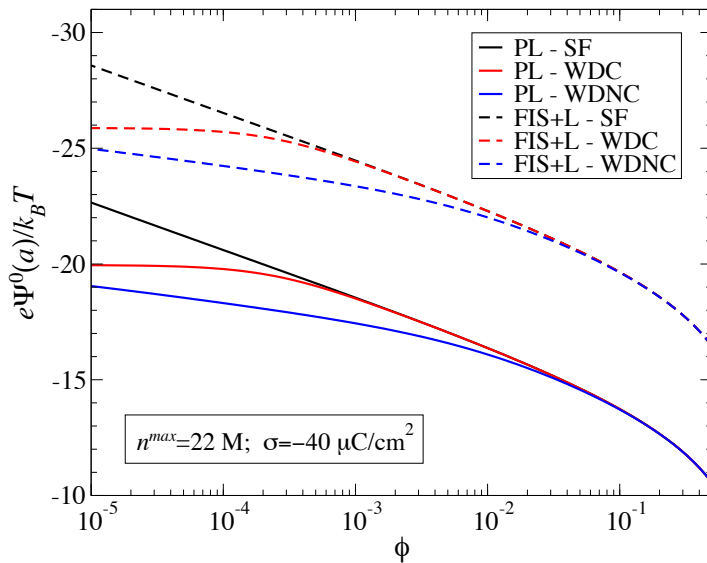

Figure 3.1: Dimensionless surface electric potential as a function of particle volume fraction. Dashed lines show the results of the FIS+L model with $n^{max} = 22$ M. Solid lines present the results for point-like ions. Black lines: only added counterions H^+ (SF). Red lines: added counterions H^+ with water dissociation ions (WDC). Blue lines: added counterions different than H^+ with $z_c = 1$ and water dissociation ions (WDNC).

for point-like ions. Black lines account for the results of ideal salt-free suspensions with only added counterions H^+ (SF). Red lines stand for realistic WDC suspensions with H^+ ions as added counterions, and blue lines for realistic WDNC suspensions with added counterions different than H^+ with $z_c = 1$. The particle surface charge density has been chosen equal to -40 $\mu C/cm^2$, and the maximum possible ionic concentration due to the excluded volume effect $n^{max} = 22$ M.

We observe in Fig. 3.1 that for high particle concentration the results for realistic suspensions with water dissociation ions are equal to those for ideal salt-free suspensions. The reason is that the added counterions completely mask the influence of water dissociation ions due to its larger concentration in the concentrated regime. The situation is very different when we approximate the dilute limit. For WDC suspensions with particle volume fraction $\phi \leq 10^{-3}$ the surface potential becomes approximately constant, in contrast with the growth noticed in an ideal salt-free suspension (SF). This behavior is due to the different sources of H^+ counterions: the added counterions released by the particles and those stemming from water dissociation. The first ones dominate in the high ϕ region, whereas the second ones do it at low particle concentration. The diminution of the surface potential in comparison with the ideal salt-free case can be explained by the increase of the counterions concentration inside the cell. For WDNC suspensions (dotted lines), there is an additional decrease of the surface potential and a wider influence of water dissociation to higher volume fraction values in comparison with the case of coincident counterions, WDC (dashed lines). This is due to the fact that now the added counterions do not participate in the water dissociation reaction. Therefore, the total number of counterions is larger than in the WDC case, causing a better screening of the particle charge and, consequently, diminishing the electric potential at the particle surface.

Fig. 3.1 also shows that the inclusion of ion size effects (FIS+L model) always rises the surface electric potential in comparison with the point-like predictions. The reason relies on the limitation of the ionic concentration in the neighborhood of the particle, which significantly diminishes the screening of the particle charge, and consequently, leading to an increment of the surface potential. We always find this behavior whatever the cases studied: SF, WDC or WDNC suspensions. When we deal with sufficiently high charged particles and finite size ions, a region of constant charge density develops very close to the particle surface with a thickness that is approximately independent of the volume fraction [53, 109]. This is in contrast
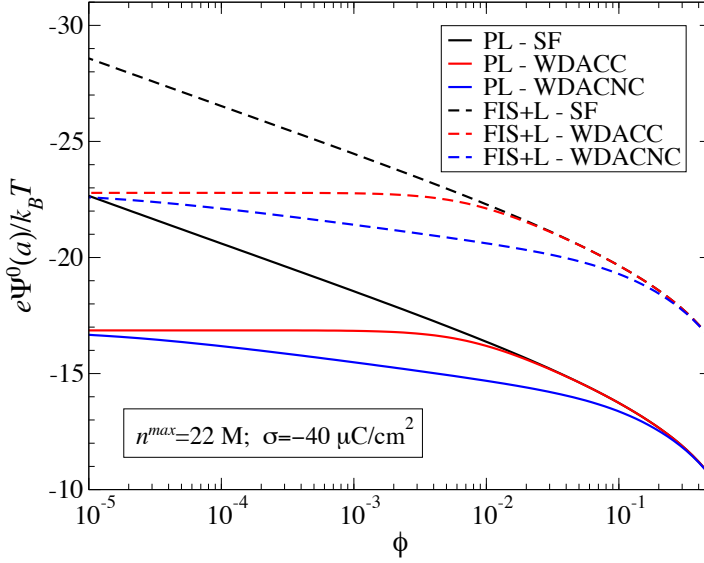
Figure 3.2: Dimensionless surface electric potential as a function of particle volume fraction. Dashed lines show the results of the FIS+L model with $n^{max} = 22$ M. Solid lines present the results for point-like ions. Black lines: only added counterions H^+ (SF). Red lines: added counterions H^+ with water dissociation and atmospheric contamination ions (WDACC). Blue lines: added counterions different than H^+ with $z_c = 1$ and water dissociation and atmospheric contamination ions (WDACNC).

with the classical point-like problem, where the charge density at the particle surface is unbounded and can reach unphysical values. The parallelism that exists between the solid and dashed lines is due to this counterions condensation region.

Fig. 3.2 shows the dimensionless equilibrium electric potential at the surface of the particle for a wide range of particle volume fractions. Dashed lines show the results of the FIS+L model with $n^{max} = 22$ M. Solid lines present the results for point-like ions. Black lines account for the results of ideal salt-free suspensions with only added counterions H^+ (SF). Red lines stand for realistic WDACC suspensions with H^+ ions as added counterions, and blue lines for realistic WDACNC suspensions with added counterions different than H^+ with $z_c = 1$. In the case of WDACC we observe again that for highly concentrated suspensions the results coincide with those of ideal salt-free predictions (SF), due to the added counterions dominance over

water dissociation and atmospheric contamination ions. In contrast with that shown in Fig. 3.1 for water dissociation ions, when we also consider atmospheric CO_2 contamination, the plateau in the surface potential now extends from the very dilute limit to $\phi = 10^{-2}$. In the present case, the H^+ counterions inside of the cell arise from three different mechanisms: the charging process of the colloidal particle, the water dissociation equilibrium, and the dissociated protons from atmospheric carbonic acid. Consequently, there is a great increase of the concentration of counterions that accounts for the marked reduction of the surface potential in the low volume fraction region.

For WDACNC suspensions Fig. 3.2 displays an additional decrease of the surface potential and an extended influence of the atmospheric CO_2 contamination for larger volume fractions in comparison with the case of WDACC suspensions. The explanation is based again on the fact that the non coincident added counterions do not participate in the water and carbonic acid dissociation reactions, yielding a large number of counterions in solution. The resulting screening of the particle charge is enhanced in comparison with the WDACC case, and therefore, the surface potential decreases.

Fig. 3.2 shows that the inclusion of ion size effects significantly increases the surface potential in comparison with point-like calculations. This is again due to the limitation of the ionic concentration in the neighborhood of the particle surface, which produces a diminution of the screening of the particle charge, and consequently, raising the surface potential. We again find this behavior irrespective of the cases studied: SF, WDACC or WDACNC suspensions.

Fig. 3.3 displays the dimensionless equilibrium surface electric potential for a wide range of particle surface charge densities, Fig. 3.3a, and particle volume fractions, Fig. 3.3b. We repeat this study for different salt-free suspensions, SF (black lines), WDC (red lines) and WDACC (blue lines), with added counterions coincident with H^+, and for the two PL (solid lines) and FIS+L (dashed lines) models. We take the maximum possible ionic concentration due to the excluded volume effect as $n^{max} = 22$ M, corresponding to a hydrated hydronium ion in solution. We observe in Fig. 3.3a that the diminution of the surface potential due to realistic considerations is practically independent of the particle surface charge density, for both point-like and finite size ions. The results of Fig. 3.3b confirm those from Figs. 3.1 and 3.2, and we can clearly see how the plateaus in the surface potential extend to larger volume fractions when we consider WDACC instead of WDC
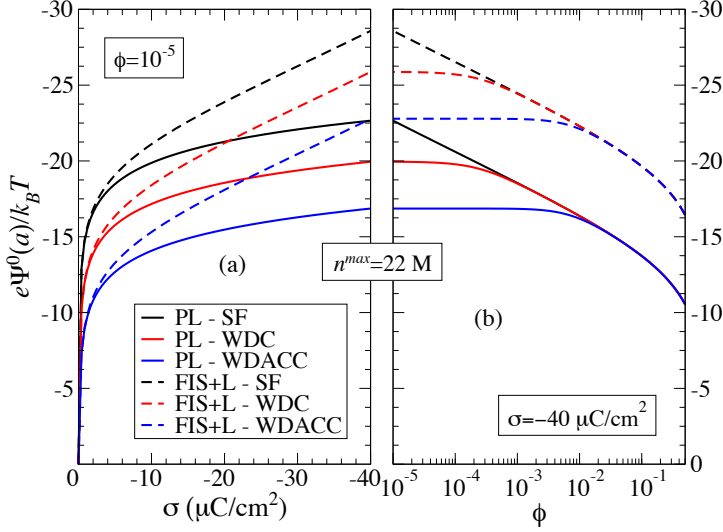
Figure 3.3: Dimensionless surface electric potential for different values of particle surface charge density (a) and particle volume fraction (b). Dashed lines show the results of the FIS+L model with $n^{max} = 22$ M. Solid lines present the results for point-like ions. Black lines: only added counterions H^+ (SF). Red lines: added counterions H^+ with water dissociation ions (WDC). Blue lines: added counterions H^+ with water dissociation and atmospheric contamination ions (WDACC).

suspensions.

Fig. 3.4 shows the dimensionless equilibrium surface electric potential for a wide range of particle surface charge densities, Fig. 3.4a, and particle volume fractions, Fig. 3.4b. We compare the results of the FIS+L model for different ion sizes (different dashed colored lines) with those for point-like ions (solid black lines). In all cases we study realistic salt-free suspensions with added counterions different than H^+ with $z_c = 1$ and water dissociation and atmospheric contamination ions (WDACNC). We find that the surface electric potential increases with the particle charge density, Fig. 3.4a. However, in some cases there is a different behavior in comparison with the point-like case. Initially, a fast and rough increase of the surface potential with the surface charge density is observed, which is followed by a much slower growth at higher surface charge densities for the PL case, or when the size of the ions is very small. This phenomenon is related to the classical counterion condensation effect: for high surface charges a layer of
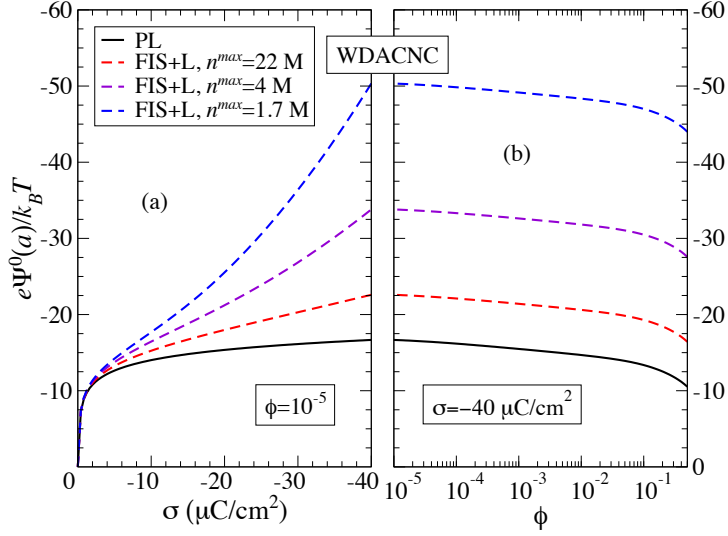
Figure 3.4: Dimensionless surface electric potential for different values of particle surface charge density (a) and particle volume fraction (b). Dashed lines present the results of the FIS+L model. Different colors stand for different counterion sizes. Solid black lines show the results for point-like counterions. In all cases we consider salt-free suspensions with added counterions different than H^+ with $z_c = 1$ and water dissociation and atmospheric contamination ions (WDACNC).

counterions develops very close to the particle surface [109]. When the ion size is taken into account, we limit the appearance of the classical condensation effect because when the surface charge is increased, the additional counterions join the condensate enlarging it. These profiles are similar to those found by for ideal salt-free suspensions in Section 2.4, but the values of the surface potential are lower for WDACNC suspensions than for SF suspensions, as we can see in Fig. 3.2.

On the other hand, the surface electric potential decreases when the particle volume fraction increases, irrespective of the cases studied: PL or FIS+L, Fig. 3.4b. When the particle concentration raises, the available space for the ions inside the cell decreases and, consequently, the screening of the particle charge augments, thus reducing the value of the surface potential.

Figs. 3.5 and 3.6 extend the results of Fig. 3.3 for realistic salt-free suspensions with added counterions coincident with H^+ and water dissociation
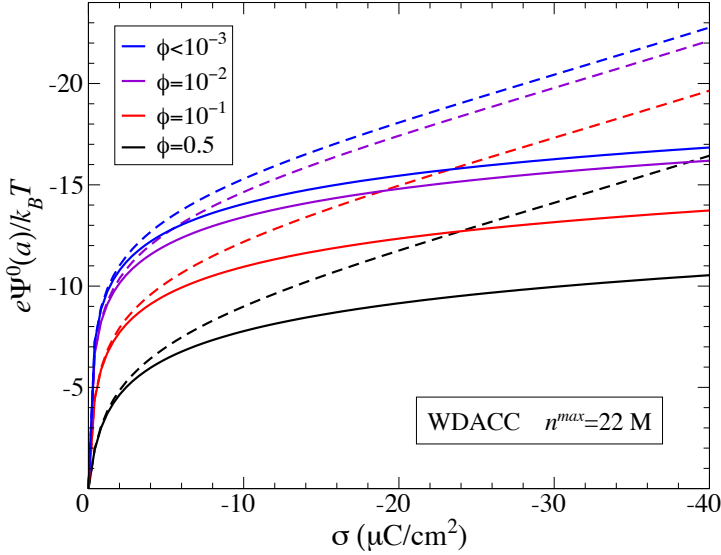
Figure 3.5: Dimensionless surface potential against the surface charge density for different particle volume fraction values. Solid lines show the results for point-like ions. Dashed lines show the results of the FIS+L model with $n^{max} = 22$ M. In all cases we consider salt-free suspensions with added counterions H^+ and water dissociation and atmospheric contamination ions (WDACC).

and atmospheric contamination ions (WDACC). In them, we compare the results of the FIS+L model for a given ion size, typical of an hydronium ion in solution (dashed lines), with those of the PL model (solid lines). Fig. 3.5 presents the dimensionless equilibrium surface electric potential at a wide range of particle surface charge densities. The different colored lines correspond to different particle volume fraction. The most remarkable fact shown in Fig. 3.5 is the large influence of the finite ion size effect even for moderately low particle surface charge densities. While for point-like predictions the surface potential hardly increases with surface charge for moderate to high surface charges at each volume fraction, the FIS+L results display an outstanding growth for the same conditions, associated with the lower charge screening ability of the counterions because of their finite size. This fact will surely have important consequences on the electrokinetic properties of such particles in concentrated realistic salt-free suspensions, as has already been shown for dilute suspensions in electrolyte solutions by
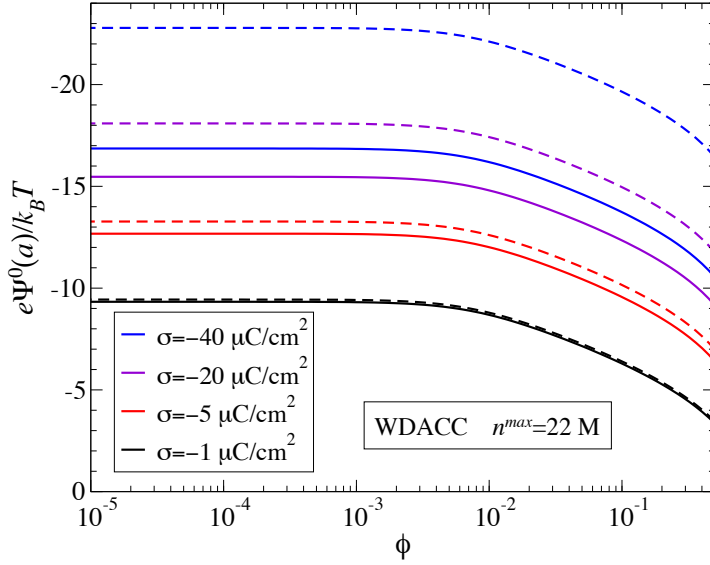
Figure 3.6: Dimensionless surface potential against the particle volume fraction for different surface charge density values. Solid lines show the results for point-like ions. Dashed lines show the results of the FIS+L model with $n^{max} = 22$ M. In all cases we consider salt-free suspensions with added counterions H^+ and water dissociation and atmospheric contamination ions (WDACC).

Aranda-Rascón *et al.* [11, 49].

Finally, Fig. 3.6 shows the dimensionless equilibrium electric potential at the particle surface against the particle volume fraction. The different colored lines correspond to different negative particle surface charge densities. As previously stated, the particle surface potential shows an initial plateau in the dilute region followed by a monotonous decrease with volume fraction at fixed particle charge density. For the ionic size chosen, the larger the surface charge, the larger the relative increase of the surface potential at every volume fraction, due to the enlarging of the counterion condensate in the neighborhood of the particle surface.

From the results, we think that it is clear that the influence of the finite ion size effect on the EDL description cannot be neglected for many typical particle charges and volume fractions, either in an ideal or in a realistic salt-free suspension.

3.4   Preliminary experimental results

We have presented a theoretical model to include ion size effects in the electrokinetics of salt-free concentrated suspensions. In this section we show some preliminary experimental measurements performed in the Laboratory of Prof. Ángel Delgado (Universidad de Granada, Spain). Both the static and dynamic electrophoretic mobility of the suspended particles were measured to test the validity of our model and the influence of ion size effects.

3.4.1   Electrophoretic mobility

As we have seen in Subsection 2.3.1, the electrophoretic mobility can be defined from the relation between the electrophoretic velocity of the particle $\mathbf{v}_e$ and the macroscopic electric field $\langle \mathbf{E} \rangle$. There are different ways to determine it experimentally. The most common method is called microelectrophoresis [79]. It is based on the direct observation, with suitable magnifying optics, of individual particles in their electrophoretic motion.

   This visual technique has been replaced by automatic methods based on the analysis of the laser light scattered by electrophoresing particles, known as electrophoretic light-scattering methods [79]. In general, their principle of operation is as follows: due to the Doppler shift of the scattered light, a beat pattern is produced in the detection photomultiplier, the frequency of which can be related to the electrophoretic velocity. Such a frequency can be measured by means of a spectrum analyzer or by analysis of the correlation function of the scattered light.

   Using Malvern's Zetasizer Nano [113], which is based on an electrophoretic light-scattering method, we have measured the electrophoretic mobility of highly charged sulfonated polystyrene latexes. These latexes were synthesized by Ikerlat Polymers [114]. The particle surface charge and particle radius values given by the manufacturer were $\sigma = -31.67 \ \mu C/cm^2$ and $a = 38$ nm, respectively. The charged particles were suspended in a salt-free medium with H^+ ions as added counterions and originally at a particle volume fraction $\phi = 0.206$. From the initial suspension, we prepared dilutions at $\phi = 10^{-2}$, $5 \cdot 10^{-3}$, 10^{-3}, $5 \cdot 10^{-4}$ and 10^{-4} using deionized and filtered water.

   Fig. 3.7 shows in black dots the measured values of the scaled electrophoretic mobility for different volume fractions. For each ϕ, three volumes were taken from the suspension and each one measured three times. The black dots are the average of these measurements. Due to technique limitations related with the light scattered from the particles, no measure-
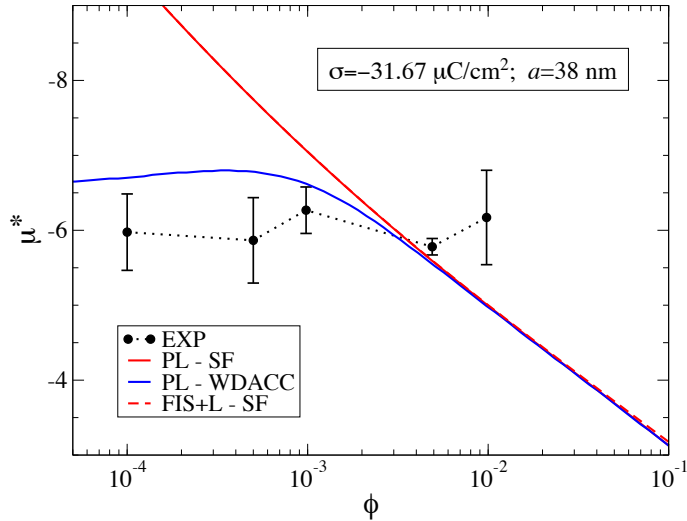
Figure 3.7: Scaled electrophoretic mobility of the particles as a function of volume fraction. • points stand for experimental measurements. Solid and dashed red lines show the results of PL model and FIS+L model with $n_c^{max} = 22$ M, respectively, in ideal salt-free suspensions with only added counterions H^+. Blue solid line stand for the results of PL model in realistic salt-free suspensions with added counterions H^+ and water dissociation and atmospheric contamination ions (WDACC) from Ref. [71].

ments are presented in the range of high and very low ϕ. From the results, it is possible to conclude that the electrophoretic mobility takes a constant value for such volume fractions (plateau in the Figure) that corresponds with the dilute limit.

We compare these measurements with theoretical calculations for ideal salt-free suspensions made with PL and FIS+L models, solid and dashed red lines, respectively. We note that both model predict the same results because of the low particle volume fraction values, despite of the high particle surface charge. The only small difference appears when ϕ increases to the concentrate region. We observe that the theoretical results do not match with the experimental measurements. Both models predict an almost linear increment of the mobility when decreasing the volume fraction, in contrast with the plateau observed with black dots in Fig. 3.7. The reason is that we do not consider water dissociation ions and atmospheric CO_2 contamination ions in ideal salt-free suspensions. As we have seen in Section 3.3, these ions

dominates in the low ϕ region.

To deal with that, we show in the blue line the results of the PL model for realistic salt-free suspensions with added counterions H^+ and water dissociation and atmospheric contamination ions (WDACC) from Ref. [71]. There are no results of the FIS+L model for realistic salt-free suspensions because only the equilibrium EDL has been studied in these systems including ion size effects. When these extra ions are considered we get closer to experimental conditions because the suspension had water as liquid medium and was open to the atmosphere. We observe that now the theoretical results present a plateau in the mobility for low volume fractions. The diminution of the mobility in comparison with the ideal salt-free case can be explained by the increase of the counterions concentration inside the cell. This theoretical plateau is slightly over the experimental one, but it is important to note that there are no adjustable parameters in the model. The use of a renormalized charge instead of the bare charge would probably improve the matching.

It is not possible to measure the mobility for high particle volume fractions with the device used because almost all the light is absorbed by the suspension and consequently no scattered light is detected. This is the reason because we are not able to check experimentally the diminution of the mobility for high ϕ. Other experimental techniques, like super-heterodyne light scattering ones, are able to measure in the concentrated region and have found this diminution [61, 63].

This experiment shows that it is necessary to consider realistic salt-free suspensions to get closer to experimental conditions, specially for low particle volume fractions.

3.4.2   Dynamic electrophoretic mobility

When the external electric field applied to the suspension is oscillating, $\langle \mathbf{E} \rangle \mathrm{e}^{-i\omega t}$, our concern relies in the dynamic electrophoretic mobility. As we have seen in Section 2.6, the value of the dynamic mobility for $\omega = 0$ coincides with that of static electric fields. When the frequency of the external electric field increases, this value is modified because of the relaxation of the electromigration and diffusion processes developed around the particle. We have experimentally measured the dynamic mobility of the suspended particles using the Electrokinetic Sonic Amplitude technique. This is an electroacoustic technique based on the determination of the amplitude and phase of the sound wave generated in the colloidal suspension by application of an oscillating field [57, 115].

The device used is Colloidal Dynamics's Acoustosizer II [116], which operates in the frequency interval between 1 and 18 MHz. We have measured the dynamic mobility of highly charged sulfonated polystyrene latexes, $\sigma = -31.67 \ \mu C/cm^2$ and $a = 38$ nm, synthesized by Ikerlat Polymers [114]. The charged particles were suspended in a salt-free medium with H^+ ions as added counterions and originally at a particle volume fraction $\phi = 0.206$. From the initial suspension, we prepared dilutions at $\phi = 0.152$, 0.097 and 0.049 using deionized and filtered water.

Fig. 3.8 presents in colored dots the measurements of the modulus of the scaled dynamic mobility as a function of frequency. Different colors stand for different volume fractions. For each ϕ, two volumes were taken from the suspension and each one measured four times. The dots are the average of these measurements. From the results, we observe that the dynamic mobility takes a constant value for the initial frequencies measured, and starts to rise for the last measurements. These behaviors can be associated with the common low frequency plateau and with the beginning of the
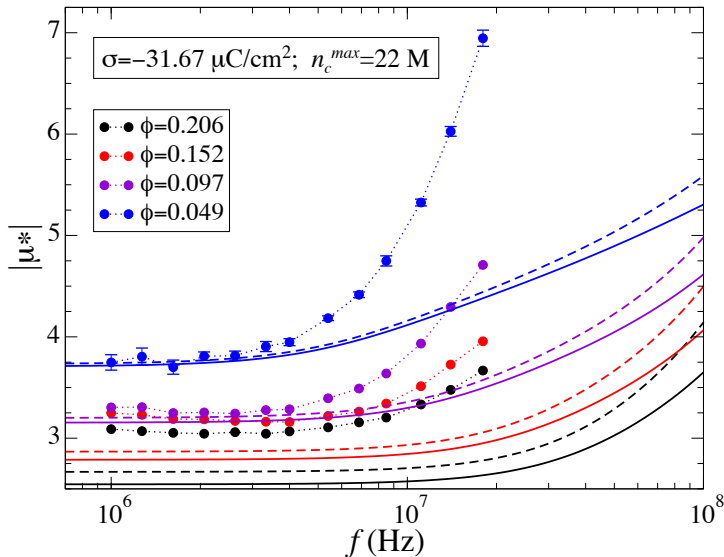

Figure 3.8: Modulus of the scaled dynamic electrophoretic mobility of the particles as a function of frequency. ● points stand for experimental measurements. Solid and dashed lines show the results of PL model and FIS+L model with $n_c^{max} = 22$ M, respectively. Different colors stand for different particle volume fractions.

MWO relaxation, respectively. We note that the frequency of the MWO relaxation is lower the lower the volume fraction, and that the value of the plateau increases when ϕ decreases.

We compare these measurements with theoretical calculations for ideal salt-free suspensions made with PL and FIS+L models, solid and dashed colored lines, respectively. There are no adjustable parameters in the models. We use as input the bare charge of the particle, $\sigma = -31.67\ \mu C/cm^2$, and for the FIS+L model we also consider hydrated H^+ counterions with $n_c^{max} = 22$ M. The theoretical results match qualitatively with the experimental measurements. In general, we find that the measured low frequency plateaus are higher than the predicted ones and that the MWO relaxations occur one decade before in frequency. Curiously, when ϕ decreases, there is a better agreement for the low frequency plateau value but the differences with the MWO relaxation frequency increase. We find quantitative differences between the predictions of both theoretical models. We observe that the FIS+L model predicts a higher value for the low frequency plateau as well as a lower relaxation frequency, specially in the high frequency region not shown in Fig. 3.8, than those predicted by the PL model. These differences diminish when the volume fraction also does it. In all the cases the predictions of the FIS+L model are closer to the experiments for these highly charged particles.

Figs. 3.9 and 3.10 show again the experimental results of the modulus of the dynamic mobility for $\phi = 0.206$ in black dots. We compare the results with the predictions of the PL and FIS+L models, solid and dashed lines, respectively. In Fig. 3.9 we fix n_c^{max} and perform the calculations for different particle surface charges. We observe that the diminution of the particle charge leads to a better agreement between experiment and theory in both the low frequency plateau value and MWO relaxation frequency. This agreement is better again for the FIS+L model. The aim of these calculations is that the electrokinetic charge is usually lower than the bare charge. Although the agreement is promising, we find that the perfect match would be obtained with unrealistic values of σ. In Fig. 3.10 we fix the particle charge and change the ion size. The values $n_c^{max} = 22$, 5 and 2.5 M correspond to ionic diameters of $2R = 0.425$, 0.693 and 0.873 nm, respectively. As ion-ion interactions are underestimated by the FIS+L model, the consideration of larger ion sizes would enhance them indirectly. Even though we have again a great qualitative agreement that also improves quantitatively for higher ion sizes, we are not able to match the low frequency plateau and the MWO relaxation frequency at the same time.

Figure 3.9: Modulus of the scaled dynamic electrophoretic mobility of the particles as a function of frequency. • points stand for experimental measurements. Solid and dashed lines show the results of PL model and FIS+L model with $n_c^{max} = 22$ M, respectively. Different colors stand for different particle surface charge densities.
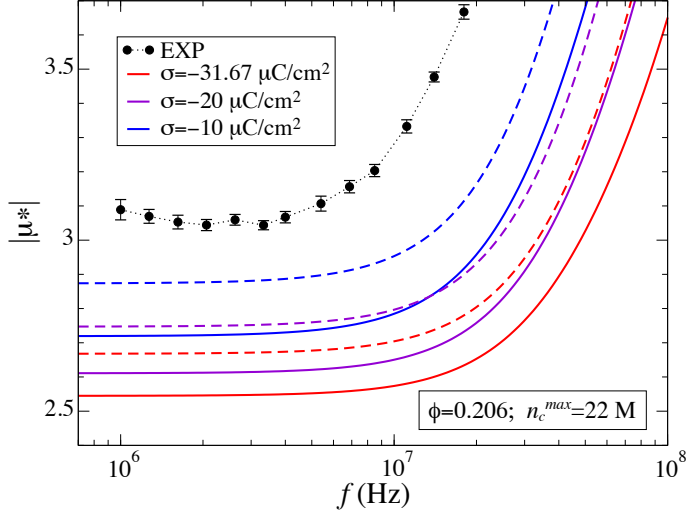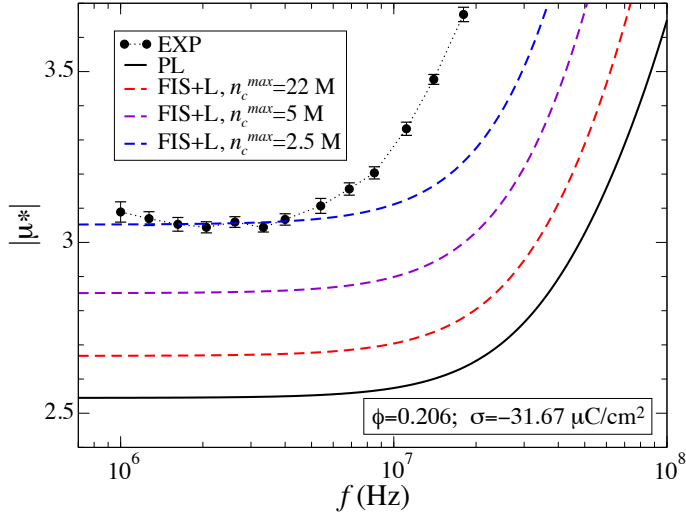

Figure 3.10: Modulus of the scaled dynamic electrophoretic mobility of the particles as a function of frequency. • points stand for experimental measurements. The results for point-like ions are shown in the solid black line. Different dashed colored lines stand for the results of FIS+L model for different ion sizes.

Summarizing, we have found a good qualitative agreement in the case of the dynamic mobility that improves quantitatively in all the cases when ion size effects are considered for the highly charged colloidal particles used.

Works in progress concerning realistic salt-free concentrated suspensions are expected to clarify this issue, and will be our major concern in the next future. It seems that charge transport processes in real suspensions cannot follow the oscillating electric field at frequencies where the theoretical transport mechanism do not suffer appreciable lag with the field. Although a larger particle radius could explain lower MWO relaxation frequencies in agreement with experimental results, there is no evidence of particle aggregation at such high particle charges. A more extensive experimental study has to be done to explain the origin of such discrepancies, by changing particle size, charge density and volume fraction, and specially by alternative estimation of the electrokinetic or effective particle charge in order to be compared with the bare one.

Chapter 4

Conclusions

By using a spherical cell approach we have analyzed the influence of finite ion size effects in the response of a salt-free concentrated suspension of spherical particles to static and oscillating electric fields. We have derived a mean-field electrokinetic model that accounts for the excluded volume of the counterions.

We have seen that the inclusion of ion size effects significantly modifies the ionic condensation region near the particle surface for moderate to high particle charges. This produces a change in the convective fluid flow and in the counterions fluxes, as well as a remarkable diminution of the electrophoretic retardation force acting on the particle when an external static electric field is applied. In the common case of H^+ counterions, this leads to an increment of both the electrophoretic mobility and the suspension conductivity in comparison with the point-like case. This increment grows with ion size and particle charge.

In the frequency domain, we have studied the dynamic electrophoretic mobility of the particles and the dielectric response of the suspension. For this purpose we have performed a comparative study of the different physical mechanisms, *pure inertia response* and charge polarization relaxations, to know how they interplay in giving the complete response. This study has allowed us to characterize the relative importance and relaxation frequencies of each mechanism separately. In the discussion of the numerical results two different MWO relaxations have been successfully associated with the relaxations of the different ionic processes that take place in the diffuse and condensate regions of the EDL. Furthermore, the inclusion of ion size effects leads to an overall increment of the dynamic mobility and relative permittivity in comparison with the point-like case. The enhancement of the

MWO relaxation for moderate to high particle charges, which is associated with the counterions condensation layer, has yielded a remarkable increment of the mobility for such frequencies. In addition, we have found that this increment of the mobility grows with ion size and particle charge. Besides, we have observed a shift in the MWO relaxation of the condensate to larger frequencies with ion size.

In an attempt to get closer to experimental systems, we have also derived a model to include ion size effects in the equilibrium EDL of spherical particles in realistic salt-free concentrated suspensions. These realistic suspensions include water dissociation ions and those generated by atmospheric carbon dioxide contamination in addition to the added counterions released by the particles to the solution. The numerical results have shown that the influence of the water dissociation in aqueous salt-free suspensions has to be considered for volume fractions lower than 10^{-2}, whereas the atmospheric contamination, if the suspensions are in contact with air, is significant in the region of $\phi < 10^{-1}$. Moreover, they have demonstrated that it is important to distinguish whether the added counterions coincide or not with one of the ionic species arising from the dissociation of water and carbonic acid. The results have also shown that the finite ion size effect has to be taken into account for moderate to high particle charges at every particle volume fraction. This equilibrium model will be used to develop nonequilibrium models of the response of realistic salt-free concentrated suspensions to external electric fields including ion size effects.

To test the validity of the electrokinetic model presented in this thesis, we have made a preliminary set of experiments to measure the static and dynamic mobility of highly charged sulfonated polystyrene latexes in salt-free concentrated suspensions. We have found a good qualitative agreement between theory and experiment in the case of the dynamic mobility that improves in all the cases when ion size effects are considered. For the measurements of the static electrophoretic mobility at low volume fractions, we have been forced to consider realistic salt-free suspensions to find such agreement. We consider that it would be necessary to improve these experiments by performing a systematic study with an established protocol. In particular, it would be interesting to repeat these experiments with other particle charges and sizes, and also with other ionic species, like K^+ or Na^+, instead of H^+ counterions. Dielectric spectroscopy measurements of the same suspensions will also add useful information about the weight of ion size effects in the overall electrokinetic response.

Appendix A

Invariance of MPB equation

In this Appendix we demonstrate that the new modified Poisson-Boltzmann equation (MPB), Eq. 2.13, is invariant under changes in the origin of the electric potential, as it must be according to basic physical grounds. This is not a trivial question, because the classical Poisson-Boltzmann equation for the low particle concentration case in electrolyte solutions is not invariant under changes in the origin of the electric potential: it is only valid when we take the potential zero at an infinite distance from the particle surface (bulk). When we study salt-free and/or concentrated suspensions, we do not have a bulk, because the electroneutrality is achieved at the outer surface of the cell, and we have to take care about the correct invariance of the equation. In this case we do not have an "infinity" to set the origin of the potential and we have also an unknown coefficient b_c that must be correctly defined to account for the latter statements. The Poisson-Boltzmann description for the salt-free case with point-like counterions made by Ruiz-Reina and Carrique [70] satisfies the above-mentioned invariance requirement.

As we said before, the unknown coefficient b_c, that appears in the MPB equation, Eq. 2.13, represents the ionic concentration where the equilibrium electric potential is zero. Our choice along this work has been $\Psi^0(b) = 0$. According to this definition and using Eq. 2.11, we can see that $n_c^0(b) = b_c$.

The potential difference between two points r, r_1 does not depend on the origin of potentials, Fig. A.1,

$$\Psi^0(r) - \Psi^0(r_1) = \Psi^{0*}(r) - \Psi^{0*}(r_1) \qquad (A.1)$$

where the magnitudes without asterisks refer to the origin $\Psi^0(b) = 0$ and those with asterisks, to an arbitrary origin, $\Psi^{0*}(r_1) = 0$, for the electric
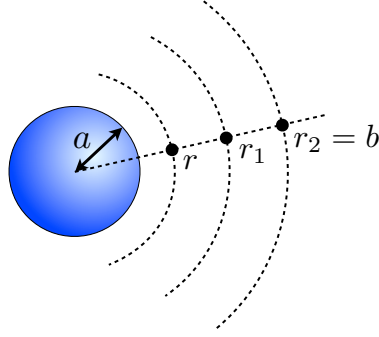
Figure A.1: Changes in the origin of the electric potential.

potential. The relationship between the potentials referred to both choices of electric potential origins is

$$\Psi^0(r) = \Psi^{0*}(r) + \Psi^0(r_1) \tag{A.2}$$

Substituting the last expression in the MPB equation, Eq. 2.13, we obtain

$$\frac{\mathrm{d}^2\Psi^{0*}(r)}{\mathrm{d}r^2} + \frac{2}{r}\frac{\mathrm{d}\Psi^{0*}(r)}{\mathrm{d}r}$$

$$= -\frac{z_c e}{\epsilon_0 \epsilon_{rs}} \frac{b_c \exp\left(-\frac{z_c e \Psi^{0*}(r)}{k_B T}\right) \exp\left(-\frac{z_c e \Psi^0(r_1)}{k_B T}\right)}{1 + \frac{b_c}{n_c^{max}} \left[\exp\left(-\frac{z_c e \Psi^{0*}(r)}{k_B T}\right) \exp\left(-\frac{z_c e \Psi^0(r_1)}{k_B T}\right) - 1\right]} \tag{A.3}$$

After a little algebra, and defining

$$b_c^* = \frac{b_c}{\left(1 - \frac{b_c}{b_c^{max}}\right) \exp\left(-\frac{z_c e \Psi^0(r_1)}{k_B T}\right) + \frac{b_c}{b_c^{max}}} \tag{A.4}$$

it yields

$$\frac{\mathrm{d}^2\Psi^{0*}(r)}{\mathrm{d}r^2} + \frac{2}{r}\frac{\mathrm{d}\Psi^{0*}(r)}{\mathrm{d}r}$$

$$= -\frac{z_c e}{\epsilon_0 \epsilon_{rs}} \frac{b_c^* \exp\left(-\frac{z_c e \Psi^{0*}(r)}{k_B T}\right)}{1 + \frac{b_c^*}{n_c^{max}} \left[\exp\left(-\frac{z_c e \Psi^{0*}(r)}{k_B T}\right) - 1\right]} = -\frac{z_c e}{\epsilon_0 \epsilon_{rs}} n_c^{0*}(r) \tag{A.5}$$

where we have defined

$$n_c^{0*}(r) = \frac{b_c^* \exp\left(-\frac{z_c e \Psi^{0*}(r)}{k_B T}\right)}{1 + \frac{b_c^*}{n_c^{max}} \left[\exp\left(-\frac{z_c e \Psi^{0*}(r)}{k_B T}\right) - 1\right]} \tag{A.6}$$

Eq. A.5 shows that $\Psi^{0*}(r)$ satisfies the MPB equation, Eq. 2.13, with a different coefficient b_c^*. Let's finally check that the concentration of counterions, $n_c^{0*}(r)$, is the same irrespective of the origin of the electric potential: $n_c^{0*}(r) = n_c^0(r)$, in spite of the different values of the unknown coefficients b_c and b_c^*.

By inserting Eq. A.4 in Eq. A.6, we obtain

$$n_c^{0*}(r) = \frac{b_c}{\left(1 - \frac{b_c}{b_c^{max}}\right)\exp\left(-\frac{z_c e \Psi^0(r_1)}{k_B T}\right) + \frac{b_c}{b_c^{max}}}$$

$$\times \frac{\exp\left(-\frac{z_c e \Psi^{0*}(r)}{k_B T}\right)}{1 + \frac{b_c}{n_c^{max}} \frac{\left[\exp\left(-\frac{z_c e \Psi^{0*}(r)}{k_B T}\right) - 1\right]}{\left(1 - \frac{b_c}{b_c^{max}}\right)\exp\left(-\frac{z_c e \Psi^0(r_1)}{k_B T}\right) + \frac{b_c}{b_c^{max}}}}$$

$$= \frac{b_c \exp\left(-\frac{z_c e \Psi^0(r)}{k_B T}\right)}{1 + \frac{b_c}{n_c^{max}} \left[\exp\left(-\frac{z_c e \Psi^0(r)}{k_B T}\right) - 1\right]} = n_c^0(r) \tag{A.7}$$

as we wanted to demonstrate.

Appendix B

Electrocinética de suspensiones concentradas salt-free con tamaño iónico finito

Introducción

En los últimos años se ha producido un renovado interés por la electroforesis. Este interés es en parte debido a avances recientes en nanociencia que hacen posible la separación de macromoléculas por tamaño o carga. Por ejemplo, moléculas de ADN o proteínas en suspensión son dirigidas y separadas mediante campos eléctricos ac o dc [1–3]. Otra aplicación fundamental en el campo de la nanociencia es el uso de nanopartículas de oro para la administración de fármacos o para la detección de células cancerígenas [4,5]. Se ha encontrado que las medidas de la movilidad electroforética de estas nanopartículas de oro es útil para caracterizar su funcionalización superficial [6]. Es un hecho conocido que las partículas adquieren carga al ser suspendidas en solución junto con microiones. En estas condiciones, se forma una estructura de doble capa eléctrica alrededor de la partícula [7–9]. La movilidad electroforética de una partícula en suspensión no depende únicamente de la carga de dicha partícula o de la viscosidad del medio, sino también de la configuración de la doble capa eléctrica.

La mayoría de los modelos teóricos para la doble capa eléctrica están basados en la ecuación de Poisson-Boltzmann, que está basada en una aproximación de campo medio que considera iones puntuales en solución. Esta

teoría deja de funcionar cuando la acumulación de iones es significativa y cuando la repulsión por tamaño iónico y las correlaciones son importantes. Algunos autores han mostrado que la consideración de efectos de tamaño iónico finito permite la acumulación de iones en las proximidades de la superficie de la partícula [10]. Esta redistribución de iones modifica la doble capa eléctrica alrededor de la partícula y por tanto su movilidad electroforética cuando se aplica un campo eléctrico [11–14].

Podemos encontrar en la literatura distintos estudios que tratan efectos de tamaño iónico finito. Algunos de ellos discuten descripciones microscópicas de las correlaciones ión-ión [15–30]. Estas aproximaciones están restringidas fundamentalmente a condiciones de equilibrio, pero son capaces de predecir fenómenos importantes como la inversión de carga [31,32]. Otros estudios están basados en descripciones macroscópicas que consideran interacciones promedio mediante aproximaciones de campo medio [10–14,33–55]. En muchos de estos trabajos, el tamaño iónico es considerado a través de una modificación en el coeficiente de actividad de los iones en el potencial electroquímico, o incorporando contribuciones entrópicas relacionadas con el volumen excluido por los iones. Al comparar las predicciones de las aproximaciones macroscópicas con resultados de simulación, se ha encontrado que éstas funcionan razonablemente bien con electrolitos monovalentes en condiciones de alta carga de partícula y/o gran tamaño iónico [15].

La mayoría de los trabajos en electrocinética tienen en cuenta suspensiones con baja concentración de partículas, pese a que hoy en día es el régimen concentrado el que atrae mayor atención debido a sus aplicaciones prácticas [56]. Las interacciones electrohidrodinámicas partícula-partícula aumentan con la concentración de partículas, lo que hace que estos sistemas concentrados sean más complejos de estudiar [57,58]. Por otra parte, los sistemas con baja concentración de sal muestran un menor apantallamiento de las interacciones electrostáticas partícula-partícula de tipo repulsivo, lo que favorece la generación de cristales coloidales o vidrios [59]. Llamamos suspensiones salt-free ideales, o suspensiones salt-free, a aquellas compuestas únicamente por partículas cargadas y por sus contracargas iónicas (conocidas como contraiones añadidos). El interés en estos sistemas ha aumentado en los últimos años desde los puntos de vista teórico y experimental [14,53–55,60–76].

El objetivo de esta Tesis es analizar la influencia del tamaño iónico finito en la respuesta de una suspensión concentrada salt-free a campos eléctricos estáticos y oscilantes. Estudiaremos especialmente la movilidad electroforética estática y dinámica de las partículas y la conductividad y la

respuesta dieléctrica de la suspensión, así como la doble capa eléctrica de equilibrio [14, 53, 54]. Para acercarnos a condiciones experimentales, discutiremos también la doble capa eléctrica de equilibrio en suspensiones concentradas salt-free realistas. Estas suspensiones realistas incluyen a los iones procedentes de la disociación del agua y a los generados por contaminación por CO_2 atmosférico, además de los contraiones añadidos liberados por las partículas a la solución. Para comprobar la validez de estos modelos, compararemos algunos de estos cálculos con resultados experimentales preliminares de la movilidad estática y dinámica de partículas coloidales altamente cargadas.

Modelo

Estudiamos las propiedades macroscópicas de la suspensión mediante una aproximación de celda esférica [101, 105]. Dichas propiedades son obtenidas mediante promedios apropiados de propiedades locales en una celda representativa. En esta aproximación, una partícula esférica de radio a es rodeada por una capa concéntrica de medio líquido, teniendo un radio externo b de forma que la razón del volumen partícula/celda en la celda es igual a la fracción de volumen de partícula en la suspensión completa, Fig. 1.2, es decir

$$\phi = \left(\frac{a}{b}\right)^3 \tag{B.1}$$

En esta aproximación simulamos las interacciones hidrodinámicas y eléctricas entre partículas en la suspensión mediante la correcta especificación de condiciones de contorno en la frontera externa de la celda.

Consideremos una partícula cargada con densidad superficial de carga σ inmersa en un medio salt-free ideal con permitividad relativa ϵ_{rs} y con la única presencia de sus contraiones añadidos de valencia z_c. Tenemos en cuenta el tamaño finito de los contraiones al tratarlos como esferas de radio R con una carga puntual en su centro. Al aplicar al sistema un campo eléctrico oscilante $\mathbf{E}\, e^{-i\omega t}$, la partícula se mueve con una velocidad electroforética dinámica $\mathbf{v}_e e^{-i\omega t}$. Los ejes del sistema de coordenadas esférico están fijos en en el centro de la partícula, con el eje polar $\theta = 0$ paralelo al campo eléctrico. La solución del problema en un instante t requiere del conocimiento en cada punto $\mathbf{r}$ del sistema del potencial eléctrico, $\Psi(\mathbf{r}, t)$, de la concentración iónica, $n_c(\mathbf{r}, t)$, de su velocidad, $\mathbf{v}_c(\mathbf{r}, t)$, de la velocidad del fluido, $\mathbf{v}(\mathbf{r}, t)$, y de la presión, $P(\mathbf{r}, t)$. Las ecuaciones electrocinéticas

fundamentales que conectan estas magnitudes son [7, 103]:

$$\nabla^2 \Psi(\mathbf{r}, t) = -\frac{z_c e}{\epsilon_0 \epsilon_{rs}} n_c(\mathbf{r}, t) \tag{B.2}$$

$$\eta \nabla^2 \mathbf{v}(\mathbf{r}, t) - \nabla P(\mathbf{r}, t) - z_c e n_c(\mathbf{r}, t) \nabla \Psi(\mathbf{r}, t) = \rho_s \frac{\partial}{\partial t} [\mathbf{v}(\mathbf{r}, t) + \mathbf{v}_e \, e^{-i\omega t}] \tag{B.3}$$

$$\nabla \cdot [n_c(\mathbf{r}, t) \mathbf{v}_c(\mathbf{r}, t)] = -\frac{\partial}{\partial t} [n_c(\mathbf{r}, t)] \tag{B.4}$$

$$n_c(\mathbf{r}, t) \mathbf{v}_c(\mathbf{r}, t) = n_c(\mathbf{r}, t) \mathbf{v}(\mathbf{r}, t) - \frac{1}{\lambda_c} n_c(\mathbf{r}, t) \nabla \mu_c(\mathbf{r}, t) \tag{B.5}$$

$$\nabla \cdot \mathbf{v}(\mathbf{r}, t) = 0 \tag{B.6}$$

Estamos interesados en el estudio de la respuesta lineal del sistema a un campo eléctrico y por tanto aplicamos el siguiente esquema de perturbación: escribimos cada cantidad X como la suma de su valor en el equilibrio, X^0, más un término de perturbación, δX, que depende linealmente con el campo multiplicado por el término $e^{-i\omega t}$.

Introducimos el tamaño finito de los contraiones incluyendo un nuevo término, la entropía de las moléculas del solvente, en la energía libre de la suspensión [38, 53]. Teniendo en cuenta una aproximación de campo medio, podemos escribir la energía libre total del sistema, $F = U - TS$, en términos del potencial eléctrico de equilibrio y de la concentración de contraiones $n_c^0(\mathbf{r})$. Las distintas contribuciones de energía interna configuracional, U, y entrópica, $-TS$, son

$$U = \int d\mathbf{r} \left[-\frac{\epsilon_0 \epsilon_{rs}}{2} |\nabla \Psi^0(\mathbf{r})|^2 + z_c e n_c^0(\mathbf{r}) \Psi^0(\mathbf{r}) - \mu_c^0 n_c^0(\mathbf{r}) \right] \tag{B.7}$$

$$-TS = k_B T n_c^{max} \int d\mathbf{r} \left[\frac{n_c^0(\mathbf{r})}{n_c^{max}} \ln \left(\frac{n_c^0(\mathbf{r})}{n_c^{max}} \right) \right. $$
$$\left. + \left(1 - \frac{n_c^0(\mathbf{r})}{n_c^{max}} \right) \ln \left(1 - \frac{n_c^0(\mathbf{r})}{n_c^{max}} \right) \right] \tag{B.8}$$

donde n_c^{max} es la máxima concentración posible de contraiones debido al efecto de volumen excluído, definida como $n_c^{max} = V^{-1}$, siendo V el volumen promedio ocupado por un ión en solución. El segundo término en la Ec. B.8 tiene en cuenta el tamaño iónico finito y modifica la ecuación clásica de Poisson-Boltzmann [38].

Obtenemos la nueva concentración de contraiones de equilibrio minimizando la energía libre $F = U - TS$ con respecto a $n_c^0(\mathbf{r})$

$$n_c^0(\mathbf{r}) = \frac{b_c \exp\left(-\frac{z_c e \Psi^0(\mathbf{r})}{k_B T}\right)}{1 + \frac{b_c}{n_c^{max}}\left[\exp\left(-\frac{z_c e \Psi^0(\mathbf{r})}{k_B T}\right) - 1\right]} \tag{B.9}$$

donde b_c es un coeficiente desconocido que representa el valor de la concentración iónica donde tomamos potencial eléctrico nulo. Usamos la condición de electroneutralidad de la celda para obtener este coeficiente.

En el equilibrio no hay campo externo aplicado y la partícula es rodeada por una distribución simétrica y esférica de carga. Aplicando esta simetría e introduciendo el valor de $n_c^0(\mathbf{r})$ en la ecuación de Poisson, obtenemos una ecuación de Poisson-Boltzmann modificada para el potencial eléctrico de equilibrio

$$\frac{d^2\Psi^0(r)}{dr^2} + \frac{2}{r}\frac{d\Psi^0(r)}{dr} = -\frac{z_c e}{\epsilon_0 \epsilon_{rs}} \frac{b_c \exp\left(-\frac{z_c e \Psi^0(r)}{k_B T}\right)}{1 + \frac{b_c}{n_c^{max}}\left[\exp\left(-\frac{z_c e \Psi^0(r)}{k_B T}\right) - 1\right]} \tag{B.10}$$

Para el caso de suspensiones salt-free realistas, la Ec. B.10 se transforma en

$$\frac{d^2\Psi^0(r)}{dr^2} + \frac{2}{r}\frac{d\Psi^0(r)}{dr}$$
$$= -\frac{e}{\epsilon_0 \epsilon_{rs}} \frac{\sum_{i=1}^{N} z_i b_i \exp\left(-\frac{z_i e \Psi^0(r)}{k_B T}\right)}{1 + \sum_{i=1}^{N} \frac{b_i}{n^{max}}\left[\exp\left(-\frac{z_i e \Psi^0(r)}{k_B T}\right) - 1\right]} \tag{B.11}$$

donde los distintos coeficientes b_i representan las concentraciones de las distintas especies iónicas (contraiones añadidos, e iones procedentes de la disociación del agua y de la contaminación por CO_2 atmosférico) donde tomamos $\Psi^0(r) = 0$. Puede encontrarse más información sobre el cálculo de estos coeficientes en la Sección 3.1.1.

Para el cálculo de los términos fuera del equilibrio en suspensiones salt-free ideales, y debido a la simetría del problema, usamos las funciones $h(r)$, $\phi_c(r)$, $Y(r)$ [104]

$$\mathbf{v}(\mathbf{r}) = (v_r, v_\theta, v_\varphi) = \left(-\frac{2}{r}h(r)E\cos\theta, \frac{1}{r}\frac{d}{dr}(rh(r))E\sin\theta, 0\right) \tag{B.12}$$

$$\delta\mu_c(\mathbf{r}) = -z_c e \phi_c(r) E \cos\theta \tag{B.13}$$

$$\delta\Psi(\mathbf{r}) = -Y(r) E \cos\theta \tag{B.14}$$

con $E = |\mathbf{E}|$. Sustituyendo el esquema de perturbación previo en las ecuaciones electrocinéticas, Ecs. B.2 − B.6, despreciando los términos de perturbación no lineales, y teniendo en cuenta la simetría del problema, obtenemos

$$\mathcal{L}(\mathcal{L}h(r)) + \frac{i\omega\rho_s}{\eta}\mathcal{L}h(r) = -\frac{z_c e^2}{k_B T \eta r}$$
$$\times \left(\frac{\mathrm{d}\Psi^0(r)}{\mathrm{d}r}\right) n_c^0(r) \left(\phi_c(r) - \frac{n_c^0(r)}{n_c^{max}} Y(r)\right) \tag{B.15}$$

$$\mathcal{L}\phi_c(r) + \frac{i\omega\lambda_c}{k_B T}\left(\phi_c(r) - Y(r)\right) = \frac{e}{k_B T}\left(\frac{\mathrm{d}\Psi^0(r)}{\mathrm{d}r}\right)$$
$$\times \left(1 - \frac{n_c^0(r)}{n_c^{max}}\right)\left(z_c \frac{\mathrm{d}\phi_c(r)}{\mathrm{d}r} - \frac{2\lambda_c}{e}\frac{h(r)}{r}\right) \tag{B.16}$$

$$\mathcal{L}Y(r) = -\frac{z_c^2 e^2 n_c^0(r)}{\epsilon_0 \epsilon_{rs} k_B T}\left(\phi_c(r) - Y(r)\right) \tag{B.17}$$

donde el operador $\mathcal{L}$ se define como

$$\mathcal{L} \equiv \frac{\mathrm{d}^2}{\mathrm{d}r^2} + \frac{2}{r}\frac{\mathrm{d}}{\mathrm{d}r} - \frac{2}{r^2} \tag{B.18}$$

Debido al tamaño finito de los contraiones, éstos no pueden aproximarse a la superficie de la partícula a una distancia inferior a un radio iónico. Tomando dicho radio como su radio de hidratación, R, obtenemos que la región entre la superficie de la partícula, $r = a$, y la superficie esférica $r = a + R$ es libre de carga. Con esta consideración, resolvemos las ecuaciones electrocinéticas, Ecs. B.10, B.15 − B.17, únicamente entre $r = a + R$ y $r = b$. Para la región entre $r = a$ y $r = a+R$, las ecuaciones a resolver son la ecuación de Laplace para el potencial eléctrico y las ecuaciones $\mathcal{L}(\mathcal{L}h(r)) = 0$, $\phi_c(r) = 0$, y $\mathcal{L}Y(r) = 0$ para el resto de funciones esféricas. Llamamos modelo FIS+L a este modelo electrocinético completo que incluye efectos de tamaño iónico finito y que considera una distancia mínima de aproximación de los contraiones a la superficie de la partícula.

Las condiciones de contorno necesarias para resolver las ecuaciones electrocinéticas son las siguientes. En la superficie de la partícula aplicamos la continuidad del potencial eléctrico, la discontinuidad de la componente

normal del vector desplazamiento, la condición de no deslizamiento para el fluido y la impenetrabilidad de los iones a través de la superficie de la partícula. En la superficie externa de la celda usamos condiciones de contorno de Kuwabara para la velocidad del fluido y de Shilov-Zharkikh-Borkovskaya para el potencial eléctrico perturbado. La consideración de una distancia mínima de aproximación de los contraiones a la superficie de la partícula implica que haya que aplicar la continuidad de la presión y de las componentes normales y tangenciales de la velocidad del fluido y de la vorticidad en la superficie esférica $r = a + R$. Por último, también es necesario el cálculo de la fuerza neta que actúa sobre la partícula o sobre la celda [68,104]. Puede encontrarse más información sobre las condiciones de contorno en la Sección 2.1.2.

Método y cantidades calculadas

Método

En este trabajo discutimos los resultados del modelo electrocinético FIS+L. Para mostrar el efecto del tamaño iónico finito en suspensiones salt-free, comparamos los resultados del modelo con predicciones estándar para iones puntuales, modelo PL [67–70]. Las ecuaciones electrocinéticas junto con sus condiciones de contorno forman un problema de valores de frontera que puede resolverse numéricamente usando la rutina de MATLAB bvp4c [107].

Consideramos también distintas suspensiones concentradas salt-free realistas: suspensiones con contraiones añadidos coincidentes, WDC (léase como Water Dissociation Coincident), o no, WDNC (Water Dissociation Non-Coincident), con los iones producidos por la disociación del agua, *i.e.*, H^+ o OH^-; y suspensiones con contraiones añadidos coincidentes, WDACC (léase como Water Dissociation Atmospheric Contamination Coincident), o no, WDACNC (Water Dissociation Atmospheric Contamination Non-Coincident), con los iones producidos por la disociación del agua o por la contaminación con CO_2 atmosférico, *i.e.*, H^+, OH^-, HCO_3^-. Comparamos también estos resultados con los del modelo FIS+L para suspensiones salt-free ideales con sólo contraiones añadidos (SF).

Por motivos de simplicidad, asumimos que el volumen promedio ocupado por un contraión es $V = (2R)^3$, donde $2R$ es el diámetro efectivo del contraión. Con esta consideración, la máxima concentración posible de contraiones debido al efecto de volumen excluido es $n_c^{max} = (2R)^{-3}$. Esto se corresponde con un empaquetamiento cúbico simple (52% de empaquetamiento). En concentraciones molares, los valores usados en los cálculos,

$n_c^{max} = 22$, 4 y 1.7 M, equivalen aproximadamente a diámetros efectivos de contraión $2R = 0.425$, 0.75 y 1 nm, respectivamente. Estos valores son diámetros iónicos hidratados típicos [108]. En la Tabla 2.1 (véase página 26) se muestran los parámetros usados en los cálculos realizados. Los parámetros escogidos se corresponden con contraiones H^+ hidratados, que se encuentran comúnmente en muchas condiciones experimentales con suspensiones salt-free de, por ejemplo, partículas sulfonatadas cargadas negativamente, debido al proceso de limpieza de la suspensión con resinas intercambiadoras de protones.

Cantidades calculadas

La movilidad electroforética dinámica μ de una partícula esférica en una suspensión coloidal concentrada puede definirse a partir de la relación entre la velocidad electroforética de la partícula y el campo eléctrico macroscópico. De acuerdo con las Refs. [14,68] puede calcularse como

$$\mu = \frac{2h(b)}{b} \tag{B.19}$$

Obtenemos la movilidad dinámica adimensional a partir de

$$\mu^* = \frac{3\eta e}{2\epsilon_0 \epsilon_{rs} k_B T}\mu \tag{B.20}$$

La conductividad compleja, K, de la suspensión se define usualmente en términos de los promedios de la densidad de corriente eléctrica local y del campo eléctrico en el volumen de una celda representativa de la suspensión completa. Siguiendo un procedimiento similar al descrito en las Refs. [14,69] obtenemos

$$K = \left(\frac{z_c^2 e^2}{\lambda_c} \frac{d\phi_c(r)}{dr}\bigg|_{r=b} - \frac{2h(b)}{b} z_c e \right) n_c^0(b) - i\omega\epsilon_{rs}\epsilon_0 \frac{dY(r)}{dr}\bigg|_{r=b} \tag{B.21}$$

Basta con tomar $\omega = 0$ en la ecuación anterior para obtener una expresión para el cálculo de la conductividad dc de la suspensión. A partir de la conductividad compleja, las partes real $\epsilon_r'(\omega)$ e imaginaria $\epsilon_r''(\omega)$ de la permitividad relativa compleja de la suspensión $\epsilon_r(\omega)$ se calculan como

$$K(\omega) = K(\omega = 0) - i\omega\epsilon_0\epsilon_r(\omega) = K(\omega = 0) + \omega\epsilon_0\epsilon_r''(\omega) - i\omega\epsilon_0\epsilon_r'(\omega) \tag{B.22}$$

$$\epsilon_r'(\omega) = -\frac{\text{Im}[K(\omega)]}{\omega\epsilon_0} \tag{B.23}$$

$$\epsilon_r''(\omega) = \frac{\text{Re}[K(\omega)] - K(\omega = 0)}{\omega\epsilon_0} \tag{B.24}$$

Resultados y discusión

Mediante el uso de una aproximación de celda esférica, analizamos el efecto del tamaño iónico finito en la respuesta de una suspensión concentrada salt-free de partículas esféricas a campos eléctricos estáticos y oscilantes.

Suspensiones salt-free: doble capa eléctrica de equilibrio

La Fig. 2.1 (véase página 29) muestra el potencial eléctrico adimensional (a) y la concentración de contraiones (b) a lo largo de la celda. Podemos ver en la Fig. 2.1a que la inclusión del tamaño iónico finito siempre aumenta el valor del potencial eléctrico en la superficie en comparación con la predicción para iones puntuales, valor que se recupera en el límite de contraiones puntuales ($n_c^{max} = \infty$). Esto se debe que al limitar la concentración de contraiones en la vecindad de la partícula, disminuimos de forma significativa el apantallamiento a la carga de la partícula, lo que aumenta el potencial en la superficie. También podemos ver en la Fig. 2.1b cómo la inclusión de efectos de tamaño iónico crea regiones de saturación que se corresponden con "plateaus" en la concentración de contraiones. Estas regiones de saturación, y por tanto también el potencial en la superficie, son mayores cuanto mayor es el tamaño del ión, o análogamente cuanto menor es n_c^{max}.

En la Fig. 2.3 (véase página 31) se representa el potencial eléctrico adimensional en la superficie de la partícula para distintos valores de carga de partícula (a) y de fracción de volumen de partícula (b). Encontramos que el potencial eléctrico en la superficie crece con la densidad de carga de partícula, Fig. 2.3a. Sin embargo, en algunos casos apreciamos un comportamiento diferente al que se encuentra con iones puntuales: inicialmente, el potencial en la superficie crece de forma rápida con la densidad de carga; esta tendencia es seguida por un crecimiento mucho más lento para valores más altos de carga de partícula en el caso PL o cuando el tamaño de los contraiones es pequeño. Este fenómeno está relacionado con el efecto clásico de condensación de contraiones: para altas cargas de partícula se forma una capa de contraiones junto a la superficie de la partícula [64, 109]. Cuando tenemos en cuenta el tamaño iónico finito limitamos la aparición del efecto clásico de condensación. Esto se debe a que cuando aumentamos la carga de la partícula los contraiones adicionales se unen al condensado y lo agrandan. Este hecho explica el aumento del potencial eléctrico en la superficie que apreciamos para altos valores de tamaño de ión y densidad superficial de carga de partícula.

Como hemos visto, la inclusión de efectos de tamaño iónico finito modifica de forma significativa la región de condensación iónica próxima a la superficie de la partícula para cargas moderadas y altas.

Suspensiones salt-free: electrocinética dc

El comportamiento clásico de la movilidad electroforética de partículas esféricas en una suspensión concentrada salt-free considerando iones puntuales, modelo PL, es el siguiente: para cargas superficiales de partícula bajas, se aprecia un gran aumento de la movilidad electroforética con la carga superficial. Cuando la fracción de volumen de partícula disminuye, este aumento es aún mayor. Este comportamiento sigue una ley de tipo Hückel que conecta linealmente ambas magnitudes. Cuando aumentamos la carga de la partícula, la movilidad electroforética alcanza un "plateau" y se vuelve prácticamente independiente de la carga de partícula. Este hecho está asociado con la generación de una capa de condensación de contraiones junto a la superficie de la partícula [64, 109]. Entre estos regímenes observamos un máximo seguido de una pequeña disminución de la movilidad electroforética que varía con la fracción de volumen. Además, encontramos que la movilidad electroforética toma valores más elevados cuanto menor es la fracción de volumen para cada valor de carga de partícula. Estos comportamientos clásicos se muestran en las Figs. 2.5, 2.6, 2.7 y 2.8 (véanse páginas 34 y 36).

Si tenemos en cuenta el tamaño iónico finito, modelo FIS+L, encontramos diferencias con respecto al caso puntual. Como podemos ver en la Fig. 2.5, la pequeña disminución que sigue al máximo en la movilidad electroforética tiende a desaparecer cuando el tamaño de los iones es considerable, así como el propio máximo. En este caso encontramos dos regímenes distintos para la movilidad electroforética cuando cambiamos la carga superficial de las partículas: un incremento inicial de la movilidad con la densidad de carga superficial, similar al visto en el caso de iones puntuales, ahora seguido, para cargas de partícula altas, por otra región con una tasa de crecimiento algo menor en la movilidad electroforética.

Cuando estudiamos el comportamiento de la movilidad electroforética al cambiar la fracción de volumen de partícula, observamos que los resultados del modelo FIS+L difieren de los predichos con el modelo PL, obteniéndose ahora valores más altos en la movilidad conforme nos aproximamos al régimen concentrado, Fig. 2.6. Además, si el tamaño iónico es suficientemente grande, encontramos un amplio mínimo a fracciones de volumen altas, que no se observa en el caso de iones puntuales.

La conductividad eléctrica de una suspensión concentrada salt-free con iones puntuales se comporta clásicamente como sigue: la conductividad aumenta con la densidad de carga superficial para cualquier valor de fracción de volumen [67]. Para cargas de partículas elevadas, la conductividad tiende a alcanzar un "plateau" debido al efecto clásico de condensación de contraiones [64]: a partir de un valor crítico de densidad de carga superficial de partícula no hay influencia apreciable en la conductividad. Una vez que se ha alcanzado dicho valor, el incremento del número de contraiones mediante el aumento de la carga superficial únicamente agranda la región de condensación y prácticamente no modifica los valores de carga y potencial fuera de dicha región. También se produce un incremento de la conductividad con la fracción de volumen, ya que el mayor número de iones móviles en la doble capa aumenta la conducitividad en mayor grado de lo que la penaliza el volumen extra no conductor ocupado por las partículas. Estos comportamientos clásicos se muestran en las Figs. 2.12, 2.13 and 2.14 (véanse páginas 44, 45 y 46).

Cuando tenemos en cuenta el tamaño finito de los contraiones (modelo FIS+L, Figs. 2.12, 2.13 and 2.14) observamos comportamientos similares, aunque los valores numéricos que toma la conductividad eléctrica son siempre mayores cuando aumentamos el tamaño iónico para cargas de partícula moderadas y altas en suspensiones concentradas. Para cargas de partícula y fracciones de volumen bajas, los resultados de ambos modelos son casi coincidentes.

La modificación de la región de condensación iónica en las proximidades de la superficie de la partícula debido al tamaño iónico finito produce un cambio en el flujo convectivo del fluido y en los flujos de los contraiones, Figs. 2.9 y 2.10 (véanse páginas 37 y 38), además de una importante disminución de la fuerza de retardo electroforético que actúa sobre la partícula cuando aplicamos un campo eléctrico estático, Tabla 2.2 (véase página 39). En el caso común de contraiones H^+, esto produce un incremento en la movilidad electroforética de las partículas y en la conductividad de la suspensión en comparación con el caso puntual. Dicho incremento crece con el tamaño del ión y con la carga de la partícula.

Suspensiones salt-free: electrocinética ac

La respuesta en frecuencia clásica de una suspensión concentrada salt-free con contraiones puntuales, modelo PL, es la siguiente: (i) a baja frecuencia, los procesos de difusión y electromigración tienen suficiente tiempo para desarrollarse por completo alrededor de la partícula. Normalmente, este he-

cho lleva a que se genere un momento dipolar eléctrico inducido que tiende a frenar el movimiento de la partícula. En esta región de frecuencias, la movilidad dinámica alcanza un "plateau" cuyo valor coincide con el de la movilidad electroforética para campos eléctricos estáticos. (ii) Conforme la frecuencia aumenta, encontramos una región de frecuencias donde los contraiones no pueden seguir las comparativamente rápidas oscilaciones del campo eléctrico. Así, el mencionado momento dipolar disminuye y, consecuentemente, la movilidad dinámica aumenta. Este proceso se conoce como relajación de Maxwell-Wagner-O'Konski (MWO) y tiene lugar siempre que el medio y la partícula cargada, rodeada por su doble capa eléctrica, presentan distintas conductividades y permitividades. (iii) Finalmente, la frecuencia puede ser tan alta que la inercia de la partícula y del fluido restrinjan el movimiento de forma progresiva. Cuando esto ocurre, la movilidad disminuye de forma continua conforme la frecuencia aumenta. Este fenómeno se conoce como relajación inercial.

Existe otro mecanismo clásico de relajación, la relajación alfa [7], que está relacionado con el efecto de polarización por concentración, esto es, la presencia de un gradiente de electrolito neutro alrededor de la partícula. Como se explica en la Ref. [73], no encontramos ninguna relajación alfa en suspensiones salt-free ya que únicamente tenemos una especie iónica, los contraiones añadidos.

La Fig. 2.16 muestra el módulo de la movilidad dinámica escalada y la Fig. 2.17 las partes real (a) e imaginaria (b) de la permitividad relativa de una suspensión concentrada salt-free en función de la frecuencia para $\phi = 10^{-2}$ (véanse páginas 51 y 52). No encontramos ninguna diferencia entre los resultados de los modelos PL y FIS+L para los "plateaus" de baja frecuencia en la movilidad y permitividad, Figs. 2.16 y 2.17a, para cualquier carga de partícula a fracción de volumen baja. Como se discutió en la Ref. [14] para la movilidad estática y la conductividad, esto se debe a que en el caso de una suspensión diluida la consideración de efectos de tamaño iónico finito sólo modifica de forma significativa los flujos contraiónicos en la inmediata vecindad de la partícula.

La relajación de MWO se asocia típicamente con el máximo que se encuentra en la parte imaginaria de la permitividad. Destacamos que para el caso de una suspensión con baja fracción de volumen, dependiendo del valor de la carga de la partícula, pueden producirse una o dos relajaciones de MWO diferenciadas, Fig. 2.17, o análogamente uno o dos máximos en la movilidad dinámica, Fig. 2.16. Asociamos el primero de ellos, conforme aumentamos la frecuencia, con la relajación MWO de la parte difusa de la

doble capa eléctrica y el segundo con la relajación del condensado.

A baja densidad de carga no se produce ningún condensado de contraiones en la proximidad de la superficie de la partícula y por tanto no se observa ningún proceso de relajación MWO del condensado. Cuando aumentamos la carga de la partícula, casi todos los contraiones que aparecen se acumulan en el condensado [64, 109], que crece de forma significativa cuando se tienen en cuenta efectos de tamaño iónico finito [53]. Esto explica por qué el tamaño iónico no produce ningún efecto considerable en la relajación MWO de la parte difusa de la doble capa eléctrica y por qué aumenta considerablemente la relajación MWO del condensado. Apreciamos también en las Figs. 2.16 y 2.17 que la frecuencia de relajación MWO de la parte difusa no cambia prácticamente con el tamaño iónico, mientras que la frecuencia de la relajación MWO del condensado aumenta con el tamaño de los contraiones, ya que también lo hace el condensado.

En las Figs. 2.18 y 2.19 (véanse páginas 54 y 55) mostramos la respuesta en frecuencia del módulo de la movilidad dinámica escalada y la parte imaginaria de la permitividad relativa de la suspensión para $\sigma = -40\,\mu\mathrm{C/cm}^2$. En las Figs. 2.16 y 2.17 hemos visto cómo se producen dos relajaciones MWO cuando aumenta la densidad de carga en condiciones de baja fracción de volumen. Ahora observamos que las relajaciones MWO del condensado y de la capa difusa en la Fig. 2.19, o de forma análoga los dos máximos en movilidad en la Fig. 2.18, tienen a solaparse en frecuencia para suspensiones concentradas con valores altos de densidad superficial de carga de partícula.

Cuando incluimos el tamaño finito de los iones encontramos cambios únicamente en la relajación MWO del condensado (incremento del máximo en movilidad y pequeña disminución de la frecuencia de relajación). Estos cambios pueden explicarse con el mismo razonamiento usado para las Figs. 2.16 y 2.17: la consideración de contraiones con tamaño finito aumenta significativamente el tamaño del condensado situado cerca de la superficie de la partícula, pero no produce ningún efecto considerable en la capa difusa. También podemos apreciar la conocida disminución en la movilidad con el aumento de la fracción de volumen en la Fig. 2.18, debida básicamente a un mayor apantallamiento de la carga de la partícula [53]: cuando aumenta la concentración de partículas, disminuye el espacio disponible para los contraiones dentro de la celda y, por tanto, se aumenta enormemente el apantallamiento de la carga de la partícula, reduciendo el valor del potencial eléctrico en la superficie y, consecuentemente, de la movilidad electroforética.

Las Figs. 2.20 y 2.21 (véanse páginas 56 y 57) presentan el módulo de

la movilidad dinámica escalada y las partes real (a) e imaginaria (b) de
la permitividad relativa de la suspensión en función de la frecuencia para
distintas cargas de partícula y fracción de volumen $\phi = 0.5$. Además, en las
Figs. 2.22 and 2.23 (véase página 58) se muestran las mismas cantidades
a $\sigma = -40$ $\mu C/cm^2$ y $\phi = 0.5$ fijas para distintos tamaños iónicos. Como
hemos mencionado anteriormente, para este valor elevado de fracción de
volumen, las dos relajaciones MWO solapan en un único pico. Podemos ver
cómo tanto la movilidad dinámica como la permitividad relativa aumentan
cuando consideramos contraiones con tamaño finito en comparación con el
caso PL y también cuando aumentamos la carga de la partícula. Esto es
debido a que un incremento de la densidad de carga superficial o la consi-
deración de iones con tamaño finito lleva a un aumento de la polarización
de carga global en la doble capa eléctrica. Dicho aumento hace que la per-
mitividad tome valores más elevados, Figs. 2.21a y 2.23a, y que aumenten
las alturas de los picos en la parte imaginaria, Figs. 2.21b y 2.23b. Una
explicación similar se aplica al considerable incremento que se aprecia en
el máximo de movilidad, asociado con las relajaciones MWO, Figs. 2.20 y
2.22: la relajación de un momento dipolar inducido más elevado da lugar a
mayores valores de movilidad.

Las Figs. 2.21b and 2.23b también muestran un desplazamiento a mayo-
res frecuencias de la relajación MWO cuando tenemos en cuenta el tamaño
iónico finito. Este desplazamiento es mayor cuanto mayor es el tamaño
de los contraiones. La relajación MWO de la capa difusa es casi indepen-
diente del tamaño iónico, y por tanto, el desplazamiento observado se debe
enteramente a un desplazamiento de la frecuencia de relajación MWO del
condensado.

Podemos concluir que la consideración de efectos de tamaño iónico finito
hace que el proceso de relajación MWO asociado con la capa de conden-
sación de contraiones se vea aumentado para cargas de partícula moderadas
y altas. Este aumento produce un incremento en la movilidad en este rango
de frecuencias. Dicho incremento en movilidad crece con el tamaño iónico
y la carga de la partícula.

Suspensiones salt-free realistas

En un intento por acercarnos a los sistemas experimentales, hemos desa-
rrollado un modelo que incluye efectos de tamaño iónico finito en la doble
capa eléctrica de equilibrio de partículas esféricas en suspensiones concen-
tradas salt-free realistas. Estas suspensiones realistas incluyen a los iones
procedentes de la disociación del agua y a los generados por contaminación

por CO_2 atmosférico, además de los contraiones añadidos liberados por las partículas a la solución.

En las Figs. 3.1 y 3.2 (véanse páginas 70 y 72) representamos el potencial eléctrico en la superficie de la partícula frente a la fracción de volumen de partícula para distintas suspensiones salt-free realistas. Los resultados numéricos muestran que la influencia de la disociación del agua en suspensiones salt-free en medio acuoso, WDC y WDNC, es importante para fracciones de volumen menores que 10^{-2}. Además, la contaminación atmosférica, si las suspensiones están en contacto con el aire, WDACC y WDACNC, es significativa en la región de $\phi < 10^{-1}$. Vemos que también es importante distinguir los casos en los que los contraiones añadidos coinciden o no con alguna de las especies iónicas que aparecen por la disociación del agua o por el ácido carbónico. Los resultados también muestran que el tamaño iónico debe ser tenido en cuenta para cargas de partícula moderadas y altas a cualquier fracción de volumen, Figs. 3.4, 3.5 y 3.6 (véanse páginas 75, 76 y 77). Este modelo de equilibrio será usado para desarrollar modelos de no equilibrio para la respuesta de suspensiones concentradas salt-free realistas a campos eléctricos incluyendo efectos de tamaño iónico finito.

Para comprobar la validez de los modelos electrocinéticos presentados en esta tesis, hemos realizado una serie de medidas experimentales preliminares de la movilidad electroforética estática y dinámica de látexes de poliestireno sulfonatados altamente cargados en suspensiones concentradas salt-free. En la Fig. 3.8 (véase página 81) mostramos medidas experimentales junto con predicciones teóricas de la movilidad dinámica en función de la frecuencia del campo aplicado para distintas fracciones de volumen. Podemos ver que existe un buen acuerdo cualitativo entre teoría y experimento, y que dicho acuerdo mejora en todos los casos cuando consideramos el tamaño iónico finito. En la Fig. 3.7 (véase página 79) se comparan teoría y experimento para la movilidad electroforética a distintas fracciones de volumen. En este caso, para fracciones de volumen bajas, es necesario considerar suspensiones salt-free realistas si queremos encontrar un acuerdo cualitativo.

Consideramos que sería necesario mejorar estos experimentos realizando un estudio sistemático con un protocolo establecido. En particular, sería interesante repetir estos experimentos con otros valores de carga y tamaño de partícula, así como con otras especies iónicas, como K^+ o Na^+, en lugar de con contraiones H^+. La realización de medidas de espectroscopía dieléctrica de las mismas suspensiones también añadiría información útil sobre la importancia del tamaño iónico finito en la respuesta electrocinética global.

Bibliography

[1] O. P. Lavrentovich, I. Lazo, and O. P. Pishnyak, *Nature*, 2010, **467**, 947–950.

[2] W. Sparreboom, A. van den Berg, and J. C. T. Eijkel, *Nature Nanotechnology*, 2009, **4**, 713–720.

[3] K. D. Dorfman, *Rev. Mod. Phys.*, 2010, **82**, 2903–2947.

[4] D. A. Giljohann, D. S. Seferos, W. L. Daniel, M. D. Massich, P. C. Patel, and C. A. Mirkin, *Angew. Chem. Int. Ed.*, 2010, **49**, 3280–3294.

[5] A. S. Dukhin, Z. R. Ulberg, V. I. Karamushka, and T. G. Gruzina, *Adv. Colloid Interface Sci.*, 2010, **159**, 60–71.

[6] J. López-Viota, S. Mandal, A. V. Delgado, J. L. Toca-Herrera, M. Möller, F. Zanuttin, M. Balestrino, and S. Krol, *J. Colloid Interface Sci.*, 2009, **332**, 215–223.

[7] S. S. Dukhin and V. N. Shilov, *Dielectric phenomena and the double layer in disperse systems and polyelectrolytes*, John Wiley & Sons, New York, 1974.

[8] J. Lyklema, *Fundamentals of interface and colloid science: vol. II, Solid-liquid interfaces*, Academic Press, London, 1995.

[9] J. H. Masliyah and S. Bhattacharjee, *Electrokinetic and colloid transport phenomena*, Wiley-Interscience, New Jersey, 2006.

[10] M. Z. Bazant, M. S. Kilic, B. D. Storey, and A. Ajdari, *Adv. Colloid Interface Sci.*, 2009, **152**, 48–88.

[11] M. J. Aranda-Rascón, C. Grosse, J. J. López-García, and J. Horno, *J. Colloid Interface Sci.*, 2009, **335**, 250–256.

[12] A. S. Khair and T. M. Squires, *J. Fluid Mech.*, 2009, **640**, 343356.

[13] J. J. López-García, M. J. Aranda-Rascón, C. Grosse, and J. Horno, *J. Colloid Interface Sci.*, 2011, **336**, 325–330.

[14] R. Roa, F. Carrique, and E. Ruiz-Reina, *Phys. Chem. Chem. Phys.*, 2011, **13**, 19437–19448.

[15] J. Ibarra-Armenta, A. Martín-Molina, and M. Quesada-Pérez, *Phys. Chem. Chem. Phys.*, 2009, **11**, 309–316.

[16] P. Chodanowski and S. Stoll, *J. Chem. Phys.*, 2001, **115**, 4951–4960.

[17] F. Jiménez-Ángeles and M. Lozada-Cassou, *J. Phys. Chem. B*, 2004, **108**, 7286–7296.

[18] A. Diehl and Y. Levin, *J. Chem. Phys.*, 2008, **129**, 124506.

[19] A. Martín-Molina, J. G. Ibarra-Armenta, E. González-Tovar, R. Hidalgo-Álvarez, and M. Quesada-Pérez, *Soft Matter*, 2011, **7**, 1441–1449.

[20] J. G. Ibarra-Armenta, A. Martín-Molina, and M. Quesada-Pérez, *Phys. Chem. Chem. Phys.*, 2011, **13**, 13349–13357.

[21] E. González-Tovar and M. Lozada-Cassou, *J. Phys. Chem.*, 1989, **93**, 3761–3768.

[22] G. Giupponi and I. Pagonabarraga, *Phil. Trans. R. Soc. A*, 2011, **369**, 2546–2554.

[23] V. Lobaskin, B. Dünweg, M. Medebach, T. Palberg, and C. Holm, *Phys. Rev. Lett.*, 1997, **98**, 176105.

[24] I. Pagonabarraga, B. Rotenberg, and D. Frenkel, *Phys. Chem. Chem. Phys.*, 2010, **12**, 9566–9580.

[25] J. Zhou and F. Schmid, *J. Phys.: Condens. Matter*, 2012, **24**, 464112.

[26] M. Z. Bazant, B. Storey, and A. Kornyshev, *Phys. Rev. Lett.*, 2011, **106**, 046102.

[27] M. Lozada-Cassou, E. González-Tovar, and W. Olivares, *Phys. Rev. E*, 1999, **60**, R17–20.

[28] A. Chatterji and J. Horbach, *J. Chem. Phys.*, 2007, **126**, 064907.

[29] A. Martín-Molina, C. Rodríguez-Beas, R. Hidalgo-Álvarez, and M. Quesada-Pérez, *J. Phys. Chem. B*, 2009, **113**, 6834–6839.

[30] G. Giupponi and I. Pagonabarraga, *Phys. Rev. Lett.*, 2011, **106**, 248304.

[31] J. Lyklema, *Adv. Colloid Interface Sci.*, 2009, **147**, 205–213.

[32] M. L. Jiménez, A. V. Delgado, and J. Lyklema, *Langmuir*, 2012, **28**, 6786–6793.

[33] J. J. Bikerman, *Philos. Mag.*, 1942, **33**, 384–397.

[34] C. W. Outhwaite and L. B. Bhuiyan, *J. Chem. Soc., Faraday Trans. 2*, 1983, **79**, 707–718.

[35] L. B. Bhuiyan and C. W. Outhwaite, *Phys. Chem. Chem. Phys.*, 2004, **6**, 3467–3473.

[36] L. B. Bhuiyan and C. W. Outhwaite, *J. Colloid Interface Sci.*, 2009, **331**, 543–547.

[37] L. Lue, N. Zoeller, and D. Blankschtein, *Langmuir*, 1999, **15**, 3726–3730.

[38] I. Borukhov, D. Andelman, and H. Orland, *Phys. Rev. Lett.*, 1997, **79**, 435–438.

[39] I. Borukhov, D. Andelman, and H. Orland, *Electrochim. Acta*, 2000, **46**, 221–229.

[40] I. Borukhov, *J. Polym. Sci. B Polym. Phys.*, 2004, **42**, 3598–3615.

[41] M. Eigen and W. E., *J. Phys. Chem.*, 1954, **58**, 702–714.

[42] V. Kralj-Iglic and A. Iglic, *J. Phys. II*, 1996, **6**, 477–491.

[43] K. Bohinc, V. Kralj-Iglic, and A. Iglic, *Electrochim. Acta*, 2001, **46**, 3033–3040.

[44] Z. Adamczyk and P. Warszynsky, *Adv. Colloid Interface Sci.*, 1996, **63**, 41–149.

[45] M. S. Kilic, M. Z. Bazant, and A. Adjari, *Phys. Rev. E*, 2007, **75**, 021502.

[46] M. S. Kilic, M. Z. Bazant, and A. Adjari, *Phys. Rev. E*, 2007, **75**, 021503.

[47] J. J. López-García, M. J. Aranda-Rascón, and J. Horno, *J. Colloid Interface Sci.*, 2007, **316**, 196–201.

[48] J. J. López-García, M. J. Aranda-Rascón, and J. Horno, *J. Colloid Interface Sci.*, 2008, **323**, 146–152.

[49] M. J. Aranda-Rascón, C. Grosse, J. López-García, and J. Horno, *J. Colloid Interface Sci.*, 2009, **336**, 857–864.

[50] J. J. López-García, M. J. Aranda-Rascón, C. Grosse, and J. Horno, *J. Phys. Chem. B*, 2010, **114**, 7548–7556.

[51] J. J. López-García, C. Grosse, and J. Horno, *Langmuir*, 2011, **27**, 13970–13974.

[52] J. J. López-García, J. Horno, and C. Grosse, *J. Colloid Interface Sci.*, 2012, **380**, 213–221.

[53] R. Roa, F. Carrique, and E. Ruiz-Reina, *Phys. Chem. Chem. Phys.*, 2011, **13**, 3960–3968.

[54] R. Roa, F. Carrique, and E. Ruiz-Reina, *J. Colloid Interface Sci.*, 2012, **387**, 153–161.

[55] R. Roa, F. Carrique, and E. Ruiz-Reina, *Phys. Chem. Chem. Phys.*, 2011, **13**, 9644–9654.

[56] ed. R. B. McKay, *Technological Applications of Dispersions*, Marcel Dekker Inc., New York, 1994.

[57] R. W. O'Brien, *J. Fluid Mech.*, 1990, **212**, 81–93.

[58] A. S. Dukhin and P. J. Goetz, *Characterization of Liquids, Nano- and Microparticulates, and Porous Bodies using Ultrasound*, Elsevier, Oxford, 2010.

[59] N. Dziomkina, M. Hempenius, and G. Vancso, *Advanced Materials*, 2005, **17**, 237–240.

[60] M. Medebach and T. Palberg, *J. Chem. Phys.*, 2003, **119**, 3360–3370.

[61] T. Palberg, M. Medebach, N. Garbow, M. Evers, A. B. Fontecha, H. Reiber, and E. Bartsch, *J. Phys.: Condens. Matter*, 2004, **16**, S4039–S4050.

[62] A. Reinmüller, H. Schöpe, and T. Palberg, *Soft Matter*, 2010, **6**, 5312–5315.

[63] T. Palberg, T. Köller, B. Sieber, H. Schweinfurth, H. Reiber, and G. Nägele, *J. Phys.: Condens. Matter*, 2012, **24**, 464109.

[64] H. Ohshima, *J. Colloid Interface Sci.*, 2002, **248**, 499–503.

[65] H. Ohshima, *J. Colloid Interface Sci.*, 2003, **265**, 422–427.

[66] C. P. Chiang, E. Lee, Y. Y. He, and J. P. Hsu, *J. Phys. Chem. B*, 2006, **110**, 1490–1498.

[67] F. Carrique, E. Ruiz-Reina, F. J. Arroyo, and A. V. Delgado, *J. Phys. Chem. B*, 2006, **110**, 18313–18323.

[68] F. Carrique, E. Ruiz-Reina, F. J. Arroyo, M. L. Jiménez, and A. V. Delgado, *Langmuir*, 2008, **24**, 2395–2406.

[69] F. Carrique, E. Ruiz-Reina, F. J. Arroyo, M. L. Jiménez, and A. V. Delgado, *Langmuir*, 2008, **24**, 11544–11555.

[70] E. Ruiz-Reina and F. Carrique, *J. Phys. Chem. B*, 2008, **112**, 11960–11967.

[71] F. Carrique and E. Ruiz-Reina, *J. Phys. Chem. B*, 2009, **113**, 8613–8625.

[72] F. Carrique and E. Ruiz-Reina, *J. Phys. Chem. B*, 2009, **113**, 10261–10270.

[73] F. Carrique, E. Ruiz-Reina, F. J. Arroyo, and A. V. Delgado, *J. Phys. Chem. B*, 2010, **114**, 6134–6143.

[74] F. J. Arroyo, F. Carrique, E. Ruiz-Reina, and A. V. Delgado, *Colloids Surf., A*, 2011, **376**, 14–20.

[75] S. Bastea, *Soft Matter*, 2010, **6**, 4223–4228.

[76] Y. Y. He, E. Wu, and E. Lee, *Chem. Eng. Sci.*, 2010, **65**, 5507–5516.

[77] R. Piazza, *Soft Matter. The stuff that dreams are made of*, Springer, New York, 2011.

[78] P. G. de Gennes, *Soft Matter*, Nobel Lecture, December 9, 1991.

[79] A. V. Delgado and V. N. Shilov, *'Electrokinetics of Suspended Solid Colloid Particles', Encyclopedia of Surface and Colloid Science*, 2006, **1:1**, 2233–2261.

[80] S. Wall, *Curr. Opin. Colloid Interface Sci.*, 2010, **15**, 119–124.

[81] M. Gouy, *J. Phys.*, 1910, **9**, 457–468.

[82] D. L. Chapman, *Philos. Mag.*, 1913, **25**, 475–481.

[83] O. Stern, *Z. Elektrochem.*, 1924, **30**, 508–516.

[84] K. Asami, *Prog. Polym. Sci.*, 2002, **27**, 1617–1659.

[85] A. Di Biasio and C. Cametti, *Bioelectrochemistry*, 2007, **71**, 149–156.

[86] S. Tomić, T. Vuletić, S. D. Babić, S. Krča, D. Ivanković, L. Griparić, and R. Podgornik, *Phys. Rev. Lett.*, 2006, **97**, 098303.

[87] M. Z. Bazant and T. M. Squires, *Phys. Rev. Lett.*, 2004, **92**, 066101.

[88] Y. C. Wang, A. L. Stevens, and J. Han, *Anal. Chem.*, 2005, **77**, 4293–4299.

[89] R. J. Hunter, *Colloids Surf., A*, 1998, **141**, 37 – 66.

[90] C. Grosse and A. V. Delgado, *Curr. Opin. Colloid Interface Sci.*, 2010, **15**, 145–159.

[91] G. S. Manning, *J. Chem. Phys.*, 1969, **51**, 924933.

[92] N. Imai and F. Oosawa, *Busseiron Kenkyu*, 1952, **52**, 42–63.

[93] F. Oosawa, *Polyelectrolytes*, Marcel Dekker Inc., New York, 1971.

[94] S. Levine and G. H. Neale, *J. Colloid Interface Sci.*, 1974, **47**, 520–529.

[95] V. N. Shilov, N. I. Zharkikh, and Y. B. Borkovskaya, *Colloid J. USSR*, 1981, **43**, 434–438.

[96] F. Carrique, F. J. Arroyo, M. L. Jiménez, and A. V. Delgado, *J. Chem. Phys.*, 2003, **118**, 1945–1956.

[97] A. V. Delgado, S. Ahualli, F. J. Arroyo, and F. Carrique, *Colloids Surf. A*, 2005, **267**, 95–102.

[98] J. Cuquejo, M. L. Jiménez, A. V. Delgado, F. J. Arroyo, and F. Carrique, *J. Phys. Chem. B*, 2006, **110**, 6179–6189.

[99] H. Reiber, T. Köller, E. Ruiz-Reina, T. Palberg, R. Piazza, and F. Carrique, *J. Colloid Interface Sci.*, 2007, **309**, 315–322.

[100] A. R. Denton, *J. Phys.: Condens. Matter*, 2010, **22**, 364108.

[101] E. K. Zholkovskij, J. H. Masliyah, V. N. Shilov, and S. Bhattacharjee, *Adv. Colloid Interface Sci.*, 2007, **134-135**, 279–321.

[102] P. M. Biesheuvel and M. van Soestbergen, *J. Colloid Interface Sci.*, 2007, **316**, 490–499.

[103] C. S. Mansgeldorf and L. White, *J. Chem. Soc., Faraday Trans.*, 1992, **88**, 3598–3615.

[104] H. Ohshima, *J. Colloid Interface Sci.*, 1997, **195**, 137–148.

[105] S. Kuwabara, *J. Phys. Soc. Jpn.*, 1959, **14**, 527–532.

[106] S. Ahualli, M. L. Jiménez, F. Carrique, and A. V. Delgado, *Langmuir*, 2009, **25**, 1986–1997.

[107] J. Kierzenka and L. F. Shampine, *ACM Trans. Math. Softw.*, 2001, **27**, 299–316.

[108] J. N. Israelachvili, *Intermolecular and surface forces*, Academic Press, London, 1992.

[109] H. Ohshima, *Theory of colloid and interfacial electric phenomena*, Academic Press, The Netherlands, 2006.

[110] B. H. Bradshaw-Hajek, S. J. Miklavcic, and L. R. White, *Langmuir*, 2010, **26**, 7875–7884.

[111] J. W. Krozel and D. A. Saville, *J. Colloid Interface Sci.*, 1992, **150**, 365–373.

[112] E. Lee, T. S. Tong, M. H. Chih, and J. P. Hsu, *J. Colloid Interface Sci.*, 2002, **251**, 109–119.

[113] Malvern Instruments, `http://www.malvern.com`.

[114] Ikerlat Polymers, `http://www.ikerlatpolymers.es`.

[115] R. A. Rica, *Electrokinetics of concentrated suspensions of spheroidal nanoparticles*, PhD Thesis, Universidad de Granada, 2011.

[116] Colloidal Dynamics, `http://www.colloidal-dynamics.com`.

Acknowledgements

First, I wish to express my gratitude to my supervisors Félix Carrique and Emilio Ruiz-Reina. I'm specially grateful to Félix for his full dedication, his patience and for giving me support and freedom during my PhD. My achievements during this period are largely owed to him.

Next, I would like to thank my good friend Juan J. Alonso for the tremendous variety of things that I have been able to learn from him.

I also appreciate the stimulating discussions with Antonio Varias, Javier Ruiz and Carlos Criado. I thank my colleagues from Física Aplicada for the time spent during the last 3^{1}/$_{2}$ years.

Special thanks go to my great ukrainian mentors Vladimir Shilov and Emiliy Zholkovskiy. I will always consider Kiev as my second home. I thank Ángel Delgado, Silvia Ahualli, Yulia Borkovskaya, Victorio Estrela-Llopis, Vladimir Lobaskin and Maksym Romensky for their help and advice during my stays in Granada, Kiev and Dublin.

Last but not least, I want to express my gratitude to my family and friends. I specially thank my parents Ramón and Gádor, my brother Ricardo and my friends Bruno 🍺, Mark, Álvaro and Guille.